Simulation and Correction of Cross Talk in the HARP Time Projection Chamber

Lara Howlett
University of Sheffield

A thesis submitted for the degree of
Doctor of Philosophy in the subject of Physics
March 2004

To Del

It is good to have an end to journey toward;
but it is the journey that matters, in the end.
Ursula K. Le Guin

Acknowledgements

First I would like to thank by supervisor Chris Booth both for his guidance throughout the PhD and his tireless proof reading while I was writing my thesis. Thanks also to all those who have helped me throughout my PhD, be it by helping me with computer problems, useful physics discussions or just making things more fun than they would otherwise have been (or in the case of *writing* the thesis less painful). Thanks go to all members of the HARP collaboration, particularly to HARP colleagues: Stefan Piperov, Malcolm Ellis, Simon Robbins, Alex Grossheim, Petr Gorbunov, Gabriel Vidal Sitjes, Gersende Prior and Silvia Borghi. Thanks are also due to all the members of the Sheffield HEP group past and present, particularly Ben Morgan and Paul Hodgson. A debt of gratitude also goes to my mum and dad and all my friends and family for putting up with me whilst I was completing my PhD. Most importantly thanks go to my long suffering husband for always being there to help me in whatever way I needed.

Preface

This thesis describes work undertaken as a member of the HARP collaboration. My initial contribution as a member of the collaboration was to take responsiblity for the MWPC reconstruction software described in Chapter 3. This involved providing the functionality for all algorithms and classes to create MwpcTrack objects, along with interfacing this software to the Kalman package when this became available. The main work of the thesis is based on the TPC Simulation. I collaborated to completely restructure this software as described in Chapter 4. This work involved both the movement of code to algorithms and objects, the addition of new functionality to the code and ensuring that all input parameters were those used during data taking. I then produced reference plots to demonstrate that the code performed as expected for each physics process.

After a simulation which reproduced the design specifications of the TPC was complete I implemented the cross talk effect in the simulation using the cross talk model and pulser data measurements provided to me by others. The software to do this and and the study of the effect of cross talk on reconstructed observables described in Chapter 6 is my own work. I went on to design a correction for this effect which is described in Chapter 7 and to test this correction on both data and Monte Carlo. Again both the correction software and the accompanying study described in Chapters 7 and 8 are my own work.

Abstract

This thesis is based on the HARP hadron production experiment. A simulation of the HARP TPC has been developed to reproduce the design specifications. An unwanted cross talk effect caused by capacitive couplings between the inputs and outputs of preamplifiers on the pad plane has been simulated on top of this ideal situation. This simulation has been used to understand the effect of cross talk on TPC measurements. A correction for the cross talk effect has been designed based on the use of the prediction and subtraction of cross talk signals where ever possible. This correction is applied to both Monte Carlo and data. For the Monte Carlo the correction is found to provide substantial improvement on all stages of reconstruction, resulting in large reductions in the detrimental effects of cross talk on momentum resolution. In the data, studies of $r\phi$ and z residuals are carried out. Large reductions in the widths of the distributions are found demonstrating that the correction works on the data. Good agreement with Monte Carlo is also found, demonstrating that the simulation of cross talk in the Monte Carlo is reproducing accurately the cross talk found in the data.

Contents

List of Figures

List of Tables

Chapter 1

Background

Recent experiments have given strong evidence for neutrino oscillations and hence neutrino mass. This indicates physics beyond the standard model, and has raised widespread interest in neutrino physics in the particle physics community. This thesis is based on HARP, a Hadron Production experiment in the CERN PS. This chapter will demonstrate the importance of an accurate knowledge of hadron production for neutrino physics and also show that the required data is not currently available. The chapter will give a very brief review of the history of the neutrino, followed by a description of why oscillations indicate mass. Next a review of the evidence for oscillations will be given. Conventional neutrino beams and the concept of a neutrino factory will be described along with the method of calculating atmospheric neutrino flux. A brief overview of existing hadron production data at HARP energies will then be given, followed by an overview of existing hadronic Monte Carlos.

1.1 The Neutrino

The existence of the neutrino was first postulated in 1930 in order to explain the apparent violation of energy conservation in nuclear weak decays. However, it was not until 1955 that the neutrino was first observed in a reactor experiment performed by Reines and Cowan [1]. Later experiments established that the neutrino was left handed [2], and also established the distinct nature of ν_e and ν_μ neutrinos [3]. However, most neutrino experiments used the neutrino as a probe in other areas of particle physics and it is only more recently that studies of the structure and properties of the neutrino have become a focus of widespread interest in particle physics.

The Standard Model was proposed by Glashow, Salam and Weinberg in the

1960s and describes mathematically the strong, weak and electromagnetic forces [4]. At this time there was no evidence for neutrino mass and for this reason the neutrinos were introduced into the model as massless fermions. This means that in the Standard Model neither mixing nor CP violation is possible within the lepton sector.

However, today there is strong evidence for neutrino mass and many experiments current and planned are designed to probe the physical properties of the neutrino and perhaps give a window on CP violation in the lepton sector, Grand Unified Theories (GUTs) and the reason for the three generations of quarks. Neutrinos are also of interest as they provide a window for cosmology and astrophysics - space is filled with neutrinos which are relics of the big bang and are also produced by astronomical sources which they can be used to study.

1.2 Neutrino Physics

1.2.1 Neutrino Oscillations and Masses

In this section the simple case of oscillations in a vacuum will be considered and the reason that neutrino mass indicates oscillations will be demonstrated. If neutrinos are massive then there are two bases in which they can be represented, the flavour eigenstates in which neutrinos are produced by weak processes (ν_e, ν_μ, ν_τ...) and the mass eigenstates (ν_1, ν_2, ν_3...). Each flavour eigenstate will in general be a linear combination of the mass eigenstates:

$$|\nu_\alpha\rangle = \sum_{i=1}^{n} U^*_{\alpha i}|\nu_i\rangle, \tag{1.1}$$

where n is the number of light neutrino species and $U_{\alpha i}$ is the corresponding element of the neutrino mixing Maki-Nakajawa-Sakata (MNS) matrix [5] analogous to the CKM matrix for quarks. In analogy to the quark matrix this can be parameterised as follows:

$$U = \begin{bmatrix} c_{12}c_{13} & s_{12}c_{13} & s_{13} \\ -s_{12}c_{23} - c_{12}s_{23}s_{13} & c_{12}c_{23} - s_{12}s_{23}s_{13} & s_{23}c_{13} \\ s_{12}s_{23} - c_{12}c_{23}s_{13} & -c_{12}s_{23} - s_{12}c_{23}s_{13} & c_{23}c_{13} \end{bmatrix} \tag{1.2}$$

for three generations of neutrino. $c_{ij} = \cos\theta_{ij}$ and $s_{ij} = \sin\theta_{ij}$, with θ_{ij} indicating the mixing angle between neutrinos i and j. CP conservation has been assumed (ie $\delta = 0$).

Measurements of the Z^0 peak in e^+e^- annihilations show that there are only three neutrino generations which couple to the Z^0 [6]. However there is no physical reason why there can't be other 'sterile' neutrinos which have no weak coupling. Indeed this may be the only way to accommodate all the experimental evidence as will be shown later on.

A neutrino which is created via a weak interaction will be produced initially in a weak eigenstate ν_α, which will be a superposition of mass eigenstates. The mass eigenstate will evolve over time according to Schrodinger's equation so that once it has travelled a distance L its state vector will be [7]:

$$|\nu_\alpha(L)\rangle = \sum_{i=1}^{n} U^*_{\alpha i} e^{-i(m_i^2/2E)L} |\nu_i(0)\rangle = \sum_\beta \sum_i U^*_{\alpha i} e^{-i(m_i^2/2E)L} U_{\beta i} |\nu_\beta(0)\rangle, \qquad (1.3)$$

where it has been assumed the mass of the neutrino is small with respect to it's momentum.

So the probability that after a distance L the eigenstate α has evolved to a state β can be calculated as:

$$P(\nu_\alpha \to \nu_\beta) = |\langle \nu_\beta | \nu_\alpha \rangle|^2 = \delta_{\alpha\beta} - 4 \sum_{i>j} \Re(U^*_{\alpha i} U_{\beta i} U_{\alpha j} U^*_{\beta j} \sin^2(\Delta m^2_{ij} L/4E)), \qquad (1.4)$$

where $\Delta m^2_{ij} = m^2(\nu_i) - m^2(\nu_j)$, E is the energy of the neutrino, L is the distance travelled, and U are the corresponding elements of the MNS matrix.

It can be seen from the above equation that if the neutrinos have non degenerate masses they are expected to oscillate with a frequency defined by the neutrino energy and the mass difference. Furthermore in order to be sensitive to a mass difference Δm^2_{ij} an experiment must fulfil the criterion:

$$\frac{E}{L} \sim \Delta m^2_{ij}. \qquad (1.5)$$

The above treatment is a simplification of the quantum mechanics used in a more rigorous treatment since a plane wave approximation has been made, but nevertheless it produces the same oscillatory dependence on energy, distance and mass differences. The situation is also more complex when neutrinos travel through matter [7, 8]. However, it can be seen that neutrino oscillations are expected to occur as a direct result of non zero and non degenerate neutrino masses.

1.2.2 Evidence for Neutrino Oscillations

There is now evidence for neutrino oscillations from various experiments [9], using neutrinos created by different methods. Experiments have measured atmospheric neutrinos, solar neutrinos, neutrinos produced in conventional beams by the decay of pions and muons, and neutrinos produced by nuclear reactors. The results of these experiments will be briefly summarised below.

Super Kamiokande is a 50 kton water Cherenkov detector which detects atmospheric neutrinos. These are produced when cosmic rays hit the earth's upper atmosphere producing hadrons. The pions from these hadronic showers decay to produce muons and the muons to muon and electron neutrinos. Since the cosmic ray flux is isotropic, the atmospheric neutrino flux will be isotropic. However SuperKamiokande observed a zenith angle dependent deficit in the ν_μ flux which is consistent with $\nu_\mu \to \nu_\tau$ oscillations with $1.6 \times 10^{-3} eV^2 < \Delta m^2_{atm} < 3.9 \times 10^{-3} eV^2$ and $\sin^2 \theta_{atm} > 0.92$ [10]. This result from SuperKamiokande is now also supported by the K2K long baseline experiment from KEK to Kamioka. This experiment produces a ν_μ beam using an accelerator. The beam intensity is measured with near detectors and the ν_μ flux is measured with the SuperKamiokande detector at a distance of 250 km. The number of events observed at the far detector is in good agreement with the number predicted by the SuperKamiokande fit parameters and in addition to this supporting evidence is given by the study of the energy spectra at the near and far detectors.

Further evidence for neutrino oscillations is provided by the SNO experiment [11]. SNO studies solar neutrinos coming from the decay of B^8 in the sun. SNO, a 1 kton heavy water Cherenkov detector, looks for three reactions:

$$\nu + d \to e^- + p + p, \tag{1.6}$$

$$\nu + d \to \nu + p + n, \tag{1.7}$$

$$\nu + e \to \nu + e. \tag{1.8}$$

The first reaction is a charged current reaction and is only sensitive to electron neutrinos. The second reaction is a neutral current reaction and is sensitive to all flavours of neutrino. The last is an elastic scattering reaction and is also sensitive to all flavours of neutrino. Comparison of the different reaction rates allows us to infer the number of neutrinos with an active flavour other than ν_e by the comparison of the ν_e flux from charged current interactions with the total ν flux from elastic scattering interactions. If the flux from charged current interaction is greater than that from elastic scattering then the neutrinos from the sun must be changing into other active flavours. SNO finds that indeed some of the ν_e from the sun are changing to some other flavour. The SNO result has recently been confirmed by the KamLAND experiment [12] which uses the $\overline{\nu}_e$ flux from nuclear reactors at Japanese power stations. A 1 kton ultra pure liquid scintillator detector at a distance of around 180 km is used to look for $\overline{\nu}_e$. This shows a deficit of the $\overline{\nu}_e$ flux in agreement with SNO. The best fit to the KamLAND data gives a value $\Delta m^2 = 6.9 \times 10^{-5} eV^2$.

The only experiment so far to see an appearance signal is the Liquid Scintillator Neutrino Detector (LSND) at LAMPF in New Mexico [13], which uses a ν_μ beam and looks for the appearance of ν_e using a 167 ton detector made of mineral oil doped with liquid scintillator at a distance of 30 m. An excess of ν_e over the expected background is observed. However KARMEN, a similar experiment using the ISIS spallation facility at RAL, sees no oscillation signal [14]. KARMEN also looks for ν_e appearance from a ν_μ beam using a 56 ton liquid scintillator detector 17.7 m down stream of the neutrino source. The parameter space covered by the two experiments is not quite the same and a joint analysis by the two experiments still allows oscillations with $0.2\ eV^2 < \Delta m^2_{LSND} < 1\ eV^2$. MiniBOONE which started taking data in 2002 will be able to probe the full parameter space of LSND using an 800 ton pure mineral oil detector 500 m downstream of the neutrino source [15].

1.2.3 Possible Hierarchies

The results of the three sets of experimental results - solar, atmospheric and LSND cannot be compatible with three neutrino mixing since all results have different orders of magnitude for Δm^2 and clearly:

$$\Delta m^2_{12} = \Delta m^2_{13} - \Delta m^2_{23}. \tag{1.9}$$

So if the LSND result is confirmed an additional 'sterile' neutrino will be required in order to fit all the data. However the results from the other experiments do not favour the addition of a fourth sterile neutrino, giving better fits to an approach containing just three. Figure 1.1 summarises the results so far if the LSND result is not included. The large mass splitting is provided by the atmospheric neutrino data and the small one by the solar data. However since only the mass splittings and not the masses have been measured it is still not known whether the hierarchy is as pictured or whether the two states with small separation should in fact be at the top.

1.3 Conventional Neutrino Beams

As mentioned above several neutrino experiments use an artificial neutrino beam as their source. These beams consist of several components. A high intensity proton beam impinges on a target, producing pions. These are focused using a magnetic

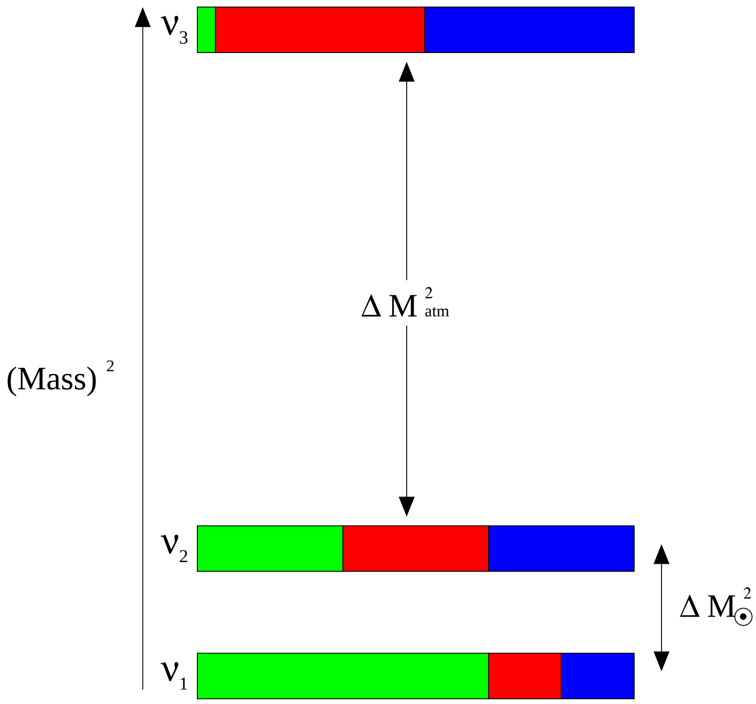

Figure 1.1: Neutrino mass spectrum indicating what is known from atmospheric and solar neutrino data. The colours indicate the approximate flavour content where green represents ν_e, red represents ν_μ and blue represents ν_τ. Since only mass differences and not absolute masses are known, the hierarchy could be inverted, with the two close together states at the top.

horn. The pions then pass into a decay region where neutrinos are produced via the reaction:

$$\pi^+ \longrightarrow \nu_\mu + \mu^+. \tag{1.10}$$

Finally there is a beam dump into which the muons and the remaining pions are absorbed. Two such beams are the BooNE neutrino beam at FermiLab [15] which uses a 12 GeV beam and a Beryllium target and the KEK beam in Japan [16] which uses an 8 GeV proton beam on an aluminium target. For both beams a large contribution to the systematic uncertainty in results of their associated experiments arises from knowing the beam composition.

1.4 Neutrino Factory

With the now overwhelming evidence for neutrino mass there is widespread interest in neutrino physics. In addition to accurately measuring the mass differences and the mixing angles in the neutrino sector, neutrinos can be used to study CP violation in the lepton sector. Furthermore since neutrino mass indicates physics beyond the standard model it is believed that the hierarchy of masses could enable us to discriminate between different GUTs and perhaps even understand the origin of quark and lepton flavours [17]. However despite the wide range of neutrino experiments currently underway it will still not be possible to fully parameterise the neutrino sector. To do this will require the higher intensities and lower systematics of a neutrino factory.

A typical schematic of such a neutrino factory is shown in Figure 1.2. In this design a proton beam of a few GeV hits a hadron production target producing pions which are then captured by a magnetic horn system and decay in flight to a muon and a muon neutrino which is lost. The muon bunches which result from these decays are short but have a large spread in momentum. A phase rotation is performed where the momentum spread is reduced and the size of the bunch increases. In order to produce a very intense neutrino beam a very focused muon beam is needed, so the muons need to be cooled in the transverse direction. This is done by a method called ionisation cooling [18]. The muons are passed through an absorber which reduces both the longitudinal and transverse components of momentum. The longitudinal component of momentum is then replaced using a radio frequency (rf) cavity. After the ionisation cooling the muons are accelerated and fed into a decay ring which typically has a figure of eight or triangular design. Here they decay into a ν_μ and an $\overline{\nu}_e$ producing two intense neutrino beams. (For a more detailed description see [19, 20]).

A neutrino factory has several advantages over conventional beams. Since all neutrinos are produced from muon decays:

$$\mu^+ \rightarrow e^+ \nu_e \overline{\nu}_\mu, \tag{1.11}$$

the neutrino factory is able to produce electron neutrinos as well as the muon neutrinos provided by conventional beams. Depending on the sign of the muon these come in pairs of $\nu_e\overline{\nu}_\mu$ (for positive muons) or $\nu_\mu\overline{\nu}_e$ (for negative muons). Since one is a particle and the other an antiparticle both flavours can be studied without ambiguity. As well as having a precisely known flavour composition due to the branching ratio of almost 100% to this decay, since the muon energy is well defined the neutrinos also have a precisely known energy composition. In addition to these lower systematics the neutrino factory is capable of much higher event rates than conventional beams - an estimated 10^{21} muon decays per year. These factors together mean that a neutrino factory would be capable of probing regions of parameter space inaccessible to conventional beams.

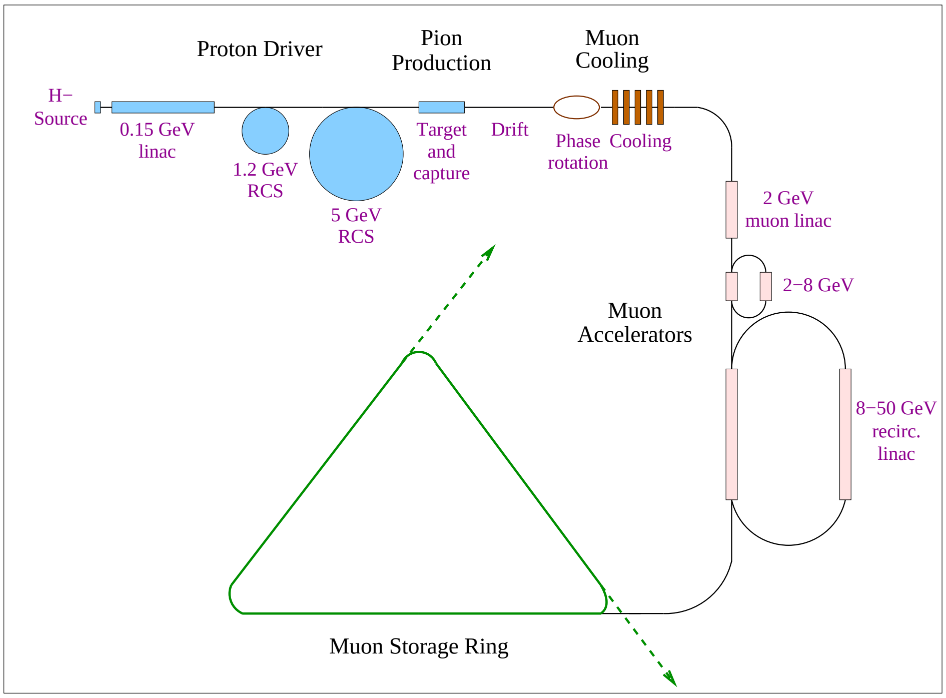

Figure 1.2: Diagram showing typical schematic of a neutrino factory. [21]

In order to produce the required number of muon decays it is necessary to have a proton beam with a power of 4 MW. This produces an extremely large power density in the target. In addition to this requirement a short bunch length is needed for the pion capture and muon capture and acceleration and a low frequency of about 100 Hz for the rf of the pion capture. These short bunches and this low frequency mean that the target is subjected to a large mechanical shock. In addition to this it is of course required that pion production from the target is as large as possible. These difficult requirements make accurate simulations of the target extremely important. Current designs for the target under consideration include rotating solid targets and liquid mercury jets [22, 23].

In order to optimise designs of the targetry and pion capture systems it is necessary to have a very accurate knowledge of hadron production. The following range of data is of particular interest:

- Proton momentum of 2-24 GeV/c to cover the energy range of proton drivers currently considered
- High Z targets since these produce the highest pion yields
- Secondary pion yields over the phase space 100 MeV/c $< p_L <$ 700 MeV/c

and $p_T < 250$ MeV/c since this is the range important for the pion capture system

- Secondary proton yield to assess induced radiation

1.5 Atmospheric Neutrinos

Atmospheric neutrinos are caused by cosmic rays hitting gas atoms in the upper atmosphere. These collisions result in hadronic showers which produce kaons and pions which decay producing neutrinos. An accurate knowledge of the atmospheric neutrino flux is of interest for several reasons. Firstly it allows us to study neutrino oscillations at energies which are inaccessible to conventional neutrino beams since atmospheric neutrinos can have energies up to 10^4 GeV. The atmospheric neutrino flux is also of interest for neutrino astronomy, since atmospheric neutrinos will be a source of background and the calibration beams for neutrino telescopes such as ANTARES and AMANDA.

Calculations of atmospheric neutrino flux require the convolution of the primary cosmic ray flux with the yield of neutrinos per incoming particle. They must also take into account the effects of the earth's geomagnetic field, so the flux of atmospheric neutrinos can be described by [24]:

$$\phi_{\nu i} = \phi_p \otimes R_p \otimes Y_{p\to\nu_i} + \sum_A \phi_A \otimes R_A \otimes Y_{A\to\nu_i}, \tag{1.12}$$

where $\phi_{p/A}$ represents the flux of protons/atoms with atomic mass A, R represents the filtering effect of the geomagnetic field, and $Y_{p/A\to\nu_i}$ represents the yield of neutrinos from a proton/atom of atomic mass A.

Calculations of atmospheric neutrino flux currently differ significantly in their results. There are two major sources of uncertainty: the energy spectrum and chemical composition of cosmic rays, and the representation of hadron production in collisions of primaries with N and O nuclei. Data on the cosmic spectrum seem to be converging and with the results of AMS [25] and BESS [26] this error seems to be under control. This leaves the major source of uncertainty in the calculation of atmospheric neutrino flux as the representation of hadron production.

In order to accurately calculate the atmospheric neutrino flux, the following range of data is required:

- Proton and pion beams with momentum between 1 and 100 GeV/c to cover the range of incident cosmic rays

- Targets of O and N nuclei
- Secondary pion, kaon and proton yields over the full phase space

1.6 Hadron Production

Hadron production at low energies is notoriously hard to describe. At low energies the value of the strong coupling constant is high meaning that at these energies perturbative QCD is no longer applicable and alternative models need to be found. In addition to this for targets heavier than hydrogen, as well as describing the hadron-nucleon interaction it is also necessary to look at the role of the nucleus in the interaction and its effect on the secondaries as they leave the nucleus.

The next sections describe the areas relevant to a discussion of current knowledge of hadron production. The focus is on hadron production at HARP energies, (momenta between 1.5 and 15 GeV/c). The first section is devoted to current experimental results. This describes existing experimental data and the general features of the distributions obtained. A brief overview of existing hadronic Monte Carlos and the problems associated with them will then be given.

1.7 Experimental Results

Despite the fact that the energies studied by the HARP experiment are extremely low by today's standards existing hadron production data is extremely sparse. A large amount of data was taken during the 60s and 70s but these data sets have severe limitations. The data in question falls into two categories: that taken with bubble chambers and that taken with spectrometers. The data taken with bubble chambers is able to provide full 4π acceptance with excellent tracking; however the data has limited statistics giving the cross sections a statistical error of around 7%. The nature of the bubble chamber means that limited target materials were available with most data being taken with hydrogen as the target. Spectrometer experiments were able to take data with excellent angular resolution and over a large range of target materials. However the angular acceptance of these experiments was small so again they cannot give a complete picture of hadron production.

Interest in hadron production at low energies has recently been revived, firstly for its use in accurate prediction of neutrino fluxes as described above, and secondly as a means to understand heavy ion collisions. The latter motivation has lead to the experiments E802[27] and E910[28] at Fermilab as well as some proton nucleus data taken using the NA49[29] detector at CERN. All these experiments used charged particle spectrometers allowing the study of a range of target nuclei over a large acceptance. The results of all these experiments will be summarised in the following section. There is also now interest in Hadron Production for the design of neutrino factories. It was for this reason that the HARP experiment was proposed in 1999[30]. Another experiment, P907, will take place at Fermilab with similar aims but studying a slighting different energy range [31].

1.7.1 Useful Definitions

Before reviewing results on hadron production some definitions which will be useful in the following discussion will be briefly outlined.

Results are often described in terms of the Feynman x variable:

$$x_F = \frac{p_L}{p_L^{max}} = \frac{2p_L}{\sqrt{s}}, \tag{1.13}$$

or rapidity:

$$y = \frac{1}{2}\ln\frac{E+p_L}{E-p_L}, \tag{1.14}$$

where p_L represents the longitudinal component of momentum and s represents the total centre of mass energy of the reaction. These quantities both describe the fraction of particle momentum in the direction of the beam particle. Particles can be separated by their Feynman x values into different regions depending on the manner of production of the particle [32]. The central or pionisation region consists of particles with $|x_F| < 0.1$. Next the fragmentation region consists of particles with $0.1 < |x_F| < 0.8 - 0.9$ and the diffractive region with $0.8 - 0.9 < |x_F| < 1$.

Particles can also be separated via their velocity using a scheme based on a definition that originates from bubble chambers, where the different classifications represent the amount of ionisation and therefore the bubble density along the track. This affected their brightness [32]. Shower particles have $\beta > 0.7$ (where $\beta = v/c$). Grey tracks have $0.3 < \beta < 0.7$ and usually correspond to protons which were knocked out of the nucleus during intra nuclear cascades. Black tracks have $\beta < 0.3$ and usually correspond to particles emitted during the de-excitation of the nucleus.

1.7.2 Hadron-Nucleon Physics

This section will review the simpler case of the hadron-nucleon interaction. This will be divided into three sections where the interactions will be examined with increasing complexity. First the characteristics of the total cross section will be reviewed, that is the reaction $A + B \rightarrow anything$. Next the slightly more complex scenario of exclusive channels will be studied, that is reactions where specific decay products such as a pion or kaon are looked for regardless of what else is produced, ie $A + B \rightarrow C + anything$. Lastly exclusive channels will be examined, ie those reactions where a specific reaction is studied.

Characteristics of Total Cross Section

The most basic parameter that can be examined for hadron production cross sections is the total cross section. The total cross section is surprisingly constant with increasing energy of the incident particle as can be seen in Figure 1.3. The value of the cross section for pp interactions varies only slightly over the energy range from 5-2000 GeV and is of the order of 40 mb [33]. Other particle types have not been measured to such high energies but available data show similar behaviour at higher energies, despite different magnitudes. More variation is found at lower energies for other incident particle types. This stability of cross section occurs despite being composed of many different cross sections of individual channels which grow and die out as a function of energy. The average multiplicity of events increases with energy as can be seen in Figure 1.4 according to the formula[32]:

$$< N_{ch} >= A + B \ln s + C(\ln s)^2, \tag{1.15}$$

which is almost universally found for different beams and different targets.

Characteristics of Inclusive Cross-sections

A more detailed understanding can be achieved by looking at inclusive cross sections. Insights on inclusive cross sections came particularly from the spectrometer experiments which had good particle identification and angular resolution. First distributions of transverse momentum will be examined. These can be seen to follow an exponential law for pions, kaons and protons for fixed rapidity as can be seen in Figure 1.5 [34, 35, 36, 37]. The dependence of the distribution on transverse momentum follows the form:

$$f(x_F, p_T) = A \exp(-bp_T), \tag{1.16}$$

where the parameter A depends weakly on x_F.

It can be seen in Figure 1.6 that for pions, kaons and antiprotons the cross section increases with y_{lab} up to values of around 1.5 where the distribution levels off. For protons the behaviour is different and it can be seen that the cross section decreases with increasing y_{lab}. This is typical leading particle behaviour, where the proton

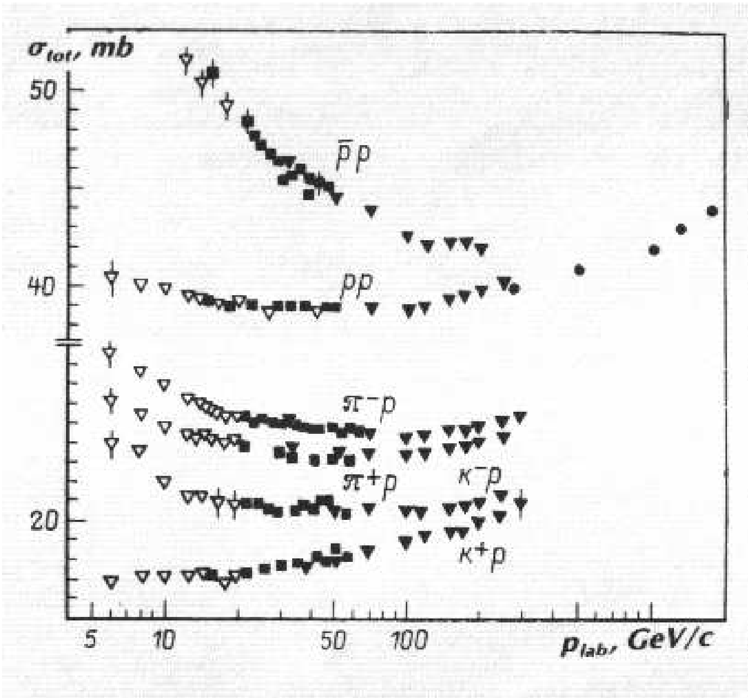

Figure 1.3: Energy dependence of hadron-nucleon cross sections [32].

appears to have 'remembered' the incoming particle. The plot is also demonstrative of the typical particle content in inclusive reactions, with the flux being dominated by pions which account for around 80 % of produced particles.

Figure 1.7 demonstrates the variation with angle of the pion cross section. It can be seen that the pions begin to peak at low momenta at smaller angles, while at larger angles the distribution is flatter. It can also be seen that at large momenta production is mainly forward, while at smaller momenta production is more isotropic.

Exclusive Cross Sections

Exclusive reactions can give useful insights into the production process leading to the resulting particle species. Information on exclusive channels comes mainly from bubble chamber data since these experiments have 4π acceptance and excellent tracking. Experiments looked at either two, four or six prong reactions and contributed to an understanding of resonance production.

The experiments showed that production of one or two mesons occurred in mainly peripheral collisions, while for three meson production the protons were deflected at larger angles and more strongly degraded in energy suggesting more central collisions. Evidence for the production of meson and baryon resonances was found and

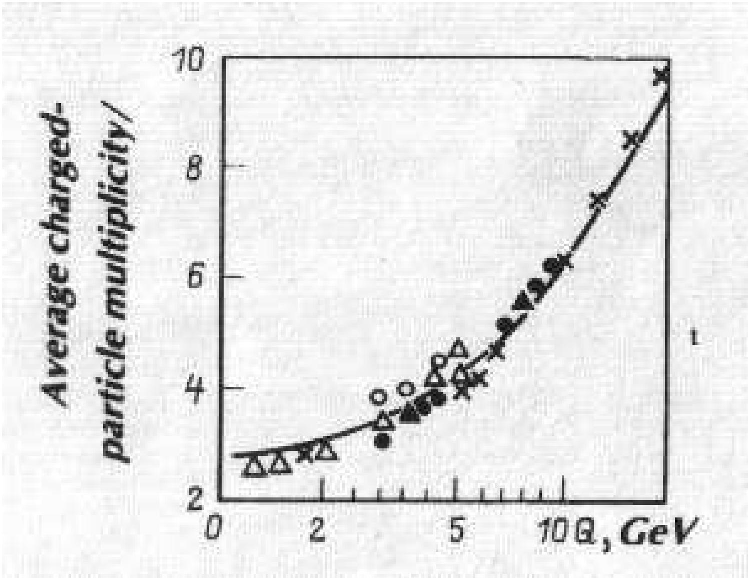

Figure 1.4: Energy dependence of multiplicity of charged secondary hadrons in hadron-nucleon cross sections [32].

the cross sections for these resonances at various energies were calculated. Both single and double resonance production were found to be important. The following channels are studied in the literature:

$$p + p \longrightarrow n + p + \pi^+ + \pi^+ + \pi^-, \tag{1.17}$$

$$p + p \longrightarrow p + p + \pi^+ + \pi^- + \pi^0, \tag{1.18}$$

$$p + p \longrightarrow p + p + \pi^+ + \pi^+ + \pi^- + \pi^-, \tag{1.19}$$

$$p + p \longrightarrow p + p + \pi^- + \pi^+, \tag{1.20}$$

$$p + p \longrightarrow p + n + \pi^+. \tag{1.21}$$

All of these reactions are found to be dominated by the $\Delta(1236)$ resonance. In reaction 1.20 the $\Delta^{++}(1232)$ is produced in association with the $\Delta^0(1232)$, $N^0(1520)$ or $N^0(1680)$ resonance in 40% of cases [39]. In reaction 1.21 evidence is also found for the $n\pi^+$ decay of the $N(1440)$ and for the $p\pi^+$ decay of the $\Delta^{++}(1920)$ [40]. There is also evidence in all reactions for the η and ω resonances, and to a lesser extent for the ρ resonance. The produced baryons are found to be strongly forward/backward peaked in the centre of mass system.

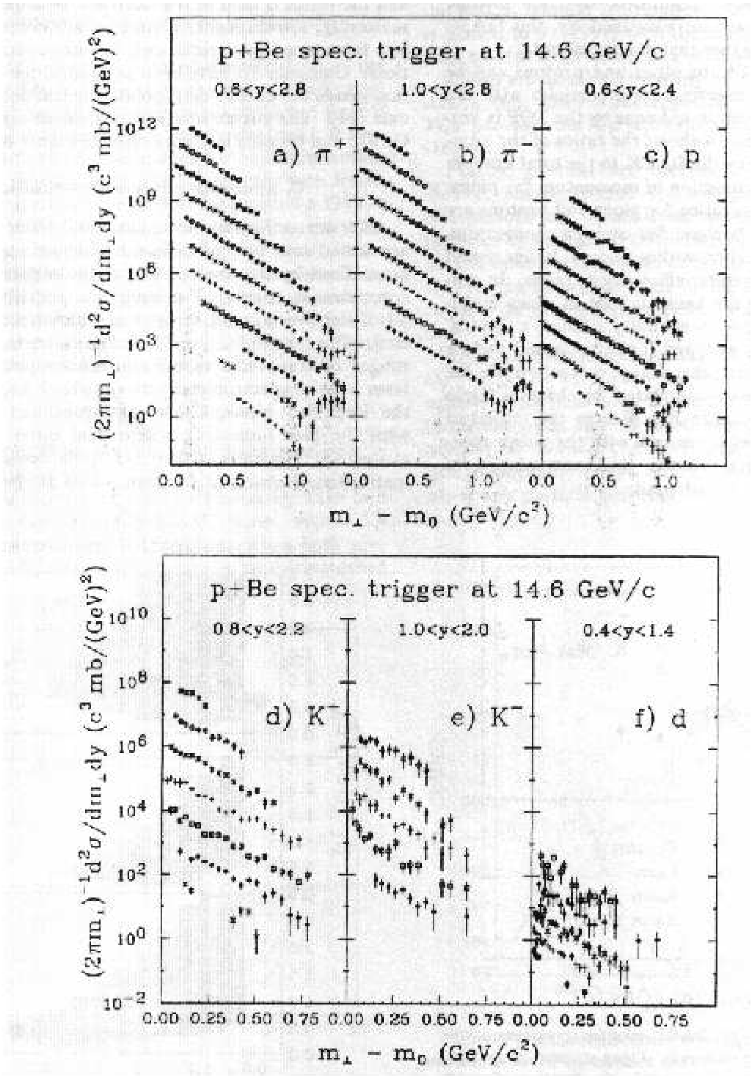

Figure 1.5: Invariant cross section as a function of transverse kinetic energy. $m_\perp$ represents the transverse component of the mass: $m_\perp c^2 = \sqrt{((m_0c^2)^2 + (p_tc)^2)}$. The different points indicate rapidity intervals of 0.2, with each successive interval being multiplied by a power of 10. [37].

1.7.3 Hadron-Nucleus Physics

In addition to the nucleon-nucleon interaction the additional effects of the nucleus on the interaction have to be considered. A measure of target thickness can be defined as:

$$\nu = A\frac{\sigma^N_{abs}}{\sigma^A_{abs}}, \tag{1.22}$$

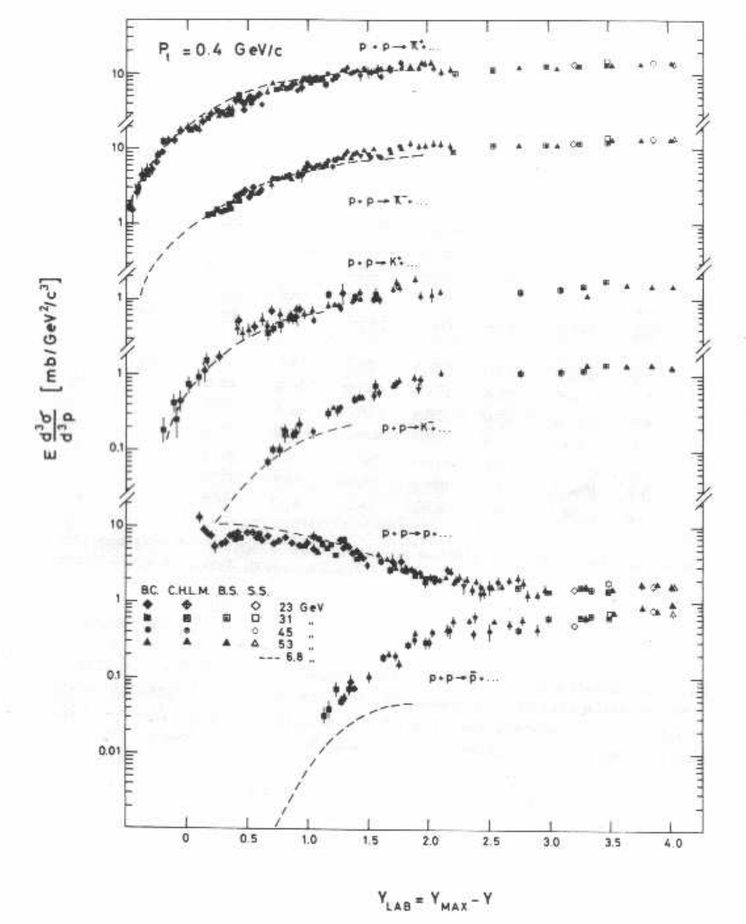

Figure 1.6: Invariant cross section against y_{lab} at p_t 0.4 GeV/c. Points represent data sets at the energies indicated and dashed lines indicate low-energy data. [34]

where $\sigma_{abs}^{N/A}$ are the absorption cross sections for a beam particle by interaction with a nucleon or the nucleus respectively. σ^A can be expressed by an empirical relation of the form:

$$\sigma^A = \sigma_0 A^\alpha, \tag{1.23}$$

where α is expected to be equal to 2/3. Experimentally values of around 0.69 are found for protons, 0.75 for pions and 0.74-0.77 for kaons [32], though the value of α has been found to be p_T dependent[41].

The average number of inelastic collisions is expected to be roughly equal to the mean interaction thickness, so experiment E910 has investigated the use of counting the number of grey tracks as a measure of the number of interactions. Comparisons with simulations show good agreement [42].

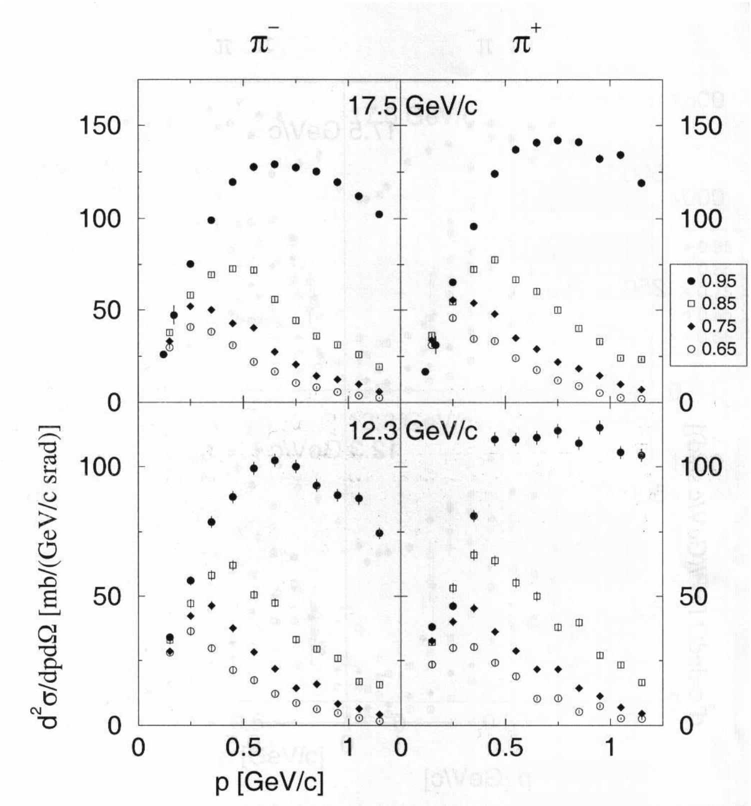

Figure 1.7: Production cross sections for π^- and π^+. The different data sets show different bins in $\cos\theta$ and the numbers in the legend indicate the centre of the bins.[38]

1.8 Hadron Production Monte Carlos

Monte Carlos simulating hadronic events are an important tool in many areas of high energy physics. They are used for studies of detector performance (particularly the energy resolution of calorimeters), predictions of induced radiation levels in materials exposed to large particle fluxes, and of course the prediction of neutrino fluxes. As has been seen above good simulations of neutrino fluxes are needed for neutrino factory design, prediction of atmospheric neutrino fluxes and calculation of fluxes in conventional neutrino beams.

Three different types of modelling are used in current hadronic generators: theory driven, data driven and parameterisation driven. Each method has different strengths and weaknesses, and different modellings are found to be well suited for different applications. For example parameterisation driven models are widely used for calorimeter simulation since they allow easy tuning of hadronic shower development. However it's clear that which ever type of modelling is used a suitable data set is essential in order to have a Monte Carlo which accurately reproduces these interactions.

The three main generators used for such purposes are FLUKA [43] and GEANT4 [44] (both developed at CERN) and MARS [45] (developed at Fermilab). Significant differences between the different Monte Carlos are observed as can be seen in Figure 1.8 which shows the pion production cross section plotted against the kinetic energy of the pion for FLUKA and MARS. While agreement is good at higher energies at low energies significant differences can be seen [46].

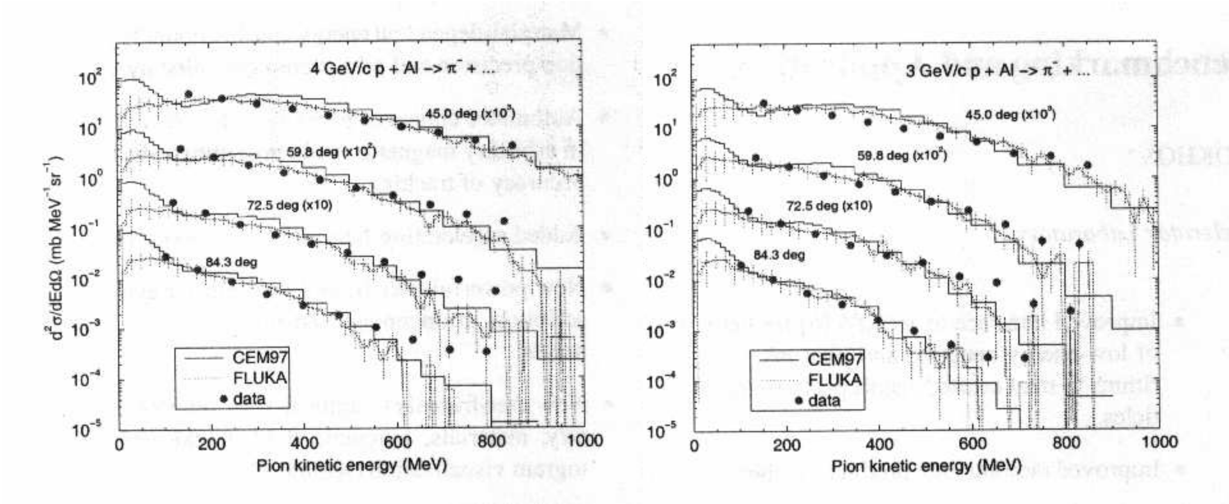

Figure 1.8: Comparison of MARS and FLUKA predictions of pion production cross section [46].

1.9 Summary

With the discovery of neutrino oscillations the planning of future neutrino experiments and the control of systematics in existing experiments is of increasing importance. In the case of existing conventional beam and atmospheric neutrino experiments, the uncertainties in the production cross section of hadrons give a large systematic error on results. Control of errors on hadron production cross sections is also of crucial importance in the design of a neutrino factory. However, hadron production data in this energy range is sparse, and this coupled with the difficulty in describing hadron production theoretically in this energy regime means that existing hadronic Monte Carlos show large discrepancies. It is therefore important for neutrino physics that this lack of hadron production data is addressed.

Chapter 2

Experimental Setup

HARP was proposed in 1999 to take hadron production data in the momentum range from 2 to 15 GeV/c, a range of momenta of interest both for the calculation of atmospheric neutrino flux and to optimise the design of a future neutrino factory. The experiment was designed to have as close to 4π coverage as possible in the range of secondary momenta of interest [30]. In order to get the experiment up and running on a fast timescale and to reduce costs many of the sub detectors were recovered from other experiments. This allowed HARP to undergo a technical run in 2000 with the experimental infrastructure in place, and to have all sub systems installed and operational by 2001. HARP then had two data taking runs in 2001 and 2002 during which it took approximately 420 million triggers.

This chapter will begin with a brief outline of the Proton Synchrotron which provides the beam for HARP. This will be followed by a description of the experimental setup.

2.1 Proton Synchrotron (PS) and T9 Beam Line

The proton synchrotron (PS) (see Figure 2.1) first began operation in 1959. The main PS ring consists of a 200 m diameter ring with three radio frequency (RF) systems and four injection and extraction systems. It is capable of accelerating protons, anti-protons, electrons, positrons and lead ions to momenta between 0.6 and 26 GeV/c [47]. PS users receive their required particle beam according to pre established sequences called super-cycles made of various magnetic cycles and lasting for 14.4 s.

The beam used by HARP is provided by protons injected into the PS at 1.69 GeV/c and extracted at 24 GeV/c. Each super-cycle extraction, called a spill, contains around 2×10^{11} protons and lasts for around 400 ms. These protons are directed to a

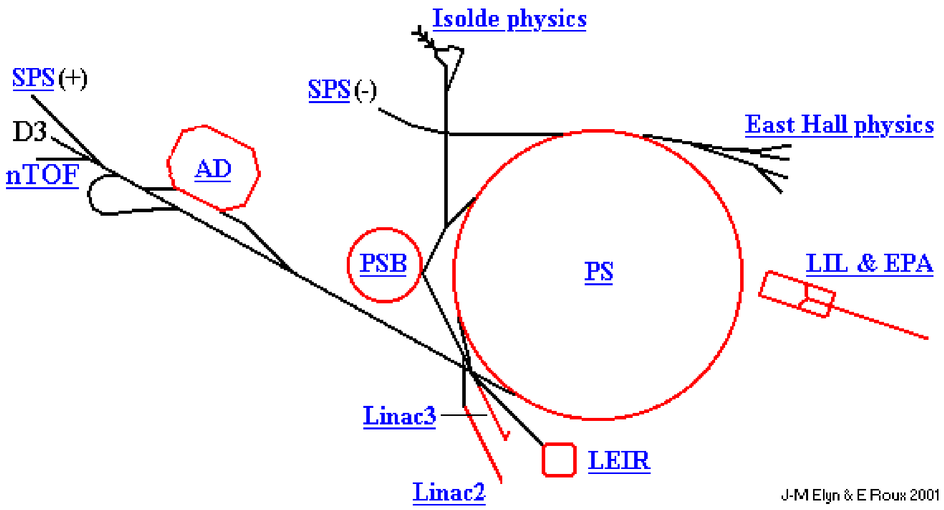

Figure 2.1: Diagram of the PS complex. [48]

primary target 55.81 m from the reference focus of the HARP experiment producing around 10^5 protons, pions and kaons per spill with momenta in the range of 0-15 GeV/c depending on the magnet settings. These particles are brought to a focus by the nine quadrupole and four bending magnets which make up the T9 beam line. The beam is further controlled by a set of vertical and horizontal collimators. These can be used to maintain the low flux required by the experiment. The result of this focusing is a beam spot with a size of approximately 5×5 mm^2 at the HARP target.

2.2 HARP Detector

A schematic diagram of the HARP detector can be seen in Figure 2.2. The sub-detectors making up the experiment can be separated into three main areas:

- Beam Instrumentation and Trigger - provides tracking and particle identification of beam particles and provides information which is used for a trigger decision.

- Large angle detectors - provide tracking and particle identification for secondaries leaving the detector with polar angles between 20° and 160°.

- Small angle detector - provide tracking and particle identification for secondaries leaving the detector with small polar angles.

The beam instrumentation consists of four Multi Wire Proportional Chambers (MWPCs) for the tracking of beam particles, and a beam Time Of Flight (TOF) system and two beam Cherenkov counters for particle identification. In addition a number of scintillator detectors in the beam are used for triggering. Tracking of secondaries leaving the target at large angles is provided by a Time Projection Chamber which also carries out particle identification by dE/dx. Additional particle identification both at large angles and in the forward direction is provided by Resistive Plate Chambers (RPCs). Tracking in the Forward direction is carried out by a series of drift chambers, with particle identification being provided by a TOF wall, a threshold Cherenkov detector and an electron identifier and muon identifier. Each subsystem will be described in the following sections.

The HARP coordinate system is defined with z along the beam axis in the direction of the beam, the y axis up wards and the x axis to the left with the beam coming from behind.

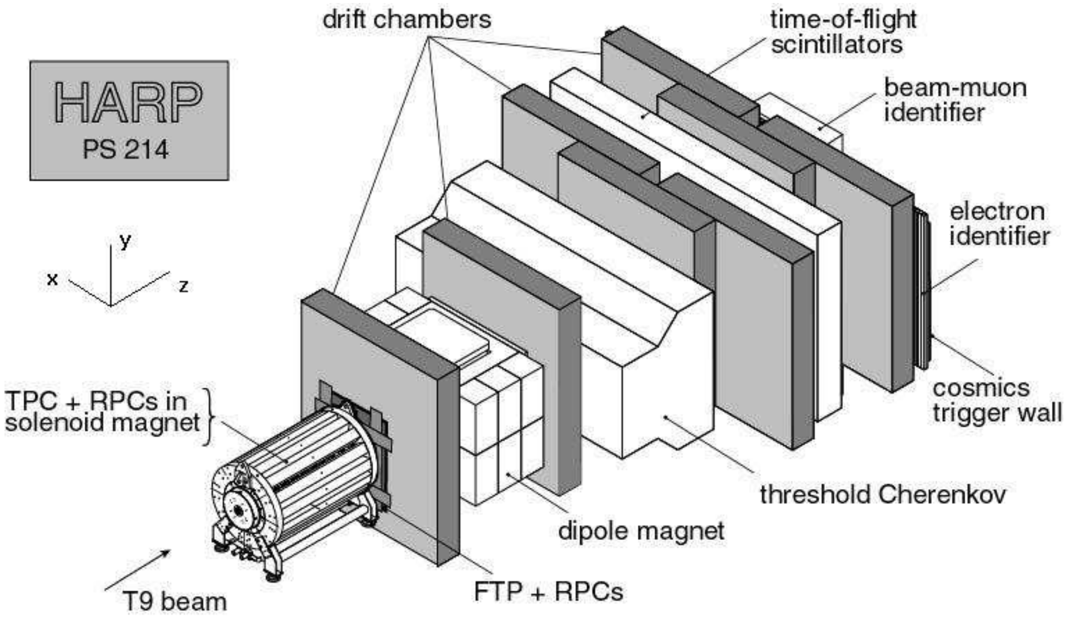

Figure 2.2: Diagram of experimental setup of HARP detector [49].

2.2.1 Beam Instrumentation

Multi-Wire Proportional Chambers

Tracking of beam particles for the monitoring of the beam profile and position, and for the reconstruction of beam particle position at the target is provided by four Multi-Wire Proportional Chambers (MWPCs) shown in Figure 2.3. Each chamber contains two 2.5 mm thick volumes filled with a gas mixture of 50 % Argon 50% CO_2, which constitute the sensitive gas volume. The sensitive volumes are enclosed by aluminised foils with 12.5 μm thick aluminium which are held at negative potential and act as cathode planes. Each sensitive gas volume contains a set of parallel tungsten wires with 10 μm radius held at positive potential which form the anode wires. When a charged particle passes through the sensitive gas volume, electron-ion pairs are produced. The electrons drift towards the anode wires due to the electric field, where an avalanche occurs causing a signal on the wire.

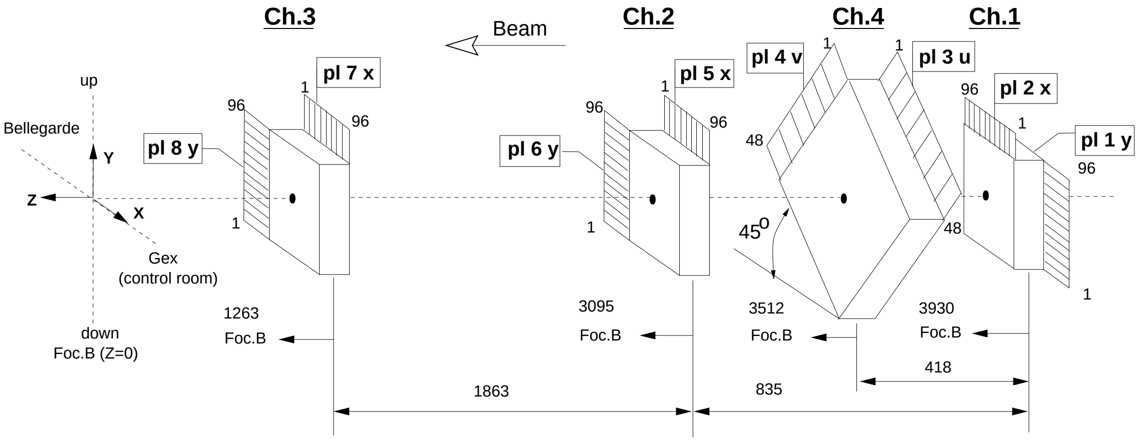

Figure 2.3: Diagram to show relative positions and orientations of MWPCs. [50]

The wires in the sensitive gas volumes of a given chamber are orthogonal allowing the xy position of a charged particle in each chamber to be measured. Three of the chambers have ninety-six wires which are read out in each plane, with a wire-spacing of 1 mm. The fourth chamber has forty-eight wires in each plane with a wire spacing of 4 mm. The fourth chamber is rotated around the z axis by 45° with respect to the other chamber with the aim of resolving ambiguities in multiple track events and to allow monitoring of the size of the beam halo. The relative positions of the four chambers are shown in Figure 2.3.

Beam Particle ID detectors

Identification of Beam Particles is provided by two beam Cherenkov counters and a Time of Flight (TOF) system. Table 2.1 summarises which particle species are separated by the beam detectors at different beam energies.

The TOF comprises two scintillator strip hodoscopes, each consisting of eight vertical strips of varying width (narrowest in the centre, widest at the outside) to roughly equalise the number of particles passing though each strip. Each strip is read out by two Photo Multipliers (PMs) at either end. A time resolution of around 140 ps is achieved [51]. Measuring the time for particles to traverse the 21.4 m

Beam Momentum GeV/c	Electron tagging	Pion tagging
< 5	BCB	TOF
5	BCA	TOF and BCB
> 5	electron id	BCA and BCB

Table 2.1: Method of identification of beam particles at different energies

between the scintillator walls provides excellent particle separation as can be seen in Figure 2.4.

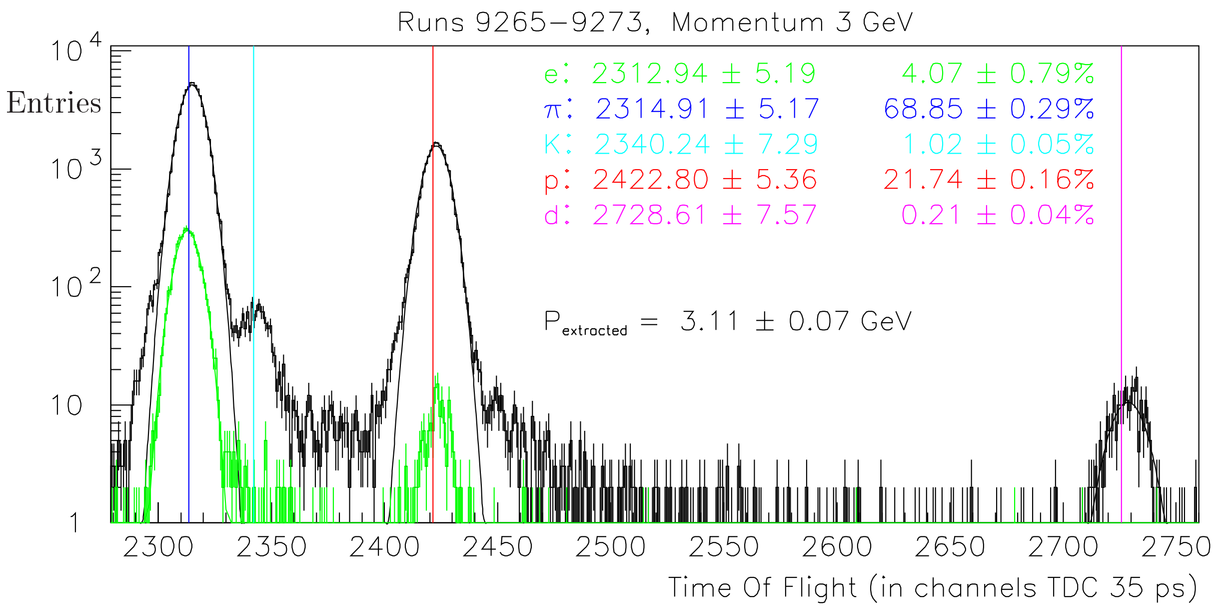

Figure 2.4: Plot showing separation provided by the TOF for a 3 GeV/c beam.[52]

The two beam Cherenkov counters are filled with N_2 gas and have lengths of 3 m and 6 m. The Cherenkov counters are operated in threshold mode. The pressure of the gas and hence the refractive index is varied according to the beam energy and which particles need to be tagged.

2.2.2 Targets

HARP aimed to take data over a large range of target nuclei. In order to cover a range from small to high A both solid and cryogenic targets were used. A list of the solid targets used can be found in Table 2.2. The targets were 30 mm in diameter due to the size of the beam. In order to minimise re interaction within the targets, solid targets of only 2 % of an interaction length were initially used. This was changed to 5 % of an interaction length in 2002 data taking in order to increase the number of useful triggers. In order to study secondary interactions and to be able to correct for these in thin target data thick targets 100 % of an interaction length thick were also used. In addition to these standard cylindrical targets, data was also taken with replica targets from the K2K and MiniBoone experiments to provide measurements allowing these experiment to reduce systematics in calculations of neutrino fluxes from their targets.

Material	Z	0.02λ (cm)	0.05λ (cm)	1.0λ (cm)	Comments
Be	4	0.81	2.03	40.70	
Be	4				0.5 λ (MiniBooNE)
Be	4				MiniBooNE target replica
C	12	0.76	1.91	38.1	
Al	13	0.79	1.97	39.44	
Al	13				0.5 λ (K2K)
Al	13				K2K target replica
Cu	29	0.3	0.75	15.0	
Cu	29				button target
Cu	29				skew target
Sn	50	0.45	1.11		
Ta	73	0.22	0.56	11.14	
Pb	82	0.34	0.85	17.05	

Table 2.2: Targets used in the HARP experiment

In order to cover as close to the full solid angle of particle production as possible the target is positioned well inside the TPC at approximately 500mm from the upstream end. For this reason it was necessary to minimise the material in the target's support structure as much as possible [53]. A picture of the support structure is shown in Figure 2.5. Each target was mounted in a cylindrical support cap made of 0.3mm thick aluminium. This support structure fitted inside a target arm. The target arm was made from aluminium with an internal diameter of 42mm and a thickness which tapered from 14mm at the upstream end to 4mm at the downstream end[1]. This arm was strong enough to ensure that the position of the target arm was maintained even when heavier targets were used. In order to be able to reliably change the target quickly and accurately for the large number of settings which were used, the target arm was mounted to a chariot which slid on rails allowing the target to be easily removed from the TPC and accurately repositioned.

[1]The target arm was changed to a carbon fibre version for 2002 data taking.

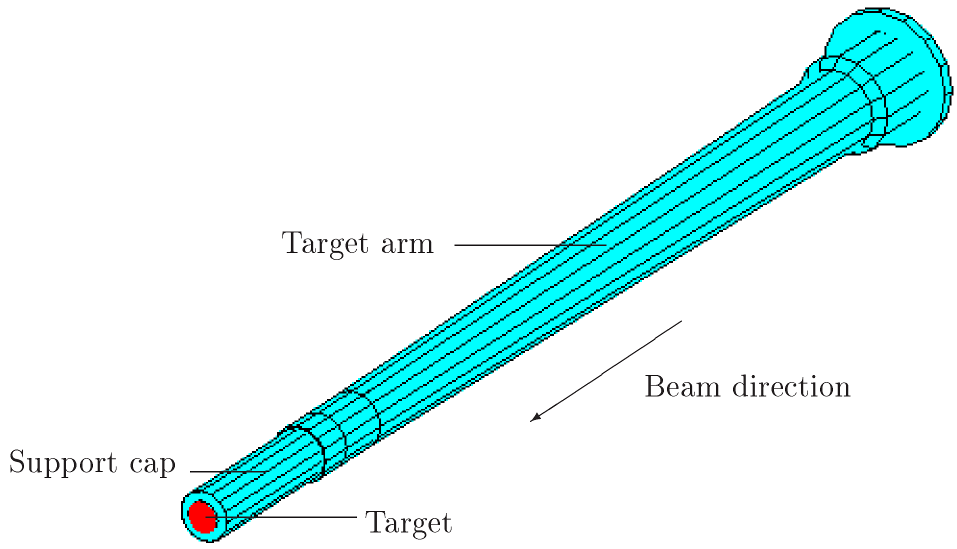

Figure 2.5: Picture of the target and its support. [53]

A series of cryogenic targets were also used. H_2 and D_2 targets were used, in order to be able to understand the interplay between hadron-hadron interactions and hadron-nucleus effects. Data was also collected with O_2 and N_2 targets to provide information for calculations of atmospheric neutrino flux. The target envelope consists of a 125 μm thick mylar envelope with a diameter of 35 mm. The entrance window has a diameter of 20 mm defining the effective diameter of the target. This is placed inside a cylindrical aluminium cryostat with 250 μm thick mylar windows.

2.2.3 Trigger

The HARP trigger system has the aim of enhancing the number of useful events recorded. This is done in two ways: the selection of beam particles and the selection of interaction events. Figure 2.6 shows the relative positions of the detectors making up the trigger.

The beam scintillator (BS) is located 4.1m upstream of the target. It consists of an 80×80 mm^2 scintillator with 5 mm thickness. It is read out by one PM, and in coincidence with a signal from TOFB it provides the lowest level of trigger (STROBE).

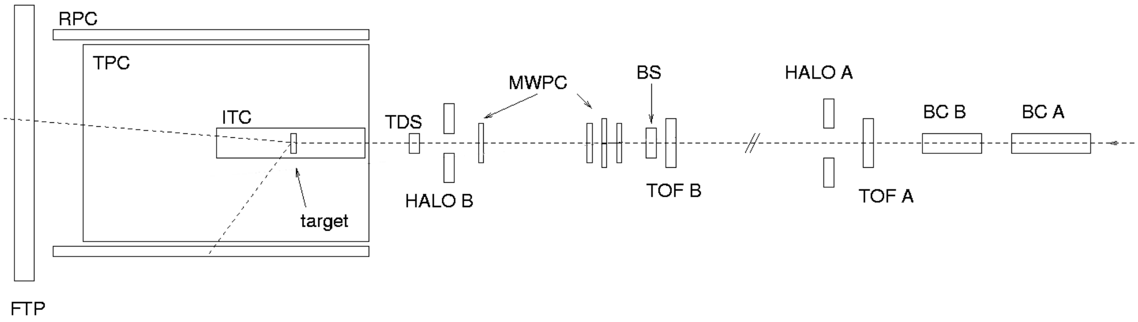

Figure 2.6: Diagram showing approximate positions of the trigger detectors. [54]

Events where a beam halo particle is present are eliminated by two halo counters. Halo A (HA) is located 25.32 m upstream of the target and has a hole of 90 mm diameter. Halo B (HB) is located 1.51 m upstream of the target. It consists of an 11 mm thick lead plate to convert gammas sandwiched between two scintillator slabs. The hole size of 30 mm is consistent with the target size.

The Target Defining Scintillator (TDS) is designed to select with high efficiency beam particles which will definitely hit the target. It consists a circle of scintillator with 20 mm diameter, significantly smaller than the target and is located 1.14 m upstream of the target. It is read out by four PMs and gives a signal if at least one PM records a signal. This gives very high efficiency (>99.9%) [55].

Along with the beam TOF these triggers define the BEAM trigger which consists of:

$$BS \times TOFB \times TDS \times TOFA \times \overline{HA} \times \overline{HB}. \tag{2.1}$$

For thick target runs where an interaction is expected in most events (since the target is 100 % of an interaction length thick) the BEAM trigger is enough to have a very high proportion of interaction events. However for thin target settings where a trigger is only expected in a small percentage of events the number of interaction events must be enhanced. This is done using two additional trigger detectors.

The Inner Trigger Cylinder (ITC) triggers on secondaries leaving the target at large angles with respect to the beam axis. It consists of an aluminium/carbon cylinder of length 1300 mm and with an inner diameter of 76 mm. Six layers of scintillating fibres are glued onto the tube. The first four layers are parallel to the beam axis, and the top two are at an angle forming helices. The detector is read out by twenty-four PMs. Only one channel is required for a signal and this gives the ITC an efficiency greater than 99 %.

The Forward Trigger Plane (FTP) triggers on secondaries which leave the target at small angles with respect to the beam axis. It consists of two planes of $1240 \times 200 \times 5$ mm^3 scintillator slabs at 90° to each other with a central hole of 20 mm diameter. An OR of the FTP and ITC provide the interaction trigger for thin target runs.

2.2.4 Time Projection Chamber

The Time Projection Chamber (TPC) is the central tracking chamber of the HARP experiment and provides both tracking and particle identification of secondaries that leave the target at large angles with respect to the beam axis. The TPC is able to provide 3D tracking information with the xy positions being provided by the location of the pads on which a signal is measured and the z dimension being provided by the timing information. The TPC sits inside a solenoid magnet which provides a 0.7 T magnetic field parallel to the axis of the TPC. This causes the curvature of tracks allowing the determination of their momentum via the parameters of a helical fit. Particle identification is provided by energy loss by ionisation (dE/dx). A plot of dE/dx against momentum for a typical TPC can be seen in Figure 2.7.

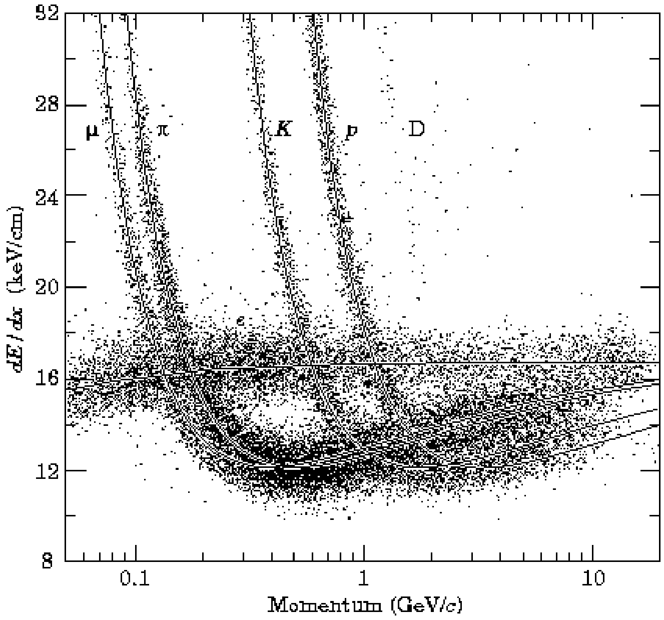

Figure 2.7: An example of dE/dx measurements in the PEP4/9-TPC. [6]

The HARP TPC has a total length of 2020 mm with an active volume with a length of 1550 mm. The active volume is filled with a gas mixture comprising Ar (91%) and CH_4 (9%). Passing charged particles produce electron ion pairs. A Minimum Ionising Particle (MIP) produces a primary ionisation of 50 electrons/cm. The electrons produced are drifted by the TPC's electric field of 110 V/cm at a speed of about 5.17 cm/μs toward the plane of anode wires at the downstream end of the TPC where an avalanche occurs, inducing signals on the pad plane.

Field Cage

The electric field in the TPC is provided by a high voltage membrane at the downstream end held at -17.1 kV, anode wires at a voltage of 1820 V at the upstream end, an Outer Field Cage (OFC) and an Inner Field Cage (IFC) [56]. A diagram of the field cages can be seen in Figure 2.8. The field cages have a series of conductive strips kept at precise potentials designed to keep the field uniform [56]. Each field cage is made from a stesalite cylinder 8 mm(2 mm) thick and 1541 mm(799 mm) long for the OFC(IFC). The surface facing the drift space has a series of 10 mm wide potential rings of printed copper on a kapton foil with 1 mm gaps, with a series of bars placed on top; 24(12) for the OFC(IFC). The bars support 10 mm metallised mylar strips separated by 1 mm gaps. The upper strips are offset by half a period with respect to the lower strips. The layer of strips closest to the gas volume mainly determine the field while the second layer reduces distortions close to the barrel. In the OFC a third layer of strips is placed inside the stesalite to shield the chamber from ejection field [2]. For the IFC this cannot be done due to a lack of space, instead this role is performed by five strips of increasing potential etched on the inner surface of the IFC.

Wire Planes

The electrons produced are drifted by the field toward the readout chamber at the upstream end of the TPC. They first reach the gating grid 16 mm from the pad plane. The gating grid consists of 70 μm Cu and Be wires with a wire pitch of 2 mm. The gating grid operates in two modes (see Figure 2.9). If there is no signal from the trigger the wires are alternately held at +35 V and -35 V. This prevents ions from drifting back into the main volume. If a signal is received from the trigger all wires are held at -67 V, the nominal voltage for the TPC electric field at this z position. Next the electrons reach the cathode plane 10 mm from the pad plane. This consists also of 70 μm Cu and Be wires with a 2 mm pitch held at 0 V. From here the electrons avalanche toward the anode wires which are 20 μm W and Au wires with a 4 mm wire pitch held at a high positive potential of 1820 V.

[2]These are fringe fields in the proximity of conductors. If they occur in the TPC gas these can cause ionisation or sparks.

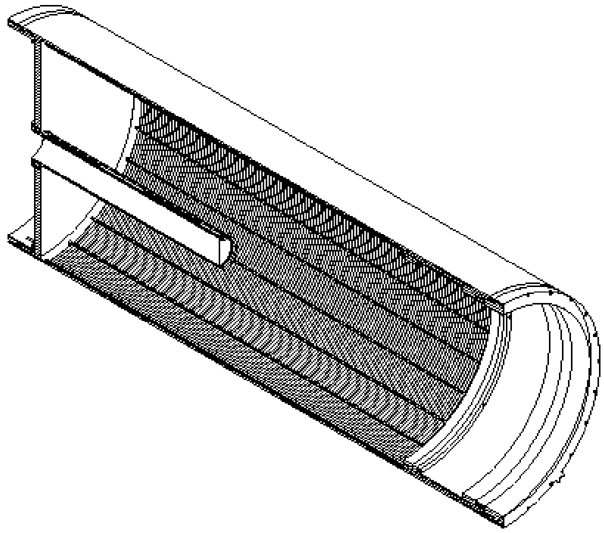

Figure 2.8: Diagram showing the Inner Field Cage and Outer Field Cage of the TPC. [56]

Readout

After the electrons have avalanched to the wire a cloud of positive ions remain which induce a negative signal on the pad plane. The Pad Plane of the TPC has six sectors. Each sector is a six layer printed circuit board (PCB) with the pads on one side and the electronics on the other. The pads are arranged in twenty rows of concentric rings, with each pad having a size of 6.5×15 mm. There are a total of 662 pads in each sector giving a total of 3972 pads for the whole TPC.

The Analogue to Digital Converters (ADCs) sample analogue signals with a clock frequency of 10 MHz. Physics events consist of 300 samples which cover the 30 μs drift time of the TPC. Zero suppression is applied to reduce the data volume and increase the number of useful events which can be recorded. This means that only pads with samples which are 10 ADC counts above the pedestal are recorded. In addition to signals above threshold two pre samples and two post samples[3] are also recorded. Data is stored in 10 bit words preceded by a 32 bit header which contains information about the pad.

The signal which is seen by the readout electronics represents the response of the electronics to the signal induced on the pad. For the TPC the response of the electronics to a delta function is well represented by a gamma function.

[3]These numbers are for 2002 data taking.

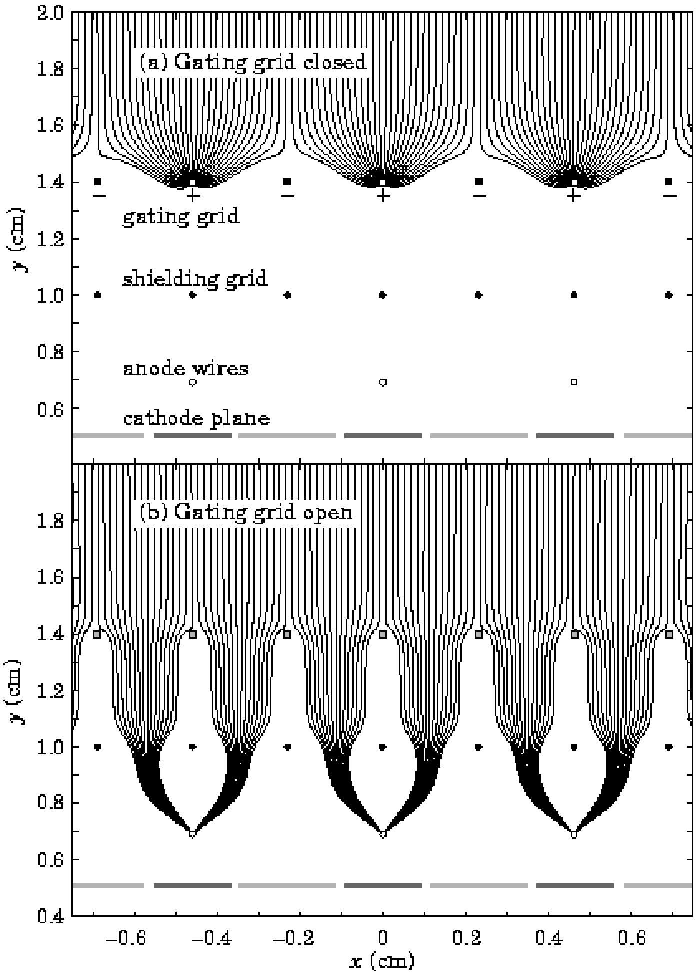

Figure 2.9: Field lines when wires are held at opposite potentials (top) and field lines when wires are held at nominal potentials (bottom). [6]

$$\frac{t^2}{\tau^2}\exp(-\frac{t}{\tau}), \tag{2.2}$$

where τ is of the order of 70 ns.

Cross Talk Effect

During HARP's 2002 data taking a cross talk effect was noticed in the TPC [57]. The effect is caused by the preamplifier output lines in the PCB passing in proximity to the input lines of other pads. This amounts to a capacitive coupling between the output signal of one pad and the input signal of a second satellite pad, causing unwanted signals on the satellite pads. The coupling is of the order of pF and approximately 50% of pads talk to other pads. This clearly has serious consequences on the ability to accurately reconstruct momentum and on dE/dx measurements. This topic will be covered in greater detail in the subsequent chapters.

Field Distortions

It was discovered after data taking was complete that the HARP TPC suffered from field distortions due to a 2.4 % voltage misalignment between the inner and outer field cages. Calculation of the field distortions caused by this can be seen in Figure 2.10 [58].

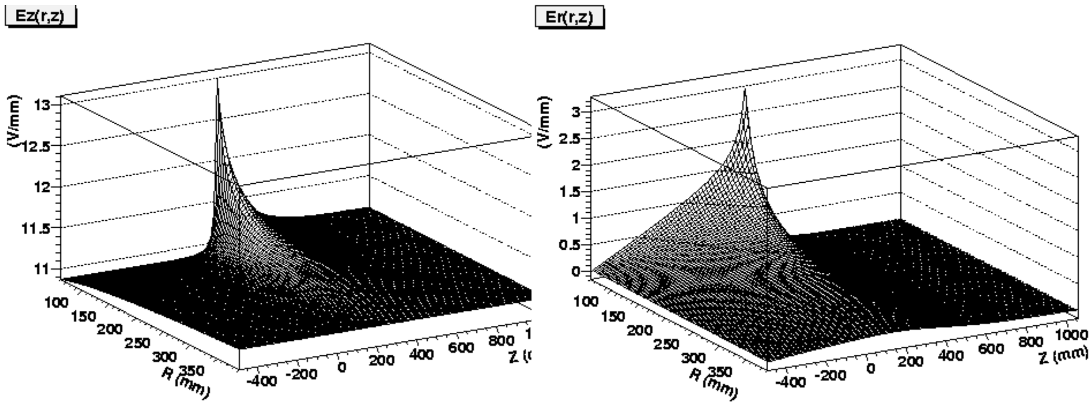

Figure 2.10: Electric field distortions [58]

Calibration

Since the TPC is used for particle identification using dE/dx it is necessary to perform accurate pad equalisation. Pad equalisation is the process of calculating the responses of different pads to the same amount of charge in order to calculate a gain factor for each pad. In HARP this is done using two methods, by the use of cosmic rays and with radioactive Krypton-83 and Iron-55.

Cosmic rays produced in the upper atmosphere produce straight tracks in the TPC. Information from the RPCs is used to provide a trigger for these events. Cosmic events are taken between spills from the PS and also in dedicated cosmic runs. Since the energy deposited along a cosmic track should be constant these tracks can be used to calculate the relative gain factors of different pads. Since the distribution of cosmic events is not uniform with angle the gain factors on some pads have higher errors than others.

This method is complemented by pad equalisation done by the injection of radioactive Krypton-83 into the detector volume. The Krypton decays and by a combination of internal electron conversions, Auger electrons and photons, produces electrons with energies between 9.4 and 41.6 keV. This spectrum of processes can be reconstructed and used to calculate gain factors.

In addition to these calibration systems to measure gain factors, the TPC has a laser system to monitor the drift velocity in the gas, which is pressure and temperature dependent, and to study the effects of field inhomogeneities. Laser light is shot from 196 200 μm optical fibres producing photo electrons which cause ionisation.

2.2.5 Resistive Plate Chambers

The Resistive Plate Chambers (RPCs) provide electron/pion separation at low momentum (150-250 MeV/c), where this is not possible using dE/dx in the TPC [59]. There is a sizable rate of electrons at this energy resulting from the conversion of γ's from π^0 decays. The RPCs utilise time of flight measurement over the distance from the target (of the order of 40 cm) to provide particle identification.

Each RPC has four 0.3 mm thick gas gaps filled with $C_2F_4H_2$ (90%) isoC_4H_10 (5%) SF_6 (5%). The gas gaps are separated by six 1 mm glass plates. The outer and central glass layers are coated in a layer of graphite, and these graphite layers serve as a HV electrode and ground respectively. Charged particles passing through the detector ionise the gas. A fast avalanche then occurs as a result of the electric field. This induces a signal in the central plane which is read out. The time resolution of the RPCs is of the order of 150 ps.

Each RPC measures 11 mm $\times$ 140 mm $\times$ 2178 mm and the gas and glass layers are housed in an aluminium casing. Each RPC unit contains two layers of eight pads. The layout of the forty-six units can be seen in Figure 2.11. Thirty RPCs sit in the 24 mm space between the TPC and the solenoid coil. These are placed in two overlapping layers of fifteen RPCs. There is also a layer of forward RPCs at a distance of 1800 mm from the target. Two sets of four counters are placed horizontally 245 mm from the beam axis and two sets of three counters are placed vertically at a distance of 145 mm from the beam axis, allowing them to cover a medium angle region not covered by the forward spectrometer.

2.2.6 Nomad Drift Chambers

Tracking of secondaries produced at small angles with respect to the beam axis is done using twenty-three Nomad Drift Chambers (NDCs) recovered from the NOMAD experiment [60]. Each NDC consists of three 8 mm gas gaps, each containing

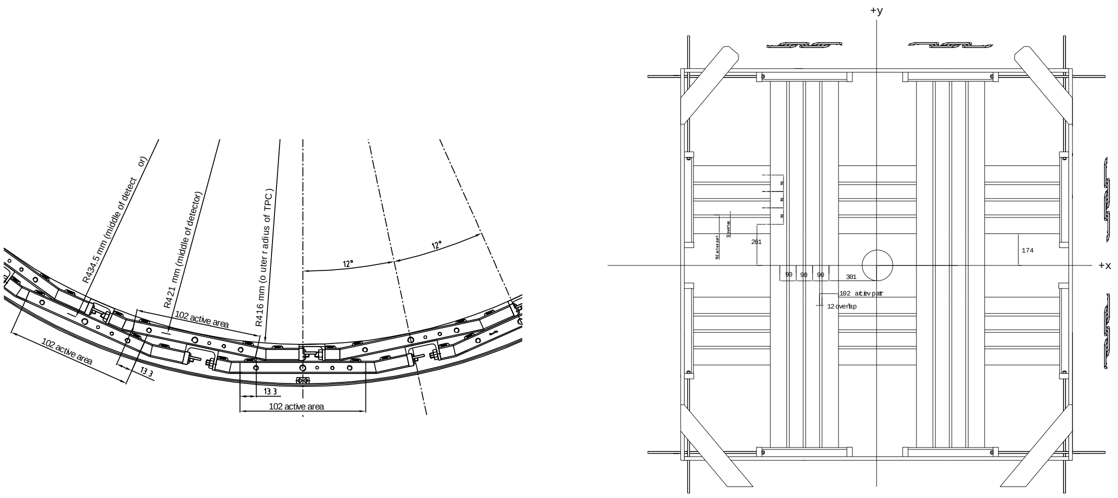

Figure 2.11: Arrangement of barrel RPCs (left) and forward RPCs (right) [59].

a plane of wires with 64 mm wire spacing. The wires in the central plane are vertical, and those in the first and third are orientated at +5° and -5° with respect to this. This orientation provides good precision in the horizontal direction in which the momentum measurement is obtained. The gas volumes are filled with a 90% Argon, 9% CO_2 1% CH_4 gas mix. As a charged particle traverses the gas volume the gas is ionised causing an avalanche at the sense wires.

Chambers are arranged in sets of four within a module. The positions of the modules can be seen in Figure 2.2. The first two drift chambers are placed either side of the dipole magnet and allow the measurement of the momentum of forward going particles. The dipole magnet provides a field in the centre of 0.5 T. There are also planes of NDCs in front of the forward particle ID detectors allowing an accurate entry point and angle to be attained.

2.2.7 Cherenkov Detector

The Cherenkov detector gives particle identification of secondaries in the forward direction with high momentum (> 3 GeV/c). It works on the principle that particles with $\beta > \frac{1}{n}$ (where $\beta = v/c$ and n is the refractive index of the medium) produce Cherenkov light which can be detected and measured. The thresholds in the HARP Cherenkov counter for different particles are shown in Table 2.3. The number of photo electrons produced depends on the velocity ($N_{photons} \propto (1 - \frac{1}{\beta^2 n^2})$) meaning that as well as discrimination between particles which are above and below threshold it is possible to discriminate between different particles above threshold via the number of photo electrons produced.

The Cherenkov counter is located 6 m downstream of the target between the

Particle	Threshold momentum GeV/c
pions	2.6
kaons	9.3
protons	17.6

Table 2.3: Thresholds for Cherenkov light for different particle types in the HARP Cherenkov detector.

second and third drift chambers. The detector is filled with C_4F_{10} gas at high density. The high refractive index of this gas means that it can be used at atmospheric pressure. The light which is produced in the gas is guided by two rows of twelve mirrors, made of plastic with an aluminium coating, toward two rows of nineteen Winston cones each with a 340 mm diameter entrance where it is collected by a PM. The PMs are separated from the gas volume by a sheet of Schott B270 glass in order to allow the possibility of the replacement of photo multipliers during operation.

2.2.8 Time of Flight Wall

The Time of Flight (TOF) Wall provides particle identification for low momentum particles in the forward direction. It gives a high precision measurement of the flight time of particles over the 10 m distance from the target to the TOF wall. This along with the momentum information from the NDCs allows particle identification [61].

The TOF wall has an active area of 657 $\times$ 243 cm^2. The main wall consists of thirty-nine scintillator slabs, arranged in three vertical walls, each consisting of thirteen slabs (see Figure 2.12). The slabs in the outer walls are 250 cm high and those in the middle wall, where the high momentum particles are expected, are 180 cm high for better time resolution. All slabs are 21 cm wide, allowing good segmentation, and 2.5 cm thick. In each wall the counters partially overlap to provide hermetic coverage. The counters are wrapped in aluminium foil and sealed with black plastic to screen outside light.

The TOF wall has two calibration systems. It uses cosmics and a laser calibration system. Two extra sets of scintillation counters are placed upstream and downstream of the TOF wall to trigger on cosmic events with fixed azimuthal angle ϕ=50°. These are: three downstream counters (two horizontal and one vertical), two large horizontal upstream counters and a strip of thirteen short horizontal scintillators which are also upstream. These are removed during normal runs to avoid the presence of extra material. In addition the centre of each counter in the main wall has a small quartz prism attached to a fibre allowing the injection of laser light.

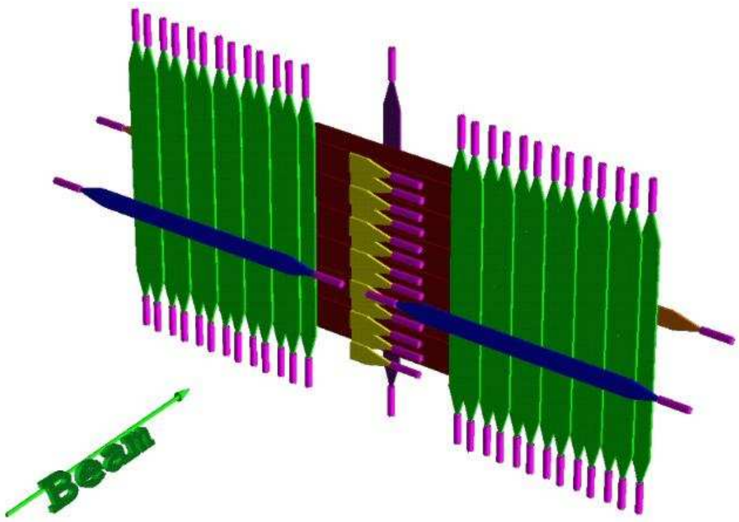

Figure 2.12: Diagram of the Time of Flight detector of the HARP experiment [62].

2.2.9 Electron Identifier

The primary purpose of the electron identifier is to discriminate pions from electrons when charged pions accompanied by knock-on electrons are identified as electrons by the Cherenkov counter [63]. It also takes the additional role of detecting π^0s. Identification of π^0s is accomplished through the invariant two-gamma mass under the assumption that both gammas originate at the target centre.

The detector consists of several components. The first of these is a 2 cm thick iron plate which converts a large fraction of γ from π^0 decay. Three NDCs are next downstream. These modules have only one chamber read out and provide an entry point for the γ. This is followed by two layers of lead and scintillator fibres (spaghetti calorimeter) which were previously used by CHORUS.

The two calorimeters have differing dimensions to match electromagnetic and hadronic shower development. The first are the electromagnetic (EM) modules. Each module is made from twenty-one layers of extruded lead containing scintillating fibres of 1 mm diameter and 2.62 m length. The fibres are collected on both sides into two different groups to give two independent counters. The fibre groups are coupled to a light guide which is itself coupled to a PM. Each module is 4 cm thick corresponding to 5.37 X_0 (0.19 λ_{int}). The second layer contains Hadronic (HAD1) modules. Each of these modules is made from forty-three layers of extruded lead, containing scintillating fibres 1 mm wide and 3.35 m long. This time the fibres are collected into a single bunch on each side and coupled through a light guide to a PM. Each of these modules is 8 cm thick corresponding to 11.0 X_0 (0.4 λ_{int}) .

The detector also has a cosmic wall which along with the TOF wall provides a cosmic muon trigger for detector calibration. This consists of thirty vertical scintillator slabs 320 cm high and 20 cm wide. These are unevenly spaced to give full coverage of the EM and HAD1 calorimeters. Each end is coupled through a light guide to a PM.

2.2.10 Muon Identifier

The detector furthest downstream is the muon identifier. It has two main purposes. First, identification of muons will help to detect decays in flight of pions and kaons. At momenta of 2 GeV/c these have a non negligible probability (5 % for pions and 40 % for kaons). These decays can produce wrong longitudinal and transverse momentum assignment and a possible pion/kaon confusion due to an increase of flight time when a pion decays in the Cherenkov counter. It also allows the muon content of the beam to be measured.

The muon identifier consists of a 40 cm iron block followed by five scintillator planes. Each plane consists of six horizontal scintillator slabs 200 cm $\times$ 6 cm $\times$ 2500 cm. Each of these planes of scintillator is separated by three or four 5 cm iron plates. Each scintillator slab is read out at both ends. The detector is asymmetric in the horizontal direction with respect to the beam line. This is to enable it to detect beam muons of all beam momenta which are horizontally deflected by the spectrometer magnet. Two vertical scintillators are positioned to provide a signal for the local trigger.

2.3 Summary

The HARP detector provides tracking and particle identification of both beam particles and secondaries leaving the target at both large angles and small angles. Large angle tracking is provided by a TPC, which, complimented by a layer of RPCs also provides particle identification in this angular region. Small angle tracking is provided by NDCs and small angle particle identification is provided by a Cherenkov counter, TOF wall and electron and muon identifiers. This gives HARP almost 4π acceptance in the momentum range of interest for hadronic physics requirements of neutrino factory design, the calculation of atmospheric neutrino flux and calculations of neutrino fluxes for conventional beams. This acceptance coupled with a selection of targets ideally suited to these purposes mean that HARP will be able to provide measurements of crucial importance to the future of neutrino physics.

Chapter 3

Beam Particle Reconstruction

This chapter describes the software written to reconstruct beam particle trajectories. Reconstruction of beam particle positions has two main roles. First, it is necessary during data taking in order to monitor the beam, and check that it is well centred on the target. Secondly it is needed during analysis to select good incoming beam particles and determine the impact position of beam particles on the target.

Tracking of beam particles is done using the Multi Wire Proportional Chambers (MWPCs) which were described in chapter 2. The chapter will begin with a brief recap of the features of the MWPCs which are pertinent to the reconstruction software. The software reconstructing the beam particle trajectories will then be described. Next a description of the simulation of the HARP beam will be given along with a description of the simulation of the MWPC detector response. The chapter will end by showing the performance of the reconstruction in terms of efficiency and accuracy as found using the simulation.

3.1 The Multi Wire Proportional Chambers

The beam particles are tracked by four MWPCs. Each has two orthogonal wire planes. Three 'small' chambers have two planes of ninety-six wires with 1 mm spacing which measure the x and y directions. The fourth 'big' chamber has two planes of forty-eight wires with 4 mm spacing. This chamber is rotated by 45° with respect to the other three chambers. This was done in order to resolve possible ambiguities in events with more than one incoming beam particle and also to be able to better measure the size of the beam halo. The MWPCs only have digital readout, and so there is only information available about the closest wire (or wires in the case of inclined tracks) to a passing beam particle.

3.2 MWPC Reconstruction Software

The HARP software framework includes a package called 'Kalman' which is responsible for applying the Kalman filter technique to tracking and vertex fitting in all sub detectors. This section will begin with a description of the algorithms which constitute the MWPC reconstruction software. A brief overview of the theory behind the Kalman filter will then be given along with a description of how the MWPC reconstruction software interfaces to this package.

3.2.1 Reconstruction Algorithms

The reconstruction of beam particles is done via a series of algorithms and objects (see Appendix A for a description of the role of algorithms and objects). A schematic diagram of these can be seen in Figure 3.1. The algorithms carry out all processes which are necessary to turn the raw data, which contains the information on which wires were hit in each event and the information on wire positions contained in the geometry and alignment files, into reconstructed tracks. These algorithms will be described in order below.

The first algorithm LoadMwpcCAAlg reads information from the MWPC geometry file and the MWPC calibration and alignment file which contains the alignment constants for each chamber of the MWPCs. It stores this information into objects which hold information about the position and size of each chamber plane and wire which can be used by the following algorithms.

The information from each event is read from the database and stored into MwpcHit objects by ObjectCnvAlg. Since the MWPCs only record the presence or absence of a hit it is only necessary for these objects to hold the chamber, plane and wire number in order to completely define a hit. Each object also contains a pointer to an MwpcWire object. This allows it to access information on its position. It is necessary for the addition of this pointer to be done in a separate algorithm, UpdateMwpcHitsAlg, due to the dependencies which are allowed by the software framework. The MwpcHit objects then contain all information necessary to perform complete reconstruction.

The first reconstruction algorithm CreateMwpcClustersAlg creates clusters. A cluster is defined as a series of hits which occur on consecutive wires. A cluster of more than one hit can indicate a track which crosses two cells (where a cell is the volume which is defined by $wireposition \pm \frac{wirespacing}{2}$ in the measurement direction). This is not expected to happen very often as can be seen in Figure 3.2 which shows the track inclinations from a typical run. Otherwise it indicates the production of

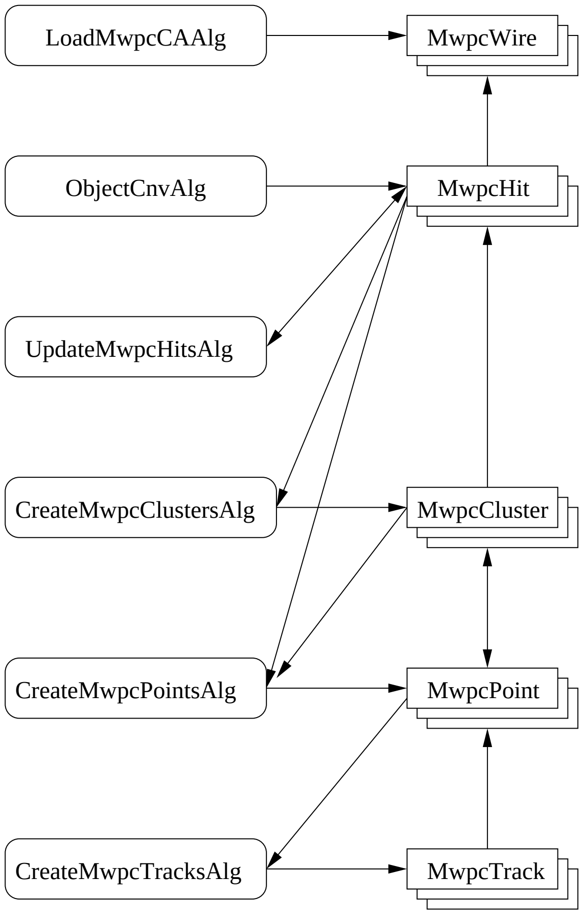

Figure 3.1: Diagram of inter-relation of objects and algorithms used for MWPC reconstruction. Square edged boxes indicate data objects and round edged boxes indicate algorithms.

a delta electron as the beam particle traverses the sensitive gas volume. In either case only one track should be reconstructed from a cluster.

The next algorithm CreateMwpcPointsAlg combines hits coming from the two planes of an MWPC to create a 3D point. The algorithm creates all possible points. So if, for example, a chamber has two hits in each plane, then four points would be created. Each point contains a pointer to the hits from which it was created, allowing the position to be calculated, and to the clusters to which the two hits belong.

The final algorithm is CreateMwpcTracksAlg which decides which hits belong to the same track. An MwpcTrack is created from a vector of MwpcPoint objects. The constructor of each track calls the Kalman package which carries out the track

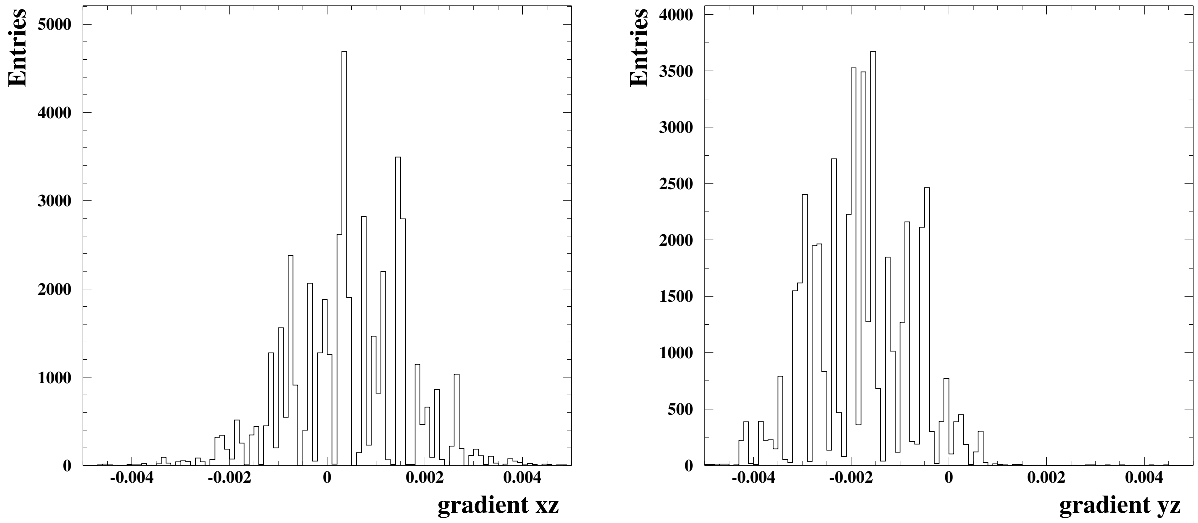

Figure 3.2: Distribution showing typical reconstructed track inclinations for a typical 15 GeV/c run. Inclination in the xz plane is shown on the left and yz on the right.

fit. The first preference is for a track created using a point in each chamber. The algorithm iterates through the points looking for all possible tracks made from a combination of one point from each chamber. If more than one track candidate exists then the track with the lowest χ^2 is taken. All points which belong to a cluster which was used in this track are deleted. The process is then repeated. Once there is no longer a point remaining in each chamber the algorithm attempts to make a track using just three points. Again if more than one track is possible the one with the lowest χ^2 is taken. Once a three point track has been made the algorithm checks if a single hit in the chamber which was not used exists. If a hit exists then this information is added to the track object, and the track is refitted.

3.2.2 Track Fitting Using the Kalman Package

Whilst the process of track selection is done by the MWPC reconstruction software, the track fitting and calculation of χ^2 values is done by the Kalman filter. A brief description of the principle of a kalman filter will be given followed by a brief description of how the MWPC software makes use of the Kalman package which does these calculations.

The Kalman technique involves doing track fitting by describing the track as a linear dynamic system [64, 65, 66]. A track in space can be described by a five dimensional state vector:

$$\mathbf{x} = (x, y, \frac{dx}{dz}, \frac{dy}{dz}, \frac{1}{p}), \tag{3.1}$$

where x, y and z are the spatial coordinates and p is the particle's momentum at that measurement point. The measurement point is defined by its position in z.

The evolution of this state vector can be described by a system of linear equations:

$$\mathbf{x}(z_k) = \mathbf{x}_k = \mathbf{F}_{k-1}\mathbf{x}_{k-1} + \omega_{k-1}, \tag{3.2}$$

where $\mathbf{x}_{k-1}$ represents the state vector at the previous measurement, $\mathbf{F}_{k-1}$ represents the propagator from the previous state vector to the current state vector and ω_{k-1} describes the random noise of the system (ie multiple scattering and energy loss).

The state vector is not observed directly. The measurements taken can be described in terms of the state vector as:

$$\mathbf{m}_k = \mathbf{H}_k\mathbf{x}_k + \epsilon_k. \tag{3.3}$$

Here $\mathbf{H}_k$ describes the relationship between the state vector and the measured quantity and ϵ_k describes measurement noise. The Kalman filter proceeds by performing three distinct operations:

- **Prediction** - Estimation of the state vector at a future measurement point.
- **Filtering** - Estimation of the state vector at the current measurement point based on previous measurements.
- **Smoothing** - Re-evaluation of the state vector at a previous measurement point using information from the current measurement.

Though the MWPCs represent a relatively simple case of a track fit it is necessary for the reconstruction to use the Kalman package for the fit so that the tracks can be used for track matching to study the performance of other detectors, and in order that the vertex fit can be performed by the Kalman filter.

The Kalman filter is provided with the positions of each MWPC and their sizes in an Algorithm called SetUpKalmanAlg which is required to be run before the Kalman filter is used. It is also here that it is provided with the radiation length of the MWPCs. The Kalman manager can then be accessed via this algorithm within the MWPC track object to create new Kalman trajectories and pass the relevant information from the MWPC points.

3.3 MWPC Simulation

In order to test the efficiency and accuracy of the reconstruction software a Monte Carlo simulation was used. This involved both a simulation of normal beam conditions mimicking those of the real situation and a simulation of the response of the detector. Both will be described below.

3.3.1 Beam Simulation

In order to simulate a beam that reproduced well the experimental reality beam parameters were taken from experimental data. The MWPC reconstruction software was run over different momentum settings of the data and the reconstructed beam parameters written to file for each event. These values could then be read in by the standard simulation package and used to simulate a beam with the same distribution of track inclinations and positions as the real data.

Since the MWPCs only read out the position of the closest wire the reconstructed position and momentum of tracks are biased by the positions of wires as can be seen in Figure 3.3 which shows the reconstructed track positions at the target. For this reason it was necessary to apply additional smearing to the beam parameters in the simulation in order to get a reasonable distribution of truth positions.

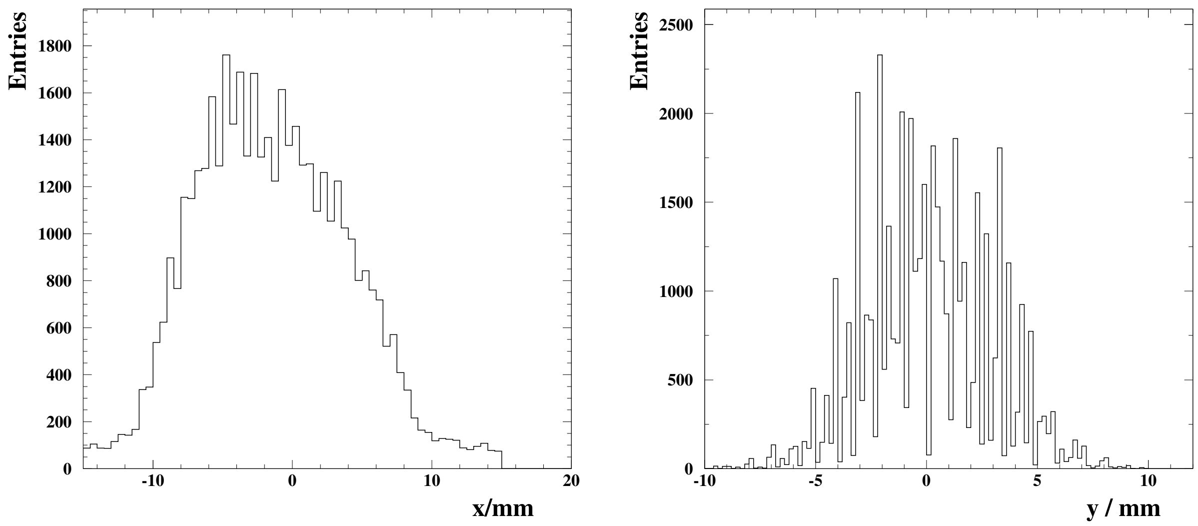

Figure 3.3: Distribution showing measured beam position at the target for a typical 15 GeV/c run.

3.3.2 The MWPC DetResponse

The simulation of each detector proceeds in two stages. First, hits are created in a given detector. This involves storing information about a passing charged particle which can cause a hit in that detector. These hits are then digitised. This involves the conversion of Monte Carlo information into a hit in that detector which can then be used in the reconstruction framework.

For the case of the MWPCs this process is quite simple. Since there is only yes/no readout all that is required for the first part of the simulation is to check each time a charged particle passes through the sensitive gas volume whether the particle has lost any energy through ionisation, and if so through which segmented gas volume the particle has passed, and to create the hit on this wire. In the digitisation the step of applying an efficiency to each wire plane is added. The calculation of these efficiency values are described below

Calculation of Efficiency

The efficiency calculation is done using the data. The efficiency of a given chamber is calculated by reconstructing particles using the other three chambers. If a track is successfully reconstructed then a hit in the two planes of the chamber not included is sought. The efficiency is then clearly the ratio between the number of tracks for which a corresponding hit was found in the plane and the total number of reconstructed tracks. The efficiencies for some runs at different energies, and taken during different periods of data taking can be seen in Figure 3.4. As expected no correlation with beam energy is observed.

3.4 Performance of Reconstruction Software

In order to determine the efficiency and accuracy of the MWPC reconstruction software the simulation described above was used in order to study the track position at the target with respect to Monte Carlo truth and to look at the efficiency of the tracking.

3.4.1 Accuracy

The accuracy of the reconstruction software was studied by comparing the reconstructed position with the Monte Carlo truth position at the target. Results can be seen in Figure 3.5. Good agreement is found with errors calculated using the formula [67]:

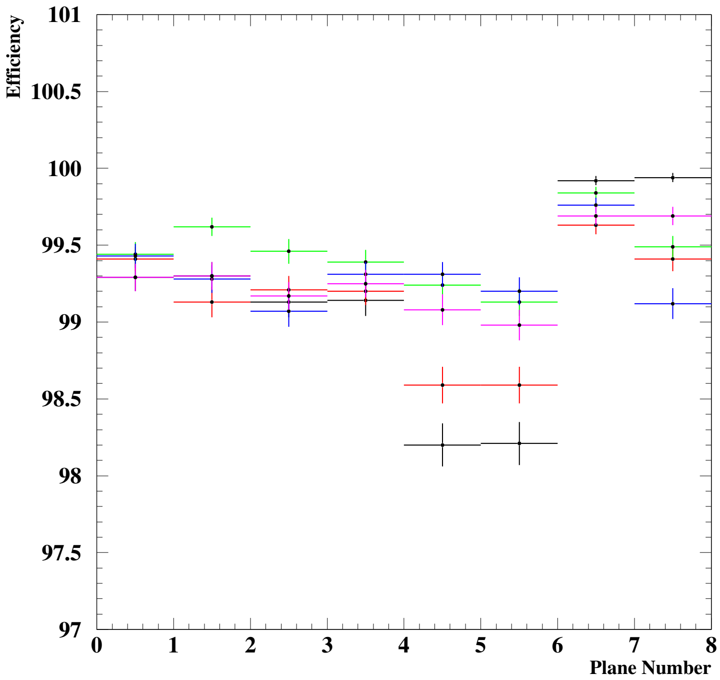

Figure 3.4: Plot of efficiency of each plane for 5 runs: 3 GeV/c (black), 5 GeV/c (red), 8 GeV/c (green), 12 GeV/c (blue) and 15 GeV/c (magenta).

$$\sigma_c^2 = \frac{\overline{\sigma^2}\ \overline{z^2}}{N(\overline{z^2} - \overline{z}^2)} \tag{3.4}$$

,where:

$$\overline{z} = \frac{\sum z_i/\sigma_i^2}{\sum 1/\sigma_i^2} \tag{3.5}$$

and

$$\overline{\sigma^2} = \frac{N}{\sum 1/\sigma_i^2} \tag{3.6}$$

which yields an error of 0.45 mm for a four chamber fit or a fit in which the three small chambers are used. Since the z position of the target is used the error on the intercept provides the total error on position. It can be seen that the errors on the position at the target are not gaussian. This is due to the non gaussian errors on the positions at each of the four chambers. It can also be seen that positions at the target show discretisation. The reason for this can be seen clearly in Figure 3.6, where it can be seen that a particular truth value will be reconstructed at defined positions which depend on the track angle. This is due to the fact that for the MWPCs only certain measurement positions are possible at each measurement plane. This leads to a discrete behaviour in the reconstructed position at the target. It can be also seen that due to this discrete behaviour the χ^2 value is not giving us an indication of the accuracy of the track (see Figure 3.7).

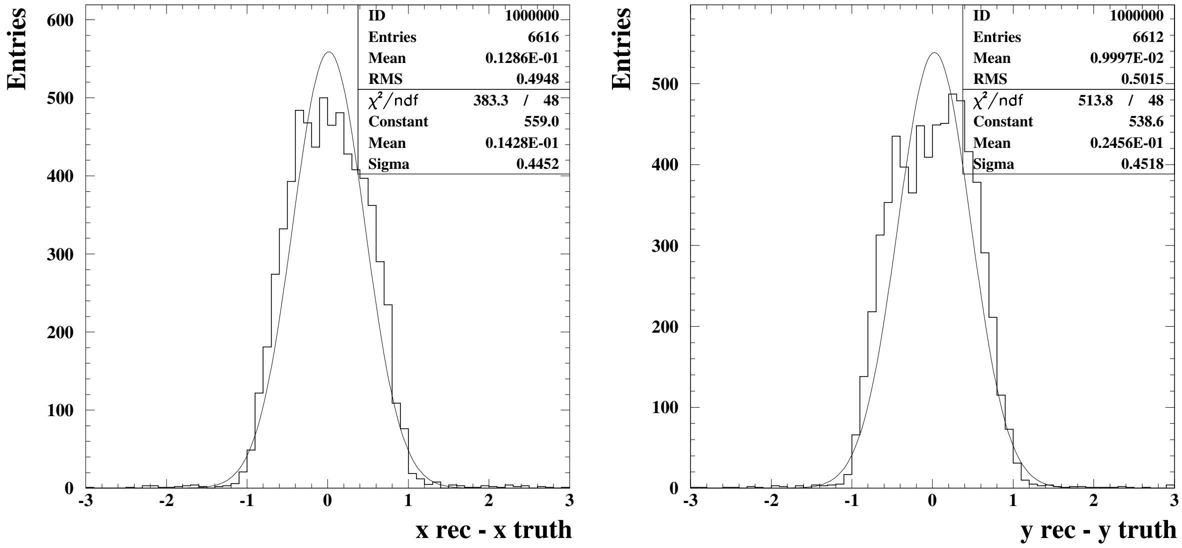

Figure 3.5: Reconstructed position–Monte Carlo truth position in the x direction (left) and y direction (right)

3.4.2 Efficiency

The efficiency of the reconstruction software was also studied using the Monte Carlo software. The values for the efficiency of each plane calculated from the data were fed into the MWPC simulation software and the results were examined. The efficiency was calculated by taking the ratio of the number of reconstructed tracks divided by the number of particles which passed through all eight sensitive gas volumes. Results can be seen in Table 3.1

It is found that when a point from all four chambers is required in the fit the efficiency directly reflects the summed efficiency of the eight planes. If this requirement is relaxed then an efficiency of 99.9 % can be achieved.

3.5 Summary

A chain of algorithms to reconstruct the position of beam particle at the target has been written. A study shows that the efficiency of track reconstruction is limited

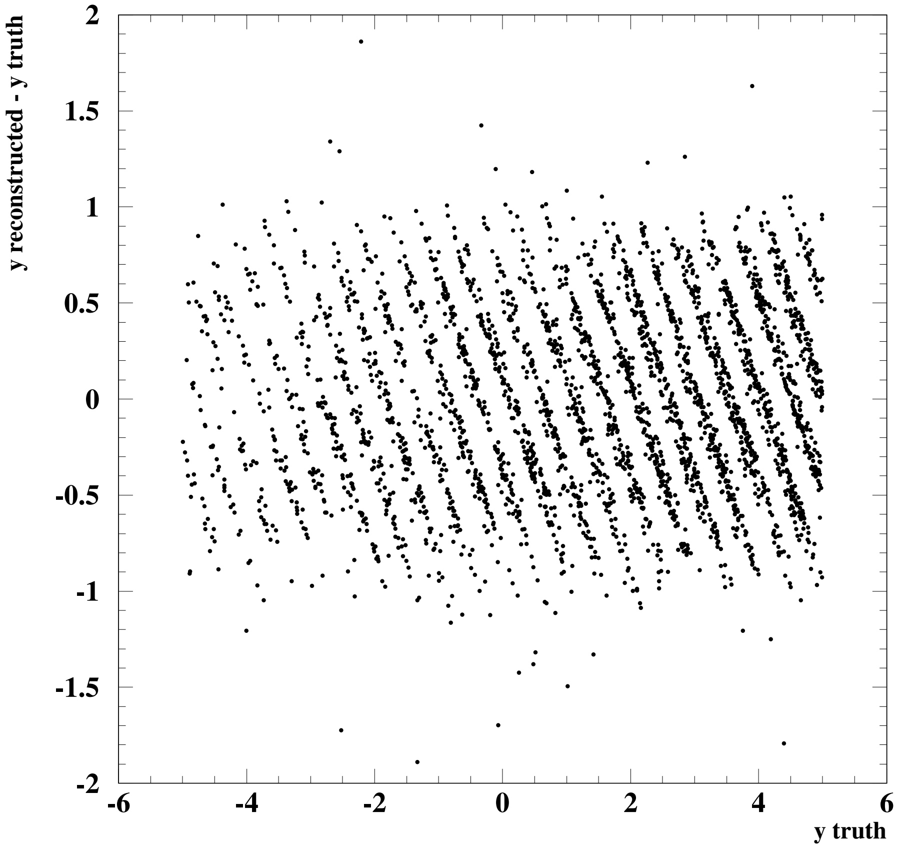

Figure 3.6: Error on reconstructed position against truth position in the y direction.

Number of planes required for fit	Efficiency of reconstruction
8	95.6 %
7	98.2 %
6	99.9 %

Table 3.1: Efficiency of beam particle reconstruction for different requirements on the number of planes.

only by the efficiency of the detector, and if only three points of four are required the efficiency of the reconstruction is found to be 99.9%. The accuracy found using the simulation shows good agreement with calculation and gives an error on position at the target of 0.45 mm.

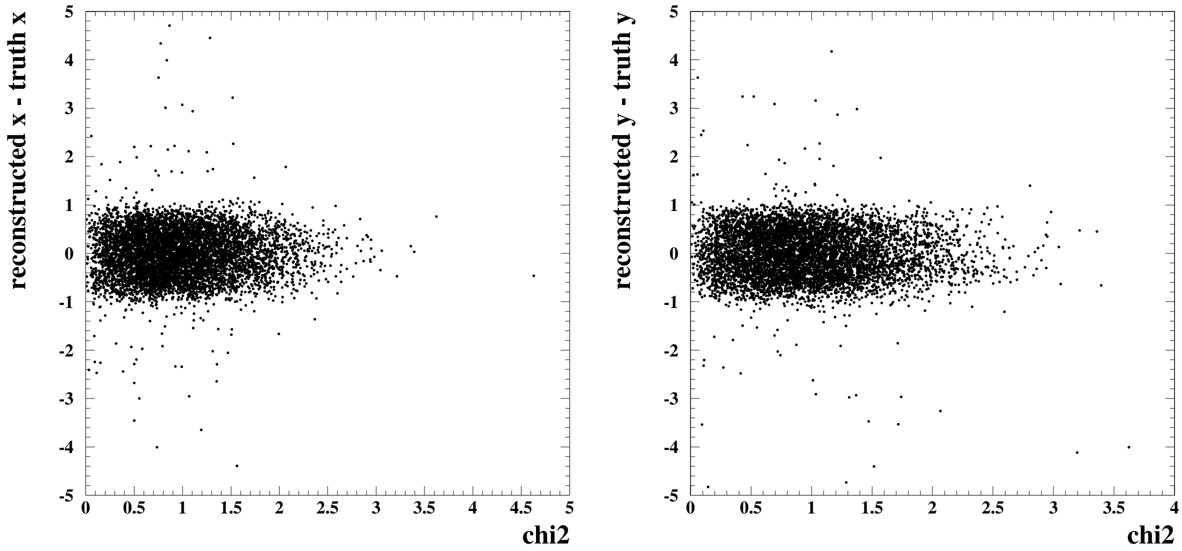

Figure 3.7: Error on position against χ^2 per degree of freedom for x direction (left) and y direction (right)

Chapter 4

TPC Simulation

A detailed simulation of the response of the TPC is essential in order to fully understand the detector. A simulation of the 'ideal' detector can be compared to the data - this enables differences between the Monte Carlo and data to be found and understood. Unwanted effects such as cross talk and field distortions can be modelled in the Monte Carlo and their effects on performance understood. Once all such effects have been understood and implemented in the Monte Carlo it can then be used to study the performance and acceptance of the detector.

This chapter describes the simulation of the response of the HARP TPC, which aims to reproduce the design specifications. The simulation describes all processes which occur after a charged particle passes through the gas volume specifically:

- Creation and propagation of drift charges
- Drift charge avalanche at the anode wires
- Response of pads to charge on wires
- Response of electronics and amplification of signal
- Digitisation of the signal
- Packing of the data

The first section gives an overview of the simulation software. Each step is then described in detail. For each step a description of the underlying physics and electronics is given along with a description of relevant models. The code used to implement these models is explained and reference plots demonstrating the output are given.

4.1 Simulation Software

The simulation of the TPC response consists of a series of Algorithms which act on the Data Objects into which the information is stored. (For a description of the role of Algorithms and Data Objects see Appendix A). The HARP simulation software is written using the Geant4 toolkit [44]. The TPC simulation interfaces to this. A schematic picture of the software is shown in Figure 4.1. Objects containing information about each point in the simulation are shown in the middle (e.g. drift charges and pads) and the algorithms which process these objects are shown down the left and right hand side. It can be seen that the simulation models every step from the energy loss of charged particles provided by Geant4 to the creation of the RawPERecord into which the data is packed in analogy with the real data.

4.2 Creation and Propagation of Drift Charges

4.2.1 Creation of Drift Charges

Energy Loss

A fast charged particle traversing a gaseous medium loses its energy dominantly through incoherent Coulomb scattering. The average differential energy loss from such processes was expressed by Bethe and Bloch as [69]:

$$\frac{dE}{dx} = D\frac{Z}{A}\rho z^2 \frac{1}{\beta^2}\left(\log\left(\frac{2m_e c^2\gamma^2\beta^2}{I\left(1+\gamma m_e/M\right)}\right) - \beta^2 - \frac{\delta}{2} - \frac{C}{Z}\right), \tag{4.1}$$

with

$$D = 4\pi r_e^2 m_e c^2 N_A, \tag{4.2}$$

where Z, A and ρ are the atomic number, weight and mass density of the medium and I is the average ionisation potential. β is the projectile velocity (in units of the velocity of light c) and $\gamma = \sqrt{\frac{1}{1-\beta^2}}$. m_e is the rest mass of the electron, r_e the classical electron radius and N_A Avogadro's number. δ is the density correction which is a function of β and the dielectric constant of the medium and corrects for the screening of the passing charge due to polarisation of the material. C is the shell correction which corrects for screening of inner atomic electrons.

The characteristic shape of this formula is shown in Figure 4.2. At low energies a fast decrease due to the $\frac{1}{\beta^2}$ term is observed which gives a minimum around $\beta \approx 0.97$, known as the minimum ionising region. This is followed by a slow increase as $\beta \to 1$ due to the logarithmic term known as the region of relativistic rise. Since the

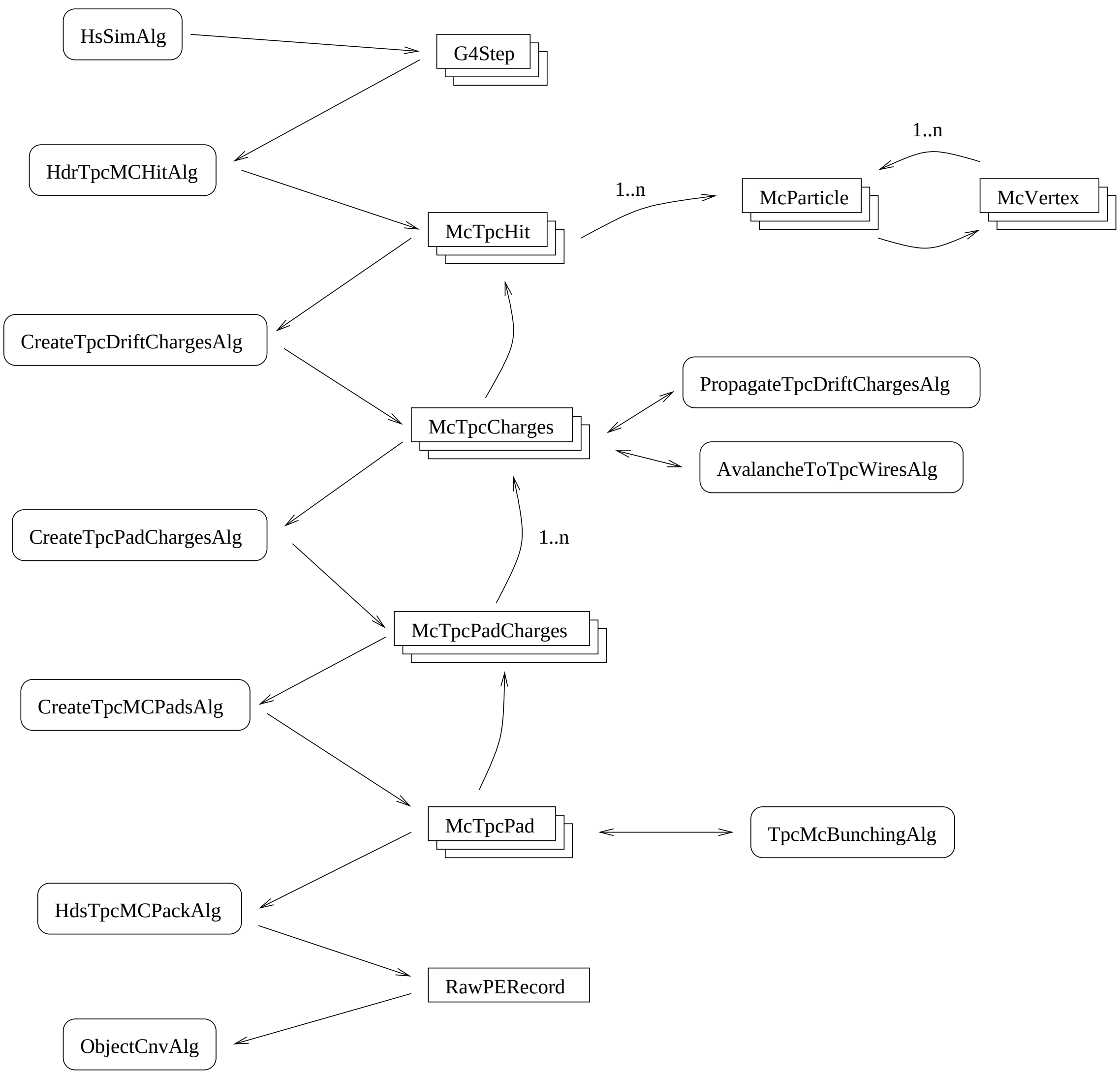

Figure 4.1: Schematic diagram to show the classes of the Simulation software. Square boxes indicate Data Objects and round edged boxes indicate Algorithms. [68]

value of $\frac{dE}{dx}$ depends only on the velocity and not on the mass, when used in parallel with a momentum measurement it provides a means of particle identification.

Distribution of Energy Loss

Though the Bethe Bloch formula gives the mean energy lost by a charged particle of a given velocity in the medium, in a thin material large fluctuations around this mean are expected. The energy is lost via a small number of discrete interactions giving a distribution which is not gaussian since each collision has a small probability to transfer comparatively large amounts of energy. The distribution has the characteristic shape for energy loss known as the Landau distribution. This can be

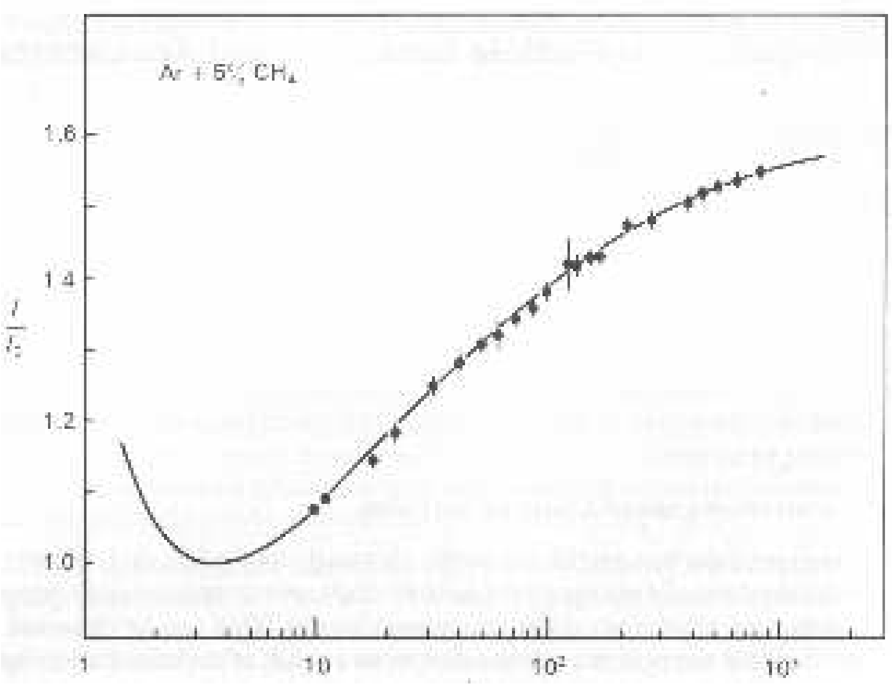

Figure 4.2: Mean Ionisation energy loss of charged particles in argon-methane mixture. [70]

expressed as [71]:

$$f(\lambda) = 1/\sqrt{(2\pi)}e^{-\frac{1}{2}(\lambda+e^{-\lambda})}, \tag{4.3}$$

where λ represents the normalised deviation from the most probable energy $(\Delta E)_{mp}$,

$$\lambda = \frac{\Delta E - (\Delta E)_{mp}}{\xi} \tag{4.4}$$

with ΔE representing the actual energy loss and ξ a constant which depends on the thickness of the material.

Relation between Energy Loss and Electrons Produced

Ionisation of the medium occurs both by primary and secondary ionisation. Primary ionisation occurs via close collisions between the charged particle and the gas. Secondary ionisation can occur both as a result of produced electrons which have sufficient energy to cause ionisation and also through more distant collisions with smaller energy where the charged particle causes intermediate excited states which can produce electrons on decay. The average number of electrons produced by a known energy loss can be found from the formula [71]:

$$n_e = \frac{\Delta E}{W}, \tag{4.5}$$

where n_e is the number of electrons produced, ΔE the energy loss and W the effective average energy to produce one electron ion pair, taking into account both primary and secondary ionisation.

Implementation in the Monte Carlo

It can be seen from Figure 4.1 that information from the Geant4 simulation is the first step in the TPC simulation. The G4Step provides information about each step taken by a particle in the gas volume of the TPC. This includes the position and momentum of the particle and more importantly the energy loss over the step. This information is passed to a McTpcHit, so all calculations of energy loss over a step and fluctuations in the energy loss are performed by Geant4. This information is then used by the TPC simulation via the McTpcHit in order to simulate the response of the detector.

Drift electrons are created from the McTpcHits in CreateTpcDriftChargesAlg. The number of electrons to be created is calculated using Equation 4.5 taking the value of W as 26.0 eV for the specific gas mixture of the HARP TPC [71]. For each electron a McTpcCharges object is created. A position for each electron is selected as a random position along the step [1]. Figure 4.3 shows the number of electrons created per 1 cm step for 10 GeV/c pions. The distribution is clearly Landau, and the mean and peak values show reasonable agreement with the plot on the right. The right plot is produced by a simulation done with Heed [72] which simulates primary and secondary ionisation processes in the specific gas mixture of the HARP TPC [73].

4.2.2 Propagation of Drift Charges

Drift Velocity

Once produced the electrons quickly lose energy and assume the average thermal energy of the medium. In the presence of an electric field E they assume a net motion in the direction of the electric field known as the drift velocity given by [74]:

$$u = \frac{eE}{m}\left\langle \frac{l}{v} \right\rangle = \frac{eE}{m}\tau, \tag{4.6}$$

[1] Clustering of electrons along the step due to ionisation processes is not yet taken into account in the Simulation

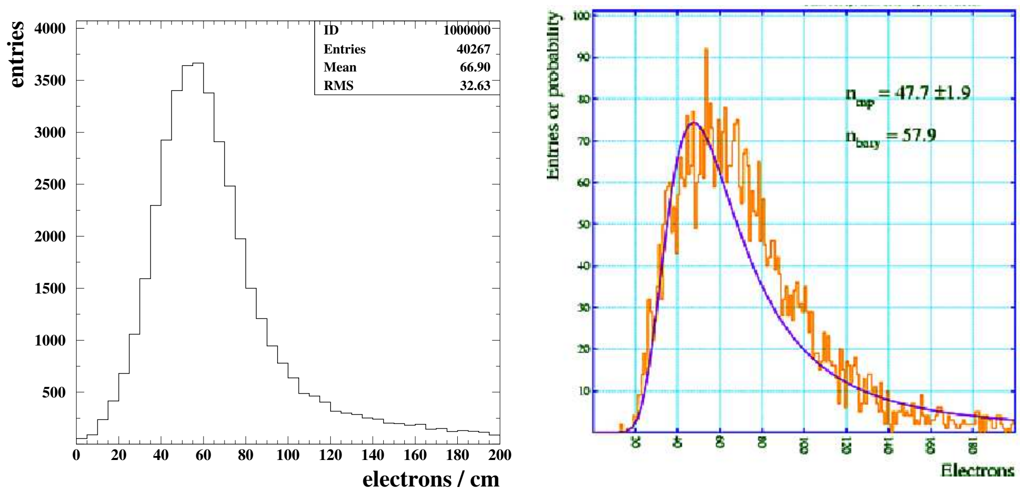

Figure 4.3: Number of electrons produced per 1cm step in Simulation (left) and results from a detailed simulation of the gas properties (right [73])

where e is the charge of an electron, E is the electric field of the medium, m is the mass of the electron, v is the velocity of the electron and l is its mean free path. τ describes the average time between collisions.

Diffusion

During their drift path the electrons undergo multiple collisions with gas molecules. This causes diffusion which results in a gaussian distribution of their position[69]:

$$\frac{dN}{N} = \frac{1}{\sqrt{4\pi Dt}} e^{-\frac{x^2}{2Dt}} dx. \tag{4.7}$$

$\frac{dN}{N}$ is the fraction of electrons in a bin of width dx at a distance x after a time t. D represents the diffusion coefficient which depends on the properties of the gas and the electric field. So after a time t an electron cloud will have undergone a gaussian diffusion with standard deviation:

$$\sigma_x = \sqrt{2Dt}. \tag{4.8}$$

In the absence of magnetic fields this diffusion will be the same in all directions but in the presence of a magnetic field the trajectories of the electrons in the plane perpendicular to the field are altered. In the case where the electric and magnetic field are parallel the projection of the particle trajectory in the plane perpendicular to the magnetic field become circular. This causes a decrease of the mean free path in this plane, and hence a decrease in the diffusion. In the plane parallel to the magnetic field direction the diffusion is unchanged. The decrease in diffusion occurs according to the equation [74]:

$$\frac{D(B)}{D} = \frac{1}{1+\omega^2\tau_B^2}, \tag{4.9}$$

where

$$\omega = \frac{eB}{m} \tag{4.10}$$

and τ_B is a phenominological mean collision time which is in general a function of both E and B.

Implementation in the Monte Carlo

The drift coefficients for the HARP TPC have been found using a Garfield simulation which simulates the properties of the gas and the electric and magnetic field [73, 75]. The transverse diffusion σ_{trans} is 0.203 mm for 1 cm drift and the longitudinal diffusion σ_{long} is 0.378 mm for 1 cm of drift which corresponding to a diffusion in time of 7.3 ns for 1 cm of drift.

The calculation of the electrons' position at the cathode plane is done in PropagateTpcDriftChargesAlg. The positions in x and y have their position shifted according to a random gaussian number whose sigma is defined as:

$$\sigma_{x/y} = \sigma_{trans}\sqrt{l_{drift}}, \tag{4.11}$$

where l_{drift} is the drift length. The time is shifted according to a random gaussian number from a distribution whose mean is the time taken to drift to the pad plane and whose sigma is defined as:

$$\sigma_t = \sigma_{long}\sqrt{l_{drift}}/v_{drift}. \tag{4.12}$$

Figure 4.4 shows the transverse and longitudinal diffusion for different drift distances. The amount of diffusion increases with distance as expected. The lower plots show the diffusion divided by the square root of the drift distance and demonstrate that this is the diffusion for 1 cm as expected.

4.3 Simulation of Avalanche

After passing through the drift volume of the detector, the electrons arrive at the wire chamber. The anode wires in the wire chamber are at high voltage, causing the drift electrons to accelerate towards them. Once they gain enough energy between

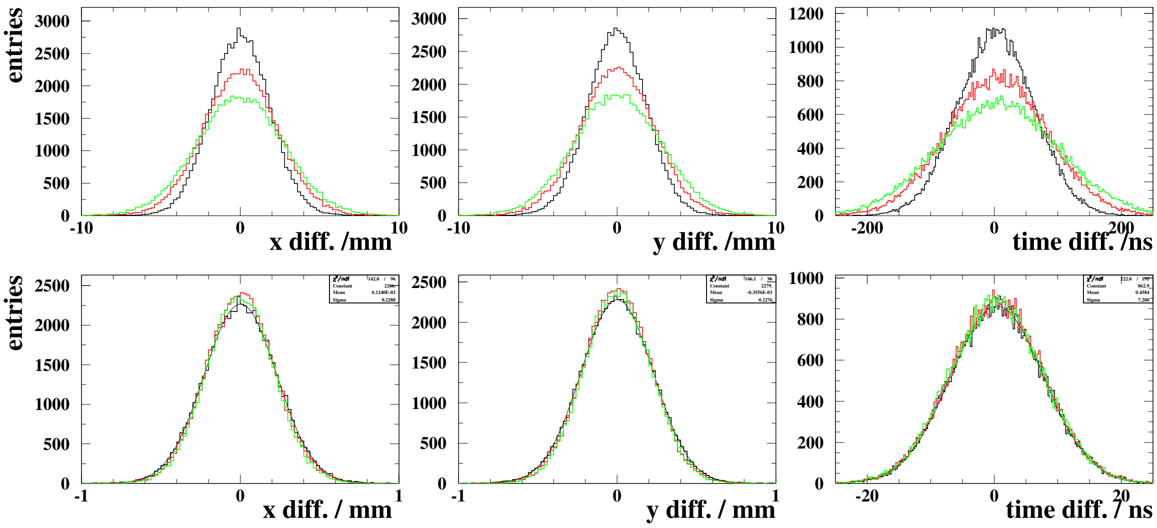

Figure 4.4: Diffusion in x (left), y(centre) and time(right), for a drift distance of 50cm (black) 100cm (red) and 150cm (green). Top plots show total diffusion over the drift distance. Bottom plots show the total diffusion, divided by the square root of the drift distance for x and y and divided by the square root of drift distance multiplied by drift velocity for time.

collisions to cause ionisation they create further electrons and an avalanche begins. Provided that the effects of space charge (which occurs as a result of the positive ions) and induced effects remain negligible with respect to the electric field from the wire, then the signal is proportional to the initial charge. Due to the fact that they are much lighter the electrons reach the sense wire extremely quickly leaving behind a cloud of positive ions as a result of the avalanche.

Gain Factor

The multiplication of electrons in the avalanche is described by the first Townsend coefficient α. The increase in the number of electron dN as a function of the path length ds can be expressed as [76]:

$$dN = N\alpha ds. \tag{4.13}$$

The value of α depends on both the properties of the gas and the electric field. No fundamental expression for the value of α exists so it must be found either from direct measurement or using detailed simulations.

The amplification factor, which represents the factor of increase in the number of electrons, can be found by integrating the above expression between the distance at which the field is just sufficient to start the avalanche(s_{min}) and the wire radius (a). This gives:

$$\frac{N}{N_0} = \exp \int_{s_{min}}^{a} \alpha(s) ds = \exp \int_{E_{min}}^{E(a)} \frac{\alpha(E)}{dE/ds} dE, \tag{4.14}$$

where N is the final number of electrons, N_0 is the initial number of electrons and dE/ds is the field gradient.

Distribution of Gain Factors

While the average number of electrons resulting from a single initial electron can be expressed by Equation 4.14, the process of ionisation is clearly statistical and so fluctuations around this value are expected for individual electrons. If we make the assumption that the probability of ionisation is proportional to the field strength and is independent of the previous history of the electron then we find that the probability distribution for a single electron can be described by the distribution for a Yule Furry process [77]:

$$P(n) = \frac{1}{\overline{n}} \left(1 - \frac{1}{\overline{n}}\right)^{n-1}. \tag{4.15}$$

In the limit that $\overline{n}$ is large this approximates to:

$$P(n) = \frac{1}{\overline{n}} e^{(-n/\overline{n})}. \tag{4.16}$$

$E \times B$ Effect

As the electrons approach the wire they also undergo a rotation due to the fact that inside the wire chamber the magnetic and electric field lines are no longer parallel causing a so-called $E \times B$ force. The electrons have to move transverse to the magnetic field meaning that the electrons' drift paths are distorted and they rotate through an effective angle ψ [76].

Implementation in the Monte Carlo

The electron's position at the wire is calculated in AvalancheToWiresAlg. The closest wire to the electron is calculated using information about the wire geometry. The position at this wire is then calculated taking into account a tangent Lorentz angle caused by the $E \times B$ effect. The tangent Lorentz angle is taken to be 32° since this was the value found for the ALEPH TPC which had a similar design to the

HARP TPC. Once the position at the wire has been calculated in this way a check is done that the electron does not fall in the dead region of the spokes[2]. Figure 4.5 shows the positions of the electrons at the wires. Individual wires can be clearly seen and the dead regions of the spokes are also clearly visible.

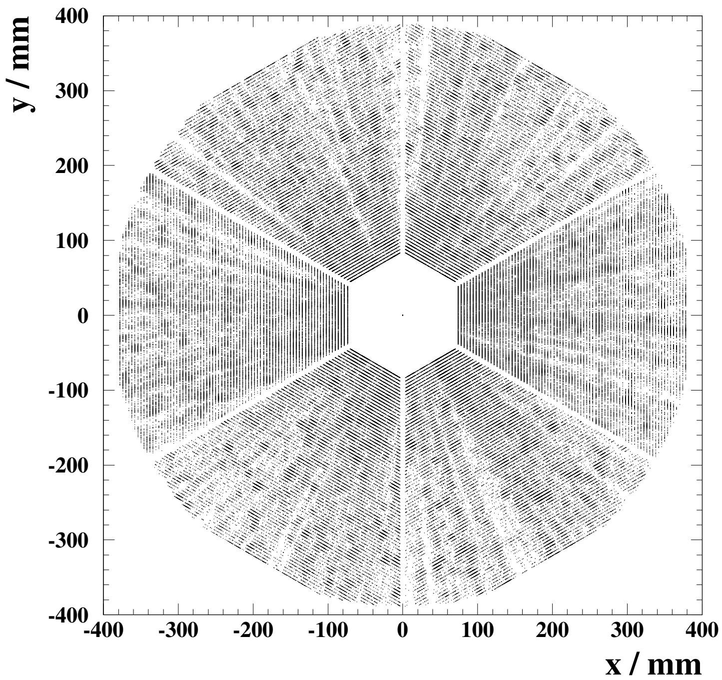

Figure 4.5: Position of the drift electrons at the wire plane from the MC simulation.

A gain factor is calculated for each electron. This is taken as an exponential with a mean value of 166000 with a maximum value of 830000. Figure 4.6 shows the gain distribution. These values are taken from a detailed simulation of the HARP TPC using Garfield which took into account the gas properties and electrostatic design [73].

4.4 Simulation of Pad Response

The Pad Response Function

The amount of charge seen by a pad from a charge cloud depends not only on the distance from the pad but also on the pad geometry and the distance between the

[2] The wires of the HARP TPC are formed by winding a single wire around six spokes. The region of the spokes is dead.

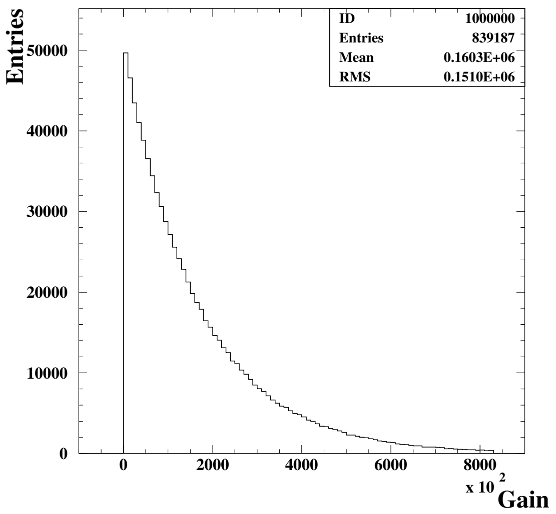

Figure 4.6: Distribution of gain factors of electrons.

wire plane and the pad plane. The response of the pad to incoming charge is found to follow the empirical relation [76]:

$$P = \int_{x-W/2}^{x+W/2} -\frac{\lambda}{2D}\frac{1}{\cosh(\pi x/D)}dx, \tag{4.17}$$

where λ is the charge density, D is the distance between the charge (ie the wire plane) and the cathode plane, x is the distance between the charge and the centre of the pad, and W is the width of the pad. Equation 4.17 can be integrated to give:

$$P = \left[\frac{-\lambda}{2D}\arctan\left(\exp\left(\pi\frac{x}{2D}\right)\right)\right]_{x-W/2}^{x+W/2}. \tag{4.18}$$

Implementation in the Monte Carlo

In CreateTpcMcPadChargesAlg the response of all pads within a radius 30 mm of each charge is calculated using Equation 4.18 and the distance of the charge from the pad centre. The pad response function is calculated both in the r and $r\phi$ directions and the results are multiplied. Figure 4.7 shows the pad response function coming from the simulation. Also shown is the measured pad response function for the TPCino (the prototype TPC). The resulting value for a given pad is then multiplied by the previously calculated gain factor, and added to a charge time series for that pad.

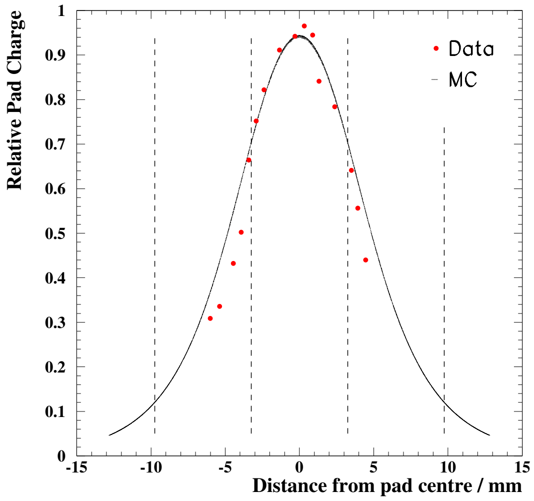

Figure 4.7: Measured Pad Response Function (red points, data taken from [73]) and Simulated Pad Response Function (black). Dashed lines indicate pad size.

4.5 Simulation of Electronics and Amplification

Transfer Function

The response of the HARP electronics to a fast input signal is found to be well approximated by a gamma function [73]:

$$\Gamma = \left(\frac{t}{\tau}\right)^2 \exp\left(-\frac{t}{\tau}\right), \tag{4.19}$$

where the value of τ is 70 ns. This is known as the transfer function. However the signal which leaves the amplifier is in fact the convolution of the input signal with this transfer function. The signal from a single electron while having a width of only a few ns, has a very long tail, and this causes a broadening of the signal width to give a value of τ of 95ns.

Collection and Drift Anisochrony

A broadening of the signal shape can also occur as a result of collection anisochrony. This refers to the difference in arrival times at the anode wires due to the different paths taken by the various drift electrons. However, for the HARP TPC, this gives only a minor contribution to the signal width. Broadening of the signal shape also occurs as a result of the track inclination and is called drift anisochrony. For inclined tracks, electrons from the same track which drift to the same pad will have different drift distances, and hence will arrive at the wire at different times. The effect of track inclination on signal shape, as found by a Garfield simulation can be seen in Figure 4.8 [73].

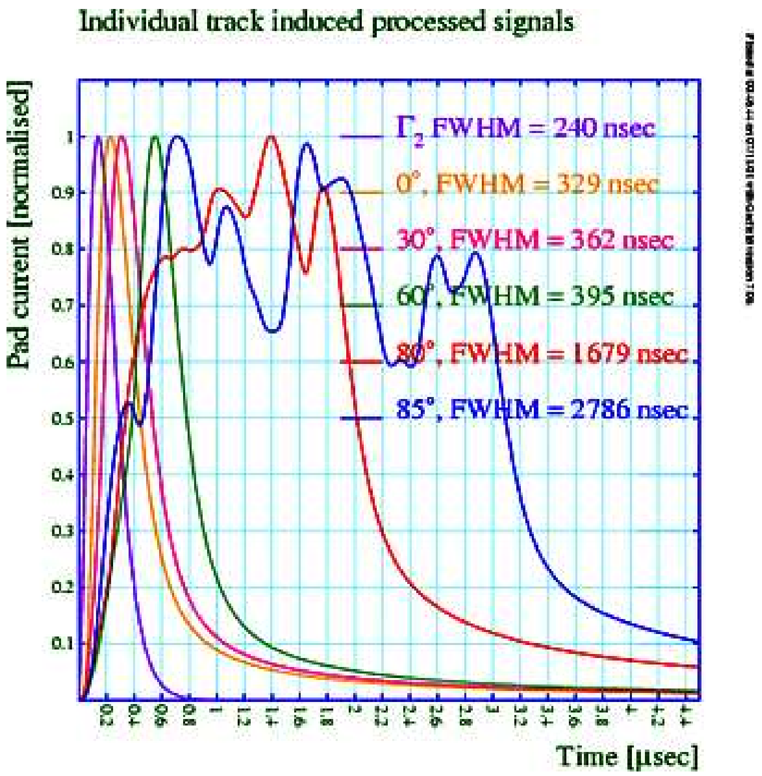

Figure 4.8: Effect of track angle on the signal shape [73].

Implementation in Monte Carlo

The creation of an ADC series on each pad is done in CreateTpcMCPadsAlg. A signal shape is created with the form of the gamma function. The signal shape is calculated bin by bin with a bin size of 100ns. Formula 4.19 is used to calculate the ADC value for each bin, where the time t is the arrival time of the first charge minus the time of the current bin and τ is 95 ns for tracks parallel to the pad plane. This value is weighted by the total amount of charge that has arrived at the pad at the time of this bin, by the current pad gain, by the amplifier gain and by a final factor to convert to ADC counts. Figure 4.9 shows a typical pad signal which has values in excellent agreement with the predictions from the detailed Garfield Simulation [73]

When the track is not parallel to the pad plane the time over which charge from drifting electrons arrives at the pad is stretched and this results in a stretching of the pad signal. In order to take this stretching into account the τ of the transfer function is altered according to the length of the charge bunch which arrives at the pad.

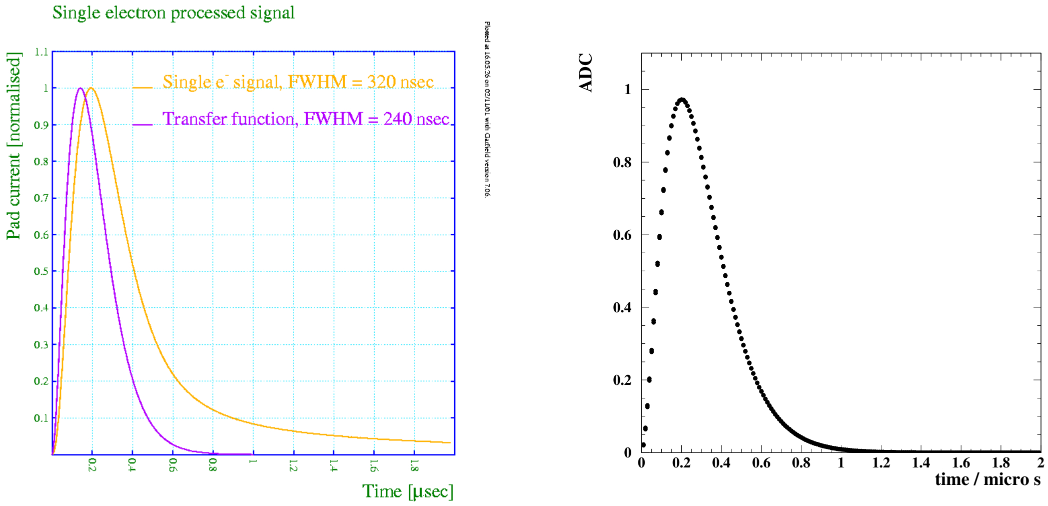

Figure 4.9: Predicted signal shape (left [73]) and signal shape from TPC simulation (right)

4.6 Simulation of Digitisation

The TPC readout is carried out by the ADC cards. The signal is sampled by a 10 MHz clock resulting in one sample every 100 ns. In order for a signal to be read out it must rise above a threshold of 10 ADC counts. All samples above this threshold are read out and in addition two pre and two post samples at the beginning and end of any signal are also read out.

In order to simulate the behaviour of the ADC cards the pad signals are 'bunched' by TpcMcBunchingAlg. This separates the ADC series into bunches where each bunch consists of a series of consecutive ADC values above threshold. Once this is done pre and post samples are added to each bunch. If the bunches overlap after the addition of pre and post samples then the bunches are merged.

4.7 Simulation of Packing

The data from each event is passed to the ObjectCnv as a block of data. This block of data consists of several different parts. First are several headers which contain information about the event, and which detector the data is from. This is followed by a data block containing the information from the detector for that event. For each signal on a TPC pad a series of 10 bit words are stored, one for each ADC value of the signal. This is followed by 1 word containing the time of the last ADC value, and then a word containing the total number of 10 bit words including the time value and that 10 bit word itself.

The packing of simulated data is done by HdsTpcMcPackingAlg. The purpose of this algorithm is to pack the Monte Carlo data in an identical way to the real data. Once this has been completed the Monte Carlo data can be read by the ObjectCnv in the same way as the real data. Figure 4.10 shows a typical signal as it looks after passing through the ObjectCnv.

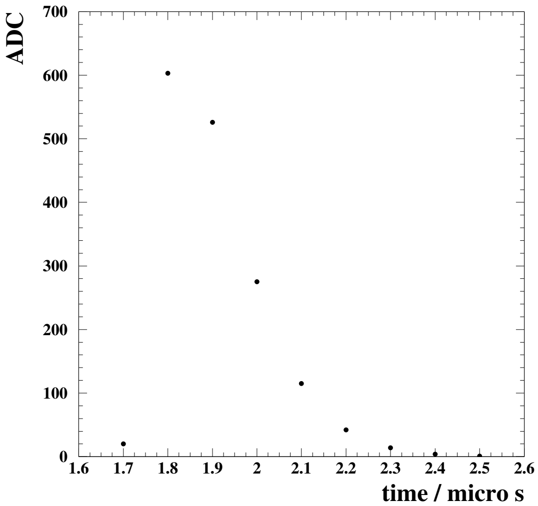

Figure 4.10: Typical signal shape returned by ObjectCnv. Hardware threshold is applied, along with pre and post samples. 100 ns sampling is also applied.

4.8 Summary

The prototype simulation of the TPC has been substantially modified and updated both to conform to the HARP software framework and to reproduce design specifications. All physics and electronics processes from drift electron creation to the packing of data are modelled in the simulation and plots to verify that the simulation performs as expected at all steps are produced. The simulation now acts as a useful tool to understand the detector. Any differences between the output of the Monte Carlo and data must be understood and added to the simulation. Once the detector is fully understood the simulation can be used to find the acceptance and resolution of the detector.

Chapter 5

The Cross Talk Effect And Its Simulation In The Monte Carlo

During HARP's 2002 data taking runs it was discovered that the TPC electronics suffered from a cross talk effect [78]. This meant that for certain pads in the TPC, when a signal was induced on that pad, signals were also observed on certain other pads, regardless of whether these pads had received any charge. This effect was caused by capacitive couplings between the input of one preamplifier and the output of another. The problem occurred due to the physical proximity inside the pad plane of the vias carrying signal before and after amplification. A cross section of the mother board can be seen in Figure 5.1. The places where capacitive coupling can occur are indicated with capacitors.

This chapter will begin with a description of the model which was found to accurately describe the cross talk effect. A special set of data taken to parameterise the effect will be described along with an overview of its finding. The implementation of this model into the Monte Carlo simulation using this data set will then be described, along with the procedure used to validate this implementation.

5.1 Cross Talk Model

As previously stated the cross talk effect is caused by a capacitive coupling between the output of one preamplifier and the input of another. A schematic diagram of the resulting circuit can be seen in Figure 5.2. In the following discussion the pad on which a signal was originally induced will be referred to as the parent pad, and its output signal the parent signal. Any pad on which a signal is induced as a result of capacitive coupling with the parent pad will be referred to as a daughter pad, its output signal will be referred to as the daughter signal. The response of a pad to a

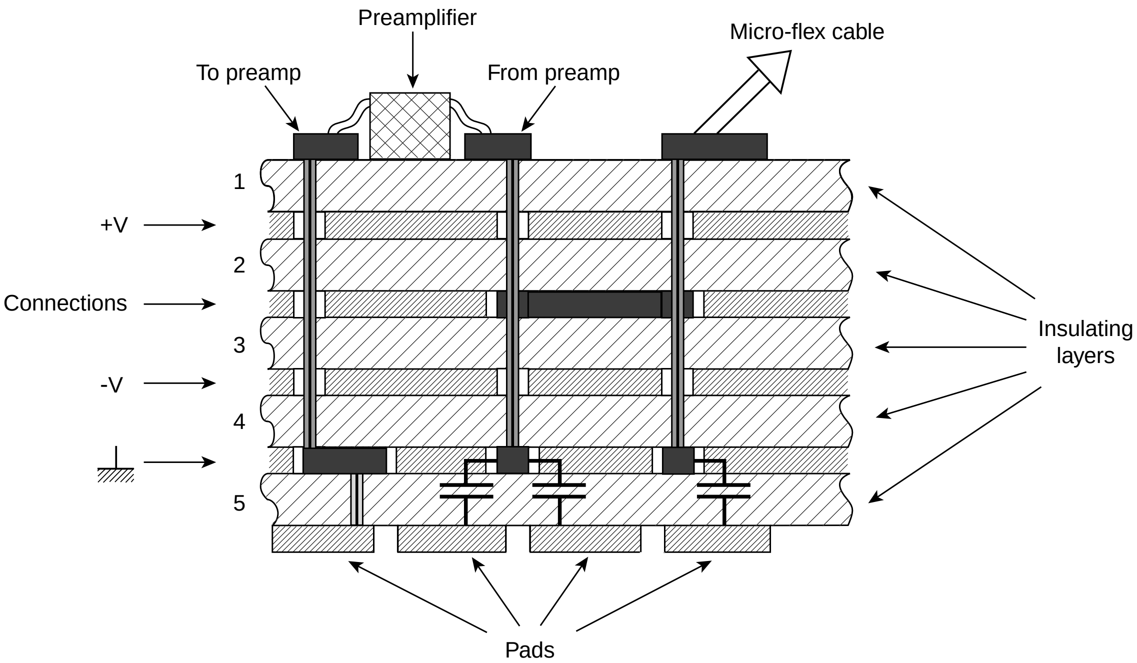

Figure 5.1: Cross section of the pad plane [79].

delta function pulse will be referred to as the pad's transfer function.

The expected output of a pad is given by the convolution of the input signal with the pad's transfer function. It can therefore be concluded that the daughter signal will be described by the following equation [79]:

$$F(\omega) = -i\omega g_P g_D C S_P(\omega) T_D(\omega), \tag{5.1}$$

where g_P and g_D are the gains of the preamplifiers of the parent and daughter pads, C is the capacitive coupling between the two pads, $S_P(\omega)$ is the signal from the parent pad and $T_D(\omega)$ is the transfer function of the daughter. This means that the resulting signal is the convolution of the signal from the mother with the transfer function of the daughter multiplied by a factor $i\omega C$. The effect is that of differentiating the signal and a typical example can be seen in Figure 5.3 [1].

5.1.1 Mapping of Cross Talk

It is clear that in order to fully describe the cross talk in the HARP TPC in addition to the above model a map of cross talk relations along with the capacitive couplings

[1] The small difference between the predicted and measured signal between -0.3 and -0.2 micro seconds is most likely an artifact of the computation, caused by the convolution of the signals being done over two short a time range. It has been observed that this can cause small disturbances in the ADC values predicted at the beginning and end of the signal.

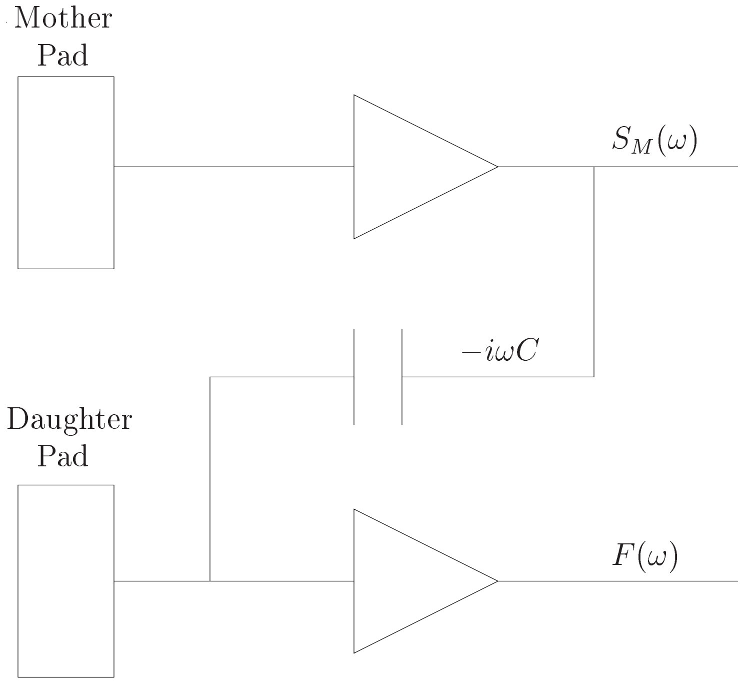

Figure 5.2: Schematic of the electronic circuit causing cross talk

between the related pads is required. In order to provide this a special set of data was taken at the end of HARP's 2002 data taking run [79]. Each pad in each sector was excited by means of a probe which was attached to a wave generator through a capacitor. The wave generator provided a step function resulting in a delta function being injected into each pad. Each pad was excited multiple times and the data recorded by the DAQ in the normal way. Since the delay between the start of the signal and the 100 ns clock is recorded the pulse shapes can be accurately reconstructed offline by means of the phase lock technique[2]. Since the DAQ only records the positive part of signals the negative part of cross talked signals is not available. For this reason some data was also recorded using an oscilloscope to confirm the existence of the negative swing.

Since all signals on all pads were recorded for each pad pulsed, it was possible to create a map of all cross talk relations, and a fit to the model was used to calculate the capacitive couplings for each relation (Figure 5.4). It was also possible to calculate the electronics gains of all pads (Figure 5.4). For the purposes of the Monte Carlo simulation only information from sector six was used, since initially the analysis was performed on this sector, and the work had not been repeated on the other five sectors at the time of writing. In this sector a total of 725 first order

[2]The phase lock technique refers to the addition of many sampled signals, using the information of the signal offset to get a smooth signal shape.

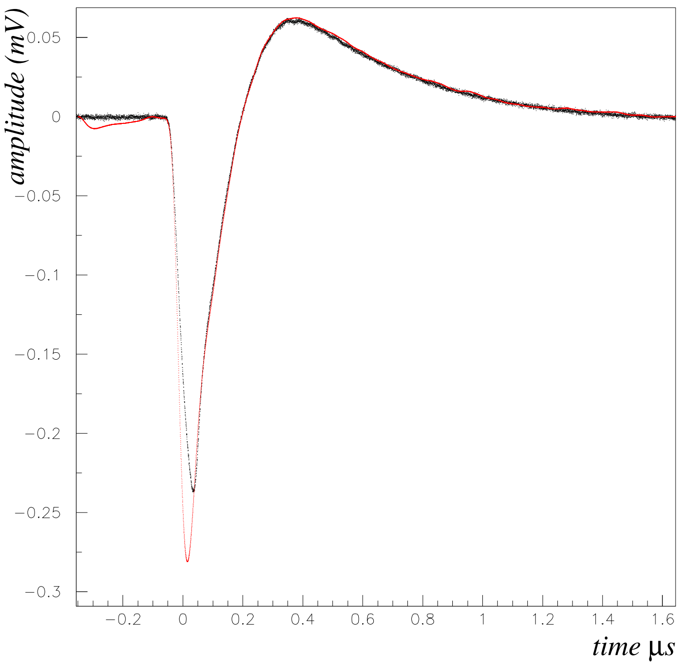

Figure 5.3: Typical first order signal as measured with an oscilloscope (black) and the signal predicted by Equation 5.1 (red) [79].

relations were observed. 159 pads were found to have no daughters and a further 325 were found to have no mothers. The positions of these pads can be seen in Figure 5.5. Daughter pads are almost always close to their parents, being either in the same row or only one row away and within a few pads in the $r\phi$ direction [80].

5.1.2 Self Talk

In addition to relations between pads many pads have internal relations causing them to talk to themselves (self-talk). The summation of several orders of cross talk causes the shape of the pads signal to change making the amplitude lower and causing a longer tail as can be seen in Figures 5.6 and 5.7. For pads with self talk there is no way to measure their 'true' transfer function, only the function which is the result of the self-talk. This has the effect that the gains measured for these pads are lower. The two distinct peaks in gain can be seen in Figure 5.4. Likewise for relations involving these pads measured capacitive couplings are higher. Again this can be observed in the plot of coupling seen in Figure 5.4. A large proportion of pads are found to be affected by self talk. The positions of these pads can be seen in Figure 5.8.

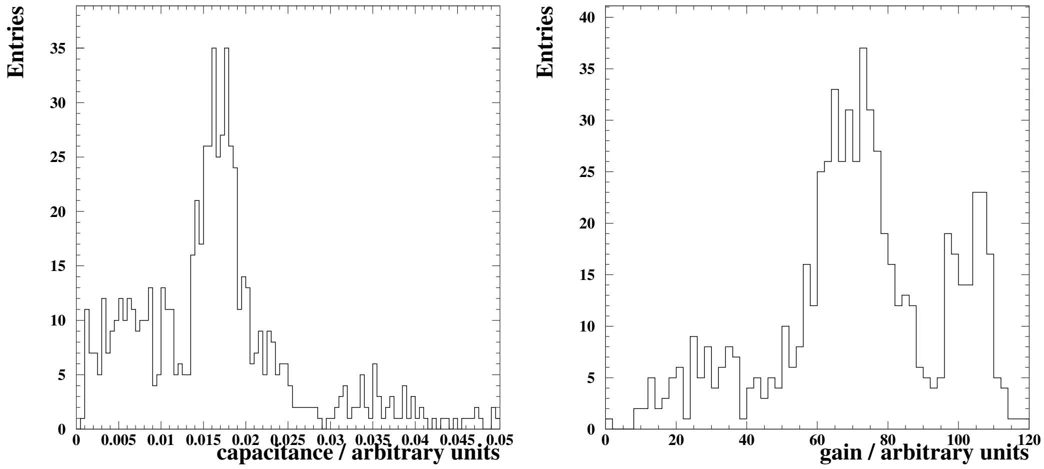

Figure 5.4: Distributions of capacitive couplings for cross talk relations in sector six (left) and Gains of pads in sector six (right).

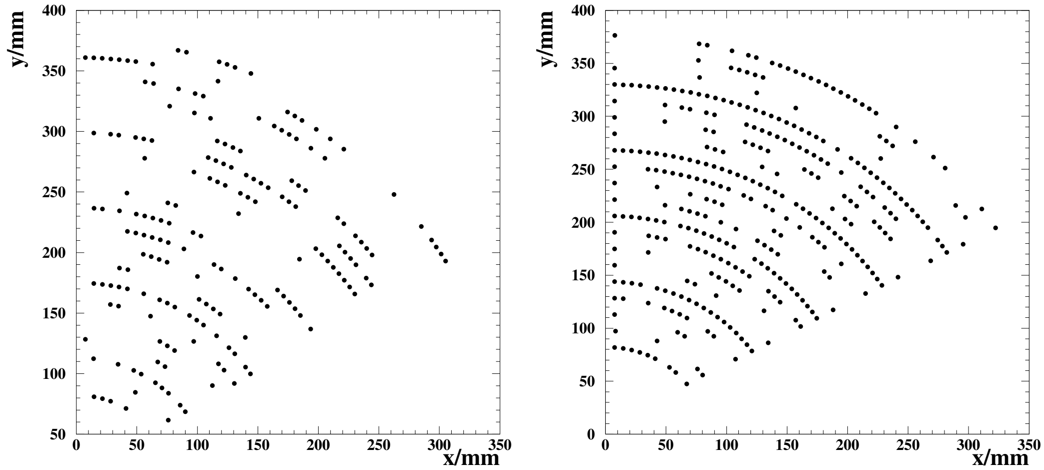

Figure 5.5: Positions of pads with no daughters (left) and no parents (right)

5.2 Implementation of Cross Talk Effect in Monte Carlo

The data obtained as a result of the pulser measurements described above were used to model the effects of cross talk and self talk in the Monte Carlo simulation of the TPC. A diagram of the classes and algorithms used in the implementation can be seen in Figure 5.9; these will be described in more detail below. The implementation falls into two categories

- changes to the way in which original signals are created in order that the effects

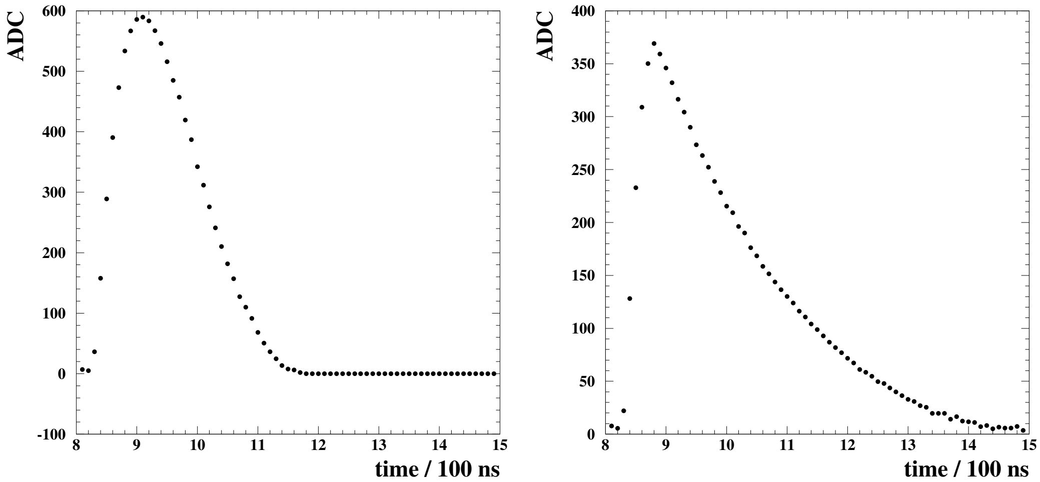

Figure 5.6: Typical signal shapes for a pad with no self talk (left) and a pad with self talk (right)

of self talk can be correctly reproduced

- calculation of cross talk signals which are induced on other pads by the initial signals

5.2.1 Implementation of Measured Transfer Functions

An option was provided in CreateTpcMCPadsAlg to use the transfer functions measured in the pulser runs instead of the parameterised transfer function described in the previous chapter. The ADC series of each transfer function for each pad, found using the data from pulser runs, is stored in a CrossTalkCalib and can be accessed when required via the CrossTalkCalibManager. In order to model the effects of drift anisochrony on the shape of the transfer function, the arrival times of the charges are used to calculate a charge distribution with the same binning as the measured transfer function. This distribution is then divided by the amount of charge injected into each pad during the pulser runs in order to provide the correct normalisation. A convolution between this charge distribution and the measured transfer function is then carried out by the CrossTalkCalculator using fourier transforms from the GNU Scientific Library [81].

5.2.2 Implementation of Cross Talk

The calculation of cross talked signals is done by AddTpcCrossTalkAlg. This algorithm simply takes the original signal and calculates resulting daughter signals up

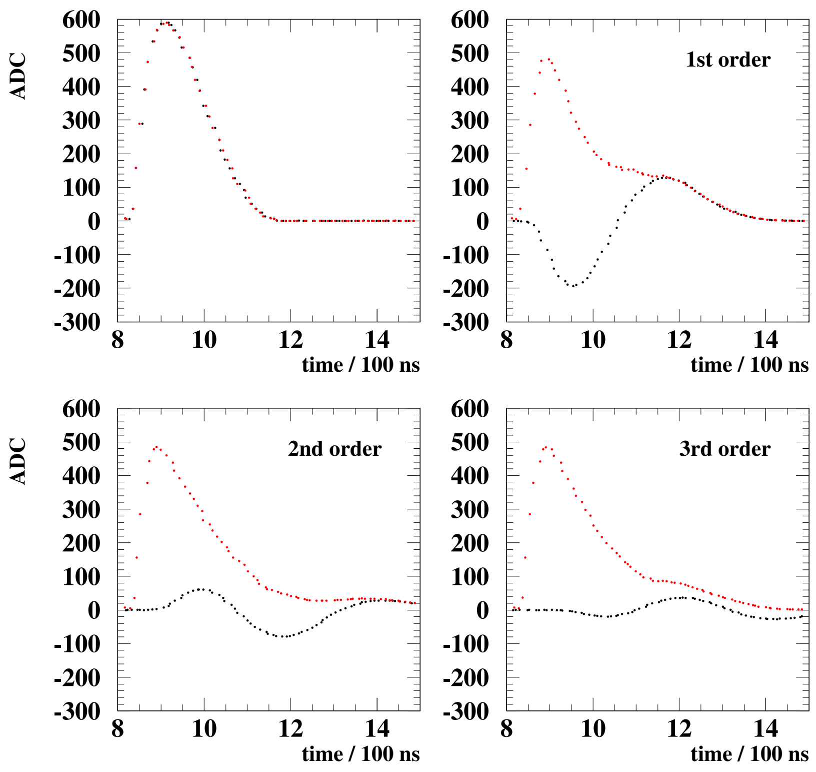

Figure 5.7: Demonstration of how several orders of cross talk lead to the self talk shape - cross talk signals are shown in red and the summation of orders in black

to the order required. The cross talk relations are read in during the initialise phase and a vector of Daughter objects is added to each CrossTalkCalib associated with a pad. The algorithm then merely iterates over the pads and passes each pad to the CrossTalkCalculator which performs the following steps:

- Find the daughters of the pad.
- Separate the signal from that pad into bunches if they exist. [3]
- Do the convolution of each bunch with the transfer function of the daughter pad.
- If there are multiple bunches then merge the results of these convolutions.
- Multiply by the capacitive coupling of the relation.

[3]Multiple bunches occur when ADCs which are not contiguous in time exist. For example if two tracks cross a pad then there will be two bunches.

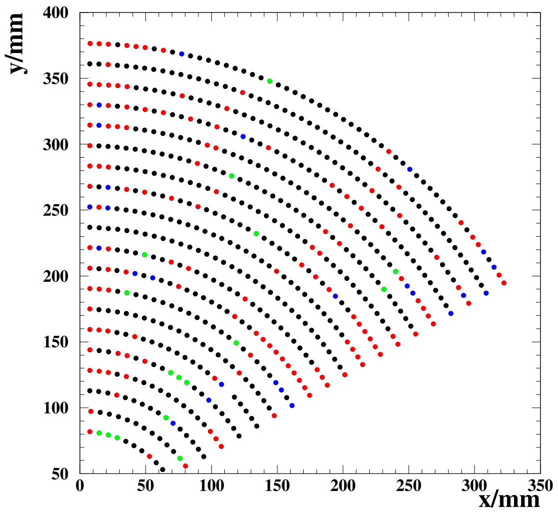

Figure 5.8: Positions of pads with no self talk(red), with self talk (black), ambiguous cases(blue) and dead pads(green)

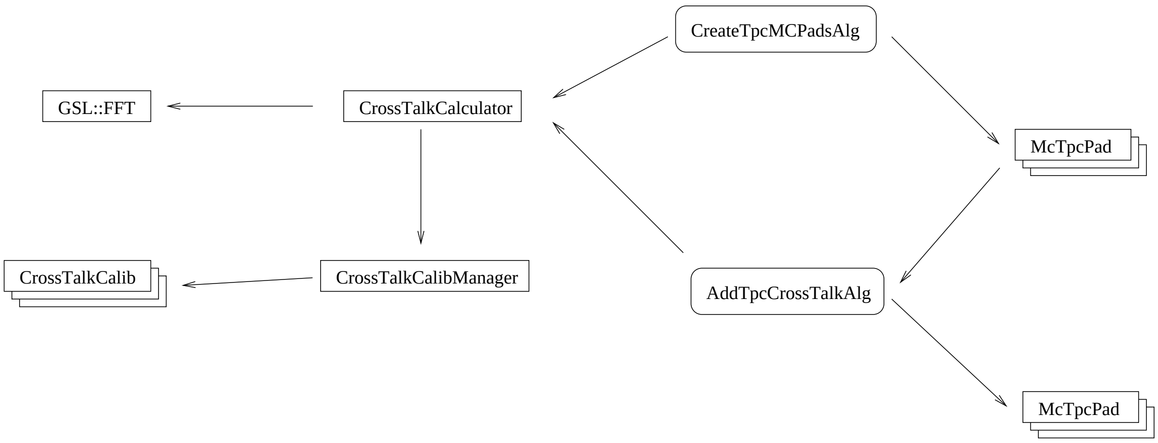

Figure 5.9: Diagram of inter-relation of objects and algorithms calculating cross talk signals.

- Check if a cross talked signal already exists on this pad. If it does then add the new signal to the existing one, if not create a new pad.

The result is a vector of pads which contain the first order cross talked signals. The process can be repeated to calculate further generations of cross talk as required. All generations are then added to the original signals, creating a vector of pads that results from cross talk which is committed to the transient store.

5.2.3 Validation

As a test of the use of measured transfer functions a charge of the size injected during the pulser data was placed in one charge bin, and the rest of the simulation run as normal. Correct implementation of the method requires that the results should be identical to the measured transfer functions used as input. This was found to be the case.

The implementation of cross talk in the Monte Carlo was validated by comparing the results of a Monte Carlo 'pulser' run (see the description above) with the results of the convolution of appropriate transfer functions. Agreement was found to be excellent. As a cross check of the model, results of a simulated pulser run were compared with data reconstructed using the phase lock technique. Some indicative results can be seen in Figure 5.10. It can be seen that first order results are reproduced with excellent accuracy. However for second order cross-talk the first peak is overestimated in the Monte Carlo. This happens because in the data the amplifier saturates. Since the pulser data was taken at high energies compared to those expected during normal runs, it is expected that the discrepancy will not be there for normal data taking conditions [82].

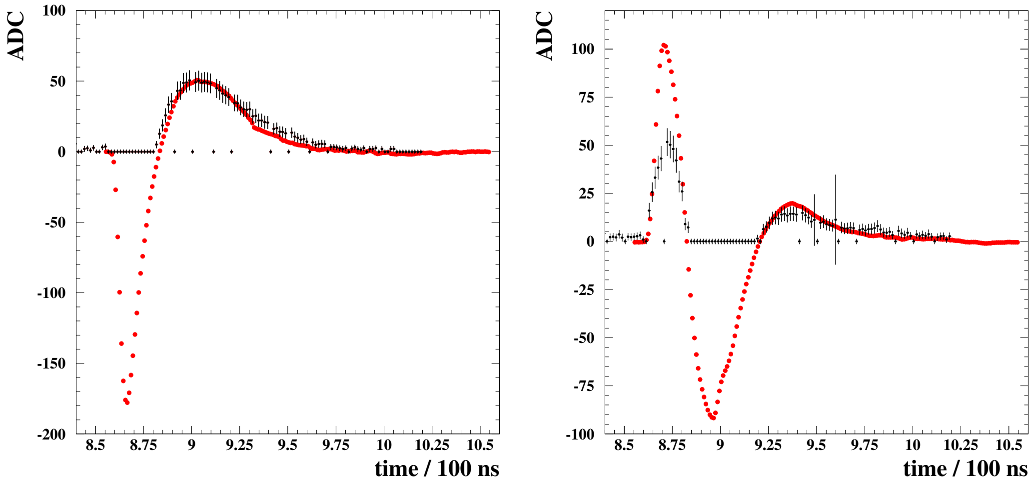

Figure 5.10: Comparison between Monte Carlo simulation (red) and data (black) for typical first order and second order signals

5.3 Summary

An unwanted cross talk effect is observed in the HARP TPC. The effect has been modelled and a special data taking run undertaken allowing the extraction of the necessary parameters to completely describe the effect. The cross talk effect can be split into self-talk, where there is a capacitive coupling between the output and the input of the same pad, and cross talk where there is a coupling between the output of one pad and the input of a different pad. Both of these effects are introduced into the Monte Carlo, with the possibility of using each effect with or without the other. The implementation is validated by comparing the results of the pulser runs with pulser runs in the Monte Carlo. Excellent agreement is found.

Chapter 6

Effect of Cross Talk

This chapter describes a study of the effect of cross talk on TPC measurements. Each of the studies described in this chapter has been performed using a single track Monte Carlo. 600 MeV positive pions were fired from the origin (the nominal target position) at three different angles in θ (the angle with respect to the beam axis): 80°, 60° and 40°, with a random angle in ϕ. The chapter begins with a description of the reconstruction independent study which was performed. Next the reconstruction algorithms used to reconstruct particle trajectories in the TPC are described, followed be a description of the effect of cross talk on each stage of the reconstruction chain.

6.1 Reconstruction Independent Study

A first study was carried out to look at the effect of cross talk independently of the reconstruction software. In order not to be biased by the method of cluster selection, the HARP reconstruction software was not used for the study. Instead a simple weighted mean method was used to find what the expected reconstructed position was. Since each event only contained one radial track it could be assumed that all hits which were found in a row belonged to the same point. A weighted mean was therefore used to calculate the reconstructed position in x and y according to the formula:

$$x = \frac{\sum_i x_i \times adc_i}{\sum_i adc_i}, \tag{6.1}$$

where i loops over all pads in the row, x_i is the position in x of the ith pad and adc_i is the sum over all ADC values in the series of the ith pad. A similar weighted mean of all pads in a cluster was used to calculate the time (and hence the reconstructed position in z). The time estimator for an individual pad was taken as the time of the peak of the ADC series.

6.1.1 $r\phi$ and z Residuals

The 'reconstructed' values were then compared with the Monte Carlo truth to find the resolution. The position of the particle was retrieved from the McTpcHits. This provides the position of the particle at 2 mm intervals. The position of the trajectory at the point of closest approach in the xy plane to the reconstructed position was taken as truth for position. Residuals were calculated for three different scenarios; firstly using the parameterised transfer functions (the ideal situation), secondly introducing the measured transfer functions (and therefore introducing the effects of self talk), and lastly introducing cross talk. The result of the study can be seen in Figures 6.1 and 6.2 and the results are summarised in Table 6.1. z distributions are fitted to a gaussian and $r\phi$ distributions to a double gaussian. The table shows the σ values of the gaussians. It is found that the TPC $r\phi$ residuals fit well to a double gaussian. The broader component is found to be associated to clusters with only one hit, or those which are in close proximity to dead pads [83][1]. In the following discussion emphasis will be given to the width of the narrow gaussian.

Parameter	Angle	Parameterised TF	Measured TF	With Cross Talk
$r\phi$ / mm	80°	0.36 (3.30)	0.66 (2.77)	0.82 (3.77)
$r\phi$ / mm	60°	0.36 (3.47)	0.63 (2.85)	0.78 (3.60)
$r\phi$ / mm	40°	0.32 (3.79)	0.60 (2.96)	0.73 (3.75)
z / mm	80°	1.59	2.21	3.38
z / mm	60°	2.09	2.74	3.88
z / mm	40°	2.74	3.94	5.06

Table 6.1: Summary of reconstruction independent study. σ values from gaussian fits are shown, for parameterised Transfer Functions (TF), measured TFs and with cross talk.

In $r\phi$ the width of the narrow gaussians shows a slight decrease with decreasing track angle. The increase in σ with respect to the ideal situation is $\sim$ 80 % for the

[1] The pulser measurements found a few pads on which there was only a very small signal, and others were missed. So these act as dead pads in the Monte Carlo.

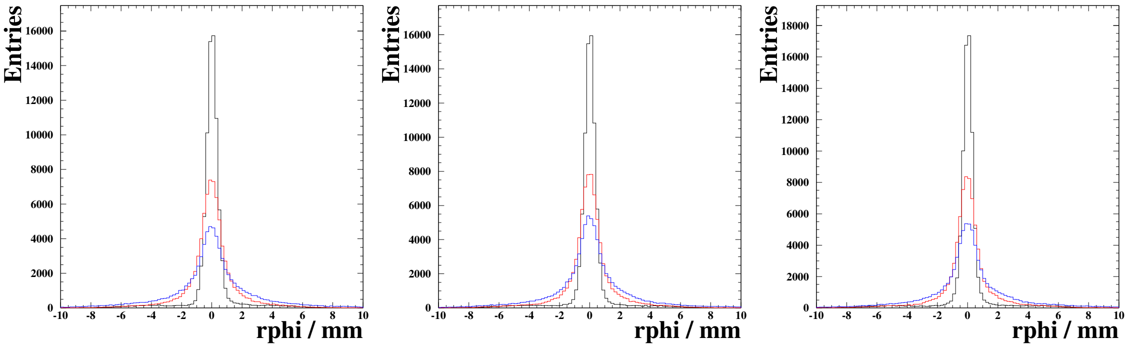

Figure 6.1: Resolution in $r\phi$ for 80° tracks (left), 60° tracks (middle), 40° tracks (right). Parameterised transfer functions are shown in black, measured transfer functions in red and with the addition of cross talk in blue.

measured transfer functions and $\sim$ 120 % for the addition of cross talk. For the wider gaussian an increase in σ as the angle decreases is seen for parameterised and measured transfer functions, while the width stays fairly constant with angle after the addition of cross talk.

In z the σ of the gaussian increases with decreasing angle for all cases. The increase in width of the narrow gaussian is $\sim$ 30 % for the measured transfer function, and $\sim$ 85 % for the addition of cross talk. After the addition of cross talk a large asymmetric tail and a slight shift of the peak position are observed. These are both an effect of the positive part of the first order cross talk signals being delayed with respect to the true signals.

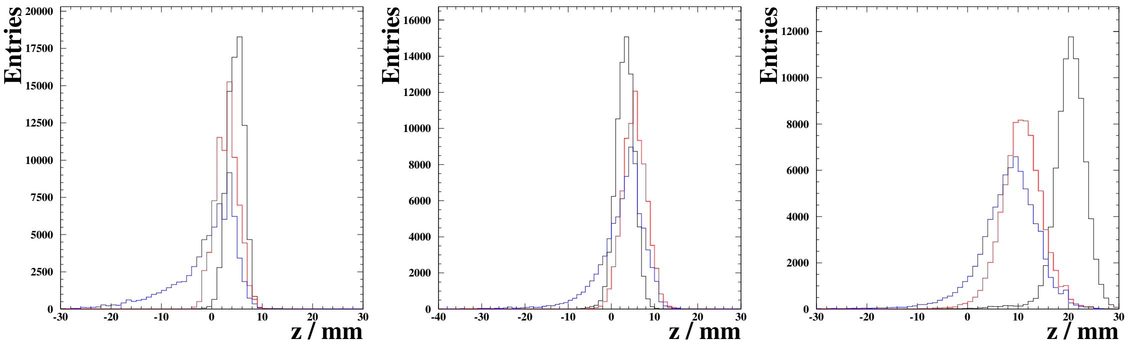

Figure 6.2: Resolution in z for 80° tracks (left), 60° tracks (middle), 40° tracks (right). Parameterised transfer functions are shown in black, measured transfer functions in red and with the addition of cross talk in blue

6.1.2 Effect of Measured Transfer Functions

In order to understand the effect of introducing the measured transfer functions, the changes with respect to parameterised transfer functions, introduced by their use, were examined separately. These are:

- The introduction of dead pads with the measured transfer functions due to unmeasured and dead pads in the TPC for which no transfer function is measured exists to be used in the Monte Carlo
- Large variations in gain introduced with measured transfer functions due to self talk and the much lower gains of pads with self talk
- Variations in integrated ADC and time estimators due to the varying signal shapes for measured transfer functions

In order to understand the effects of these different factors, two new sets of conditions were studied. First parameterised transfer functions were studied with the same distribution of dead pads as is found in the measured transfer functions. Second, instead of correcting for the unequalised gains of the transfer functions during reconstruction by applying a gain factor, the gains were equalised inside the simulation, and the gas gain was altered to make the mean gain with measured transfer functions equal to that for parameterised transfer functions. The results can be seen in Figures 6.3 and 6.4 and Table 6.2.

Parameter	Conditions	σ (narrow)	σ (wide)	RMS
$r\phi$ / mm	param	0.36	3.30	1.32
$r\phi$ / mm	param + dead	0.36	3.56	1.68
$r\phi$ / mm	meas	0.65	2.76	1.71
$r\phi$ / mm	meas + inc. gain	0.44	3.26	1.66
z / mm	param	1.59	-	2.25
z / mm	param + dead	1.61	-	2.34
z / mm	meas	2.23	-	2.89
z / mm	meas+ inc. gain	2.19	-	2.98

Table 6.2: Summary of the contributions to $r\phi$ and z residuals of different effect of self talk. σ values from gaussian fits and RMS values are shown.

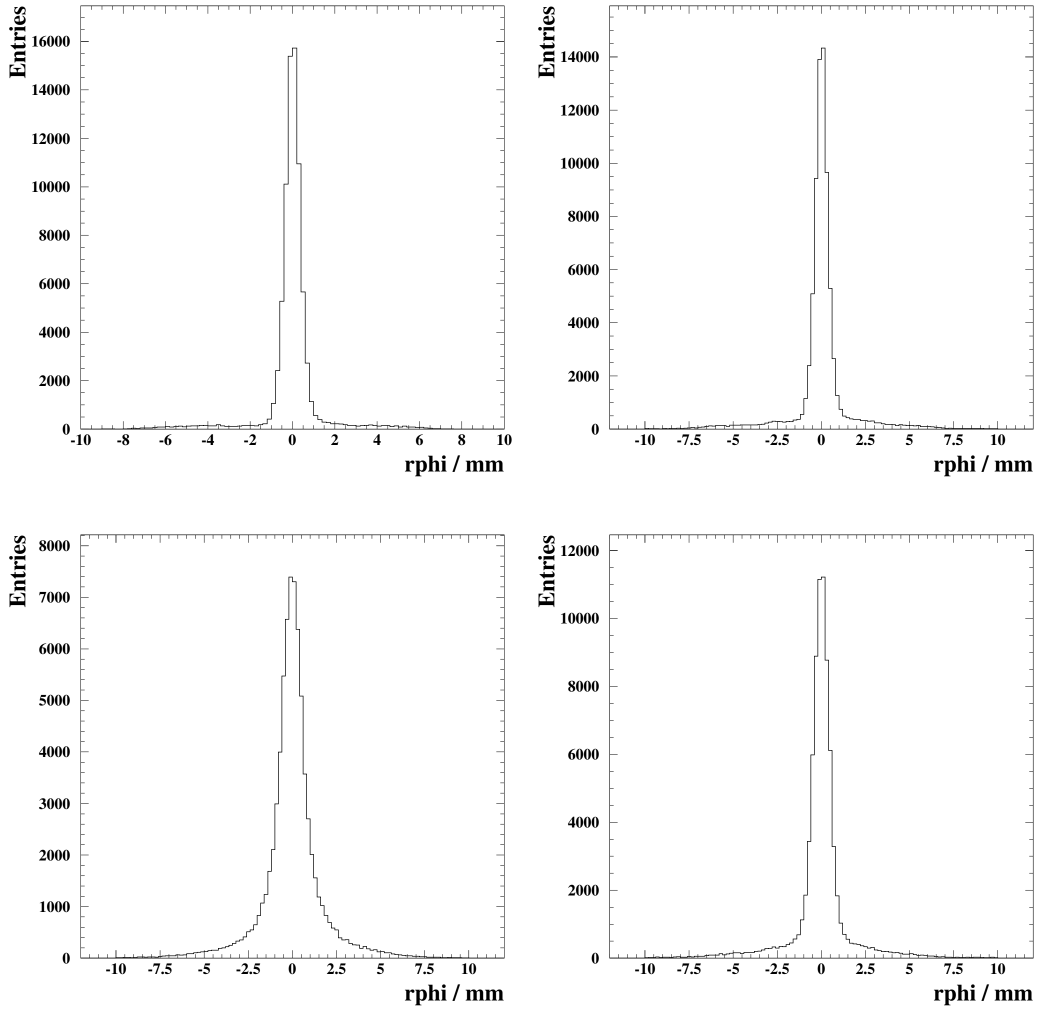

Figure 6.3: Distributions of $r\phi$ residuals. Top left shows parameterised transfer functions with all pads live, top right shows parameterised transfer function with the dead map of measured transfer functions, bottom left shows measured transfer functions, bottom right shows measured transfer functions with mean gain equal to that of parameterised transfer functions.

It is observed that the width of the narrow gaussian in $r\phi$ is dominated by the difference in gain between the measured and parameterised transfer function. The RMS of the $r\phi$ distribution however is dominated by the effects of dead pads. In z little change in the distribution is observed after these two changes, so we can assume that here the changes in signal shape are dominant.

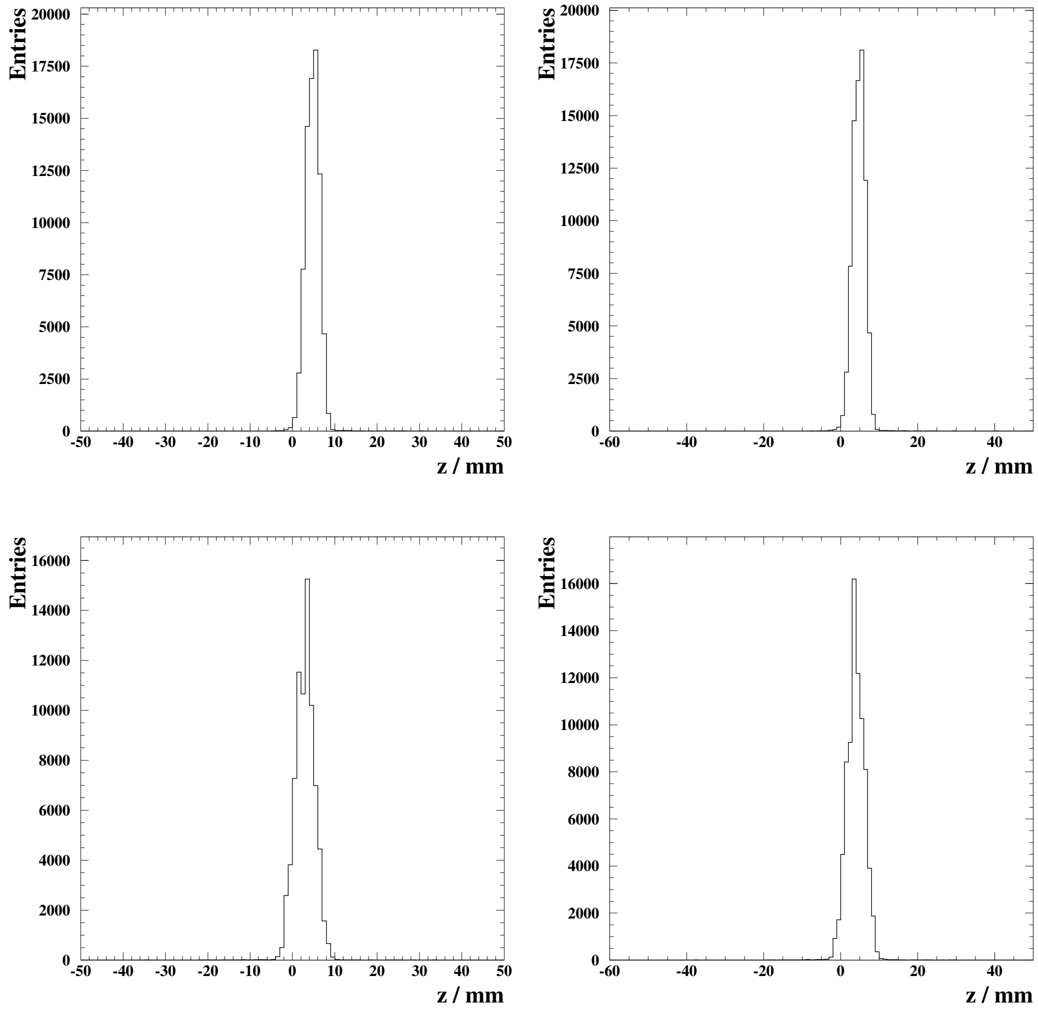

Figure 6.4: Distributions of z residuals. Top left shows parameterised transfer functions with all pads live, top right shows parameterised transfer function with the dead map of measured transfer functions, bottom left shows measured transfer functions, bottom right shows measured transfer functions with mean gain equal to that of parameterised transfer functions.

6.2 Description of Reconstruction Chain

The reconstruction chain proceeds in several steps which are depicted in Figure 6.5. These are:

- Equalisation of pad gains performed by CalibrateTpcAlg
- Clustering performed by TpcClusterAlg
- Pattern recognition performed by FindTpcTracksAlg
- Track fitting performed by FitTpcTracksAlg

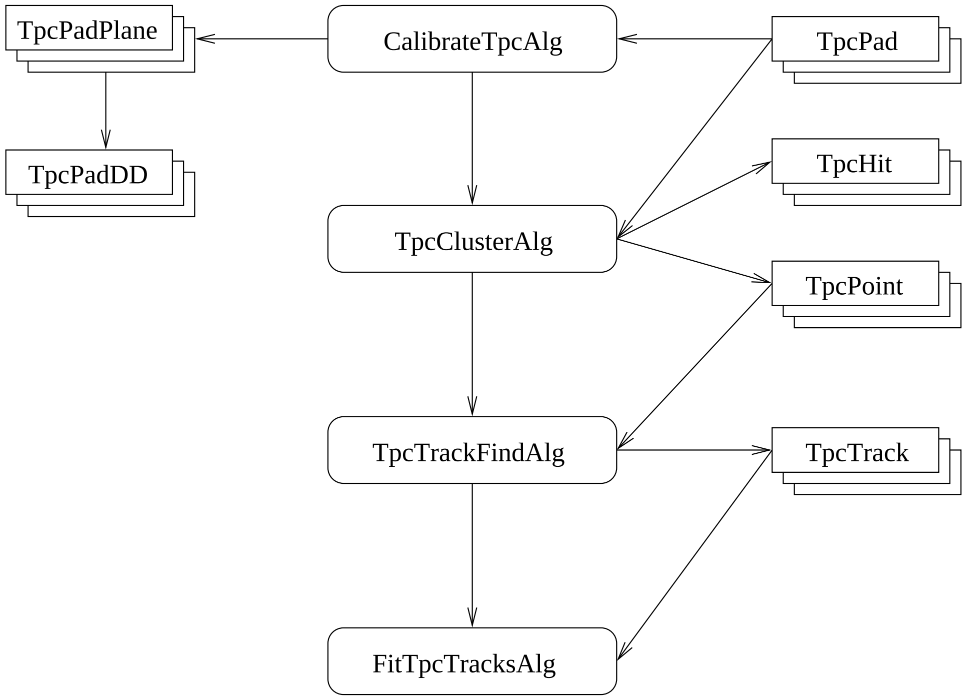

Figure 6.5: Diagram of inter-relation of objects and algorithms which perform the reconstruction of TPC tracks. Square boxes indicate data objects and round edged boxes indicate algorithms.

This can be followed by a refit of the track performed by the Kalman Filter using these parameters as input but at the time of writing this produces unreliable results at large angles with respect to the beam axis and for this reason is not used. Each step will be described in more detail below.

6.2.1 Equalisation

The equalisation is performed first with the calibration constants obtained using the calibration techniques described in Chapter 2. Each ADC value is simply divided by the equalisation constant for that pad and stored into the TpcPad.

6.2.2 Clustering

The clustering creates space points with an associated ADC value in the TPC [83]. This process is performed in 3 steps:

- Creation of hits in each pad [2]

[2]The signal on each pad is separated into a new hit each time the signal falls below a software threshold

- Decision about which hits belong in the same point
- Calculation of position and ADC value of each point

The creation of hits is done by dividing the ADC series each time the ADC value falls below a software threshold of 5 ADC counts, or there is a time gap of 100 ns (1 bin). Each hit is then assigned an xy position which is defined by the position of the pad, an ADC value defined by the sum of all ADC values making up the hit and a time. The time is defined as the point at 50% of the peak value, and is calculated by a linear interpolation from the peak time and the leading time (see Figure 6.6).

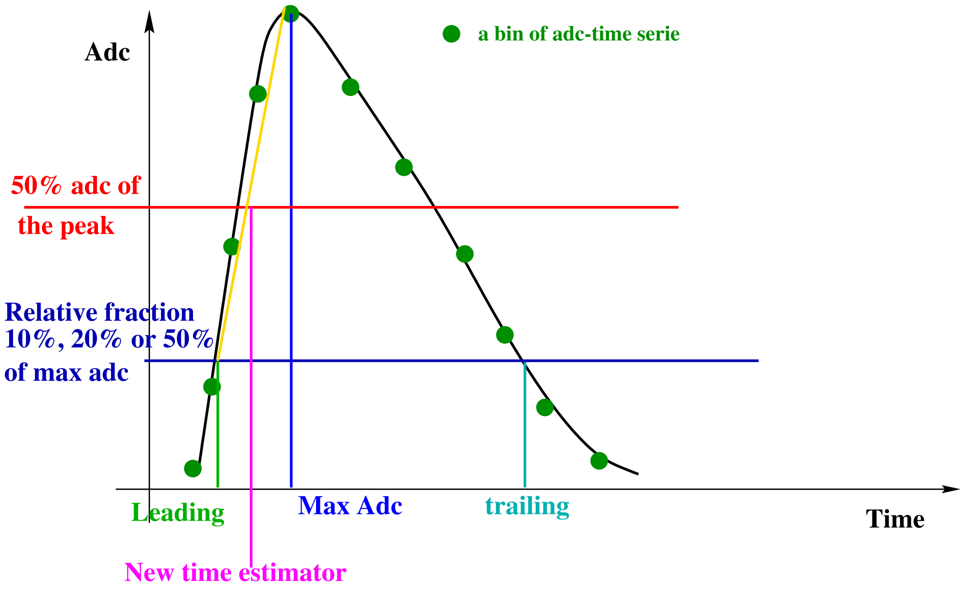

Figure 6.6: Diagram showing how the time estimator of TPC hits is calculated [83].

Next the hits are grouped into clusters. This is done row by row so for the ideal case 20 points are expected for a track which traverses the whole radius of the TPC (1 in each of the 20 rows in the TPC). Hits are considered to be in the same cluster if they belong to neighbouring pads in the same row, and if the signals are close in time (a maximum gap of 600 ns).

The final step is to define the position and ADC value of the cluster. The position is defined by a weighted mean of the positions of the pads in the cluster in x, y and time (see Equation 6.1). The z position can then be calculated using:

$$z = v_{drift} \times t \tag{6.2}$$

The ADC of the cluster is taken as the sum of all ADCs of hits in the cluster.

6.2.3 Pattern Recognition

The next step of the reconstruction is to decide which points belong in the same track. The pattern recognition makes no assumption that the track should be helical but builds up links between points. The pattern recognition starts from the outside of the TPC where the tracks will be further apart. Using the links in the outer region as seeds a line is created that connects the points, and further points are searched for in a truncated cone with its axis defined by this line. The parameters of the algorithm are the radius, opening angle and forward acceptance of the cone (See Figure 6.7) [84]. When points are found they are added to the track candidate and the procedure is repeated until the inner radius of the detector is reached.

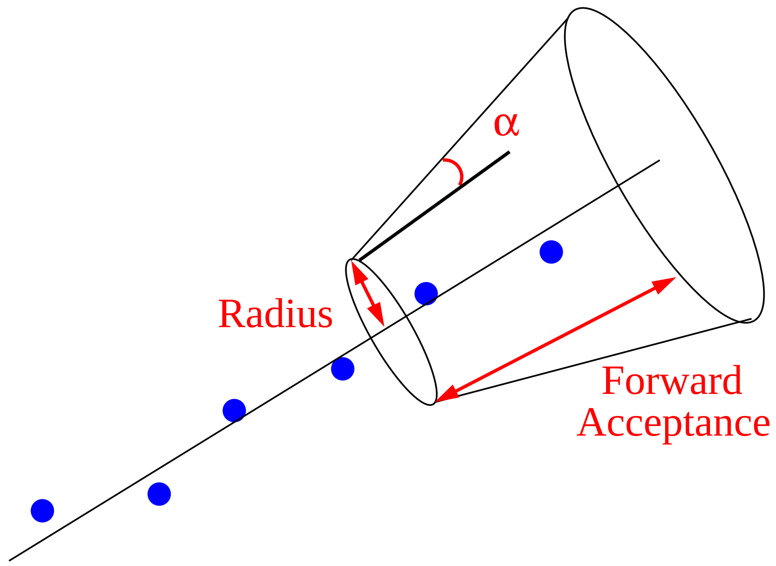

Figure 6.7: Diagram showing the parameters used by the pattern recognition.

6.2.4 Track Fitting

Once points belonging to the same track have been identified a helical fit to these points is performed to find the track parameters. The fit is performed in two steps: a circular fit in the xy plane is done first, and this is followed by a straight line fit in the $s_{xy}z$ plane, where s_{xy} is the length of the arc in the xy plane. The fit can be described by five parameters. The chosen parameters for HARP are shown in Figure 6.8 These are [85]:

- ρ the inverse of the radius of curvature
- d_0 the impact parameter in the xy plane

- ϕ_0 the angle between the projection in the xy plane of the particle's momentum at the impact point and the x axis
- $\tan\lambda$ the dip angle
- z_0 the z coordinate at the impact point

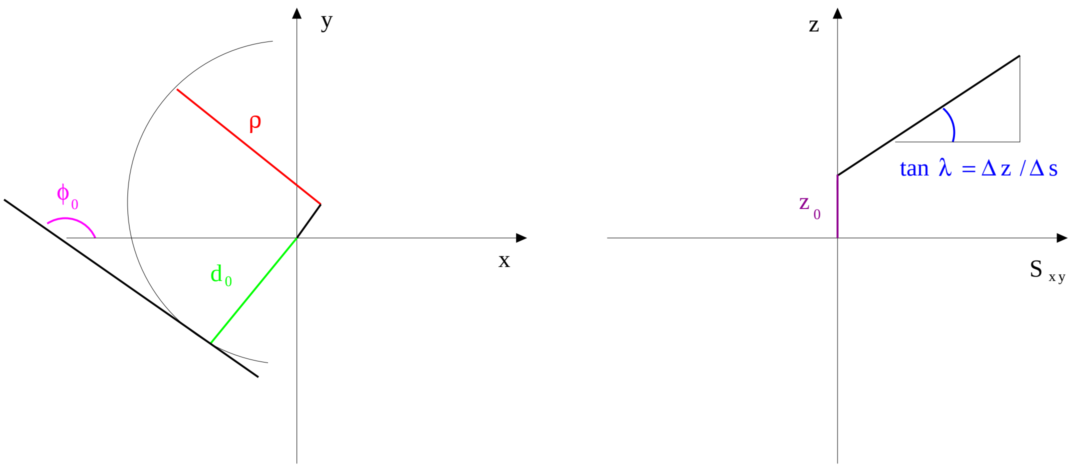

Figure 6.8: Diagram showing the fit parameters of the helix fit.

The track fit returns a flag indicating pathological cases such as tracks with too few points, or too large or too small radius for a reliable fit. If the track does not fall into any of these categories then it is returned with a flag of 0.

6.3 Effect of Cross Talk on Reconstructed Observables

Since the important effect of cross talk is its effect on final measured observables such as p_t and p_l it was decided to study the affect of cross talk on all stages of the reconstruction chain described above. For each of the studies 600 MeV pions at 80°, 60° and 40° were used as described in the previous section. Again each observable was examined in three conditions: parameterised transfer functions, measured transfer functions and with cross talk.

6.3.1 Clusters

First the effect of cross talk on the clustering was studied. The effect on residuals in $r\phi$ is shown in Figure 6.9 and that on z in Figure 6.10. The results of a double gaussian fit to the $r\phi$ distributions and a gaussian fit to the z distributions can be seen in Table 6.3. It can be seen that the widths of the narrow gaussians for $r\phi$ are larger than those found in the previous study while the widths of the z distributions are smaller than those found in the previous study. An examination of the number of hits in a cluster compared to the number of hits per row found in the previous study, shows a decrease of 0.5 hits per event. This has clear consequences for residual widths in $r\phi$ since a missing hit will bias the position of the point. The hits are excluded by the clustering because they are too far apart in z. This is also the reason for the narrower residuals in z.

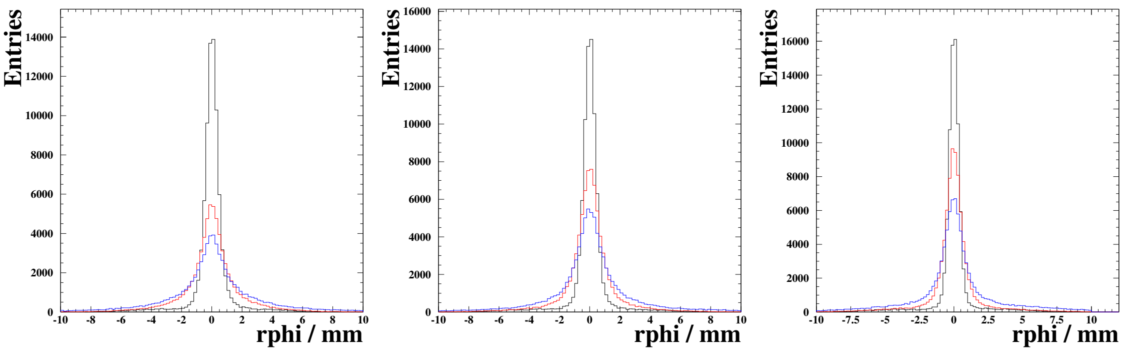

Figure 6.9: Resolution in $r\phi$ of clusters for 80° tracks (left), 60° tracks (middle), 40° tracks (right). Parameterised transfer functions are shown in black, measured transfer functions in red and with the addition of cross talk in blue.

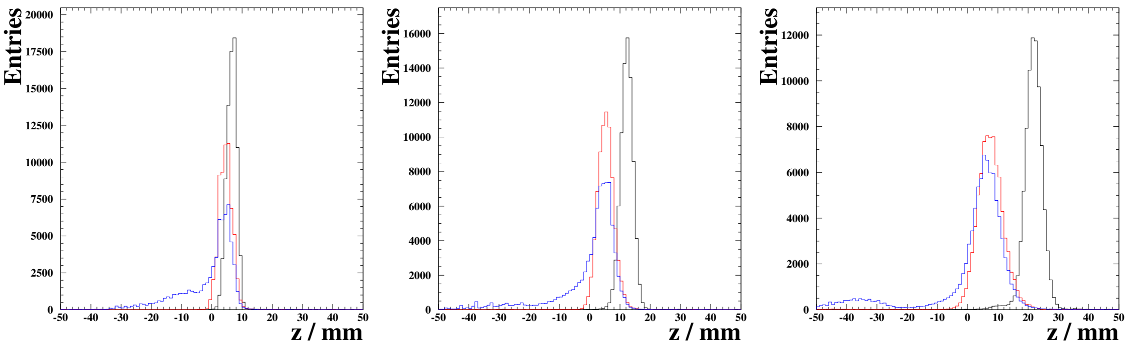

Figure 6.10: Resolution in z of clusters for 80° tracks (left), 60° tracks (middle), 40° tracks (right). Parameterised transfer functions are shown in black, measured transfer functions in red and with the addition of cross talk in blue.

In $r\phi$ the σ of the narrow gaussian decreases with angle for parameterised transfer functions. For measured transfer functions and cross talk the increase with respect

Parameter	Angle	Parameterised TF	Measured TF	Cross Talk
$r\phi$ / mm	80°	0.42(3.00)	0.72(2.76)	0.91(3.96)
$r\phi$ / mm	60°	0.40(3.11)	0.71(2.95)	0.88(4.02)
$r\phi$ / mm	40°	0.35(3.57)	0.60(3.62)	0.75(4.69)
z / mm	80°	1.56	2.06	2.91
z / mm	60°	2.00	2.57	3.72
z / mm	40°	2.65	4.06	4.94
npts	80°	20.22	16.43	17.35
npts	60°	20.33	19.36	20.53
npts	40°	20.40	20.55	22.70
npts RMS	80°	1.64	3.65	3.58
npts RMS	60°	1.36	2.60	3.06
npts RMS	40°	1.19	2.00	3.08

Table 6.3: Summary of clustering study. Shown are σs of a double gaussian fit to $r\phi$ residual distributions, σ of gaussian fit to z residual distribution and mean and RMS values of the number of points found per event.

to parameterised transfer functions is ~ 70 % at all angles and for the addition of cross talk it is ~ 115 % at all angles.

In z the widths of the distributions increase with decreasing angle. The increase of measured transfer functions is around 30 % with respect to parameterised transfer functions and for the addition of cross talk the increase is around 85 %. Again a large asymmetric tail is seen after the addition of cross talk. At 40° where the cross talked signals are shifted by a larger amount with respect to original signals due to the longer signal shapes, this forms a second peak since the signals are too far apart in time to be considered as part of the same cluster and therefore two clusters are created.

The number of points found per event is also shown in Table 6.3 and the distributions in Figure 6.11. For parameterised transfer functions a number of just over twenty per row is found as expected for tracks which traverse the radius of the TPC. The numbers are lower for measured transfer functions. A decrease of 20 % is observed at 80° with respect to parameterised transfer functions, but the numbers are comparable at 40°. In the previous chapter it was stated that the gains of pads with self talk were smaller than those without. This decrease in the gain in a large number of pads means that clusters visible without the effects of self talk fall below the hardware threshold when self talk is introduced. As we go to smaller angles the track length across a pad and therefore the charge induced increase, so the effect is lessened. A small increase in the average number of hits after the addition of cross talk is observed. This is due to clusters which consist of pure cross talk.

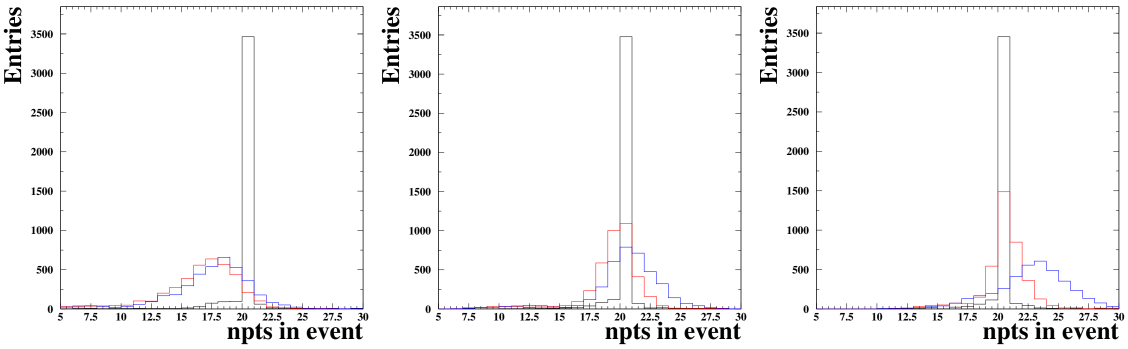

Figure 6.11: Number of clusters found in an event for 80° *tracks (left),* 60° *tracks (middle),* 40° *tracks (right). Parameterised transfer functions are shown in black, measured transfer functions in red and with the addition of cross talk in blue.*

6.3.2 Pattern Recognition

Next the effect of cross talk on the pattern recognition was studied. Figure 6.12 shows the number of points found by the pattern recognition, and Table 6.4 shows the mean and RMS values. Also shown is the ratio of points created to points found. It should be noted that while this is labelled 'efficiency', for cross talk this value is really underestimated, since points consisting of pure cross talk which are not picked up should not be considered to be decreasing the efficiency. It can be seen that while use of measured transfer functions has little effect at 80°, inefficiency is seen as the angle decreases with an inefficiency of 5 % at 40°. Again this happens due to the magnification of distortions at large angles due to larger signal shapes. Cross talk decreases the efficiency of the pattern recognition by around 10-15 %.

Figures 6.13 and 6.14 show the residuals in $r\phi$ of points which are included in the track and those which are not included in the track. Figures 6.15 and 6.16 show the same distributions in z. These plots make it clear that the problems in the pattern recognition are caused by shifts in the z coordinate for cross talk. The effects of the clustering can again be seen in the peak of z values at large and positive values of z. Several peaks are clearly visible in the cross talk distributions and these are believed to correspond to offsets in the time coming from 1st and 2nd order crosstalk. This theory is supported by the fact that the peaks are further apart for more inclined tracks.

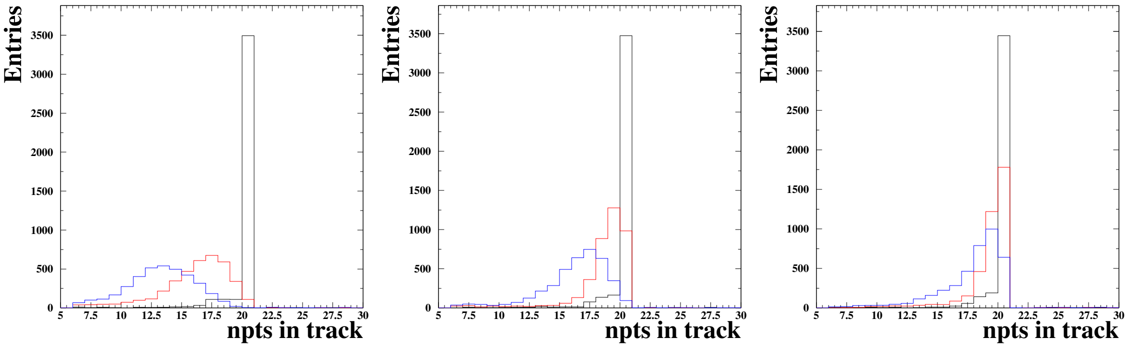

Figure 6.12: Number of points found by pattern recognition for 80° tracks (left), 60° tracks (middle), 40° tracks (right). Parameterised transfer functions are shown in black, measured transfer functions in red and with the addition of cross talk in blue.

Parameter	Angle	Parametrised TF	Measured TF	Cross Talk
npts in track	80°	20.13	16.16	13.37
npts in track	60°	20.17	18.72	16.36
npts in track	40°	20.19	19.39	17.95
npts	80°	20.22	16.43	17.35
npts	60°	20.33	19.36	20.53
npts	40°	20.40	20.55	22.70
efficiency	80°	0.996	0.999	0.872
efficiency	60°	0.993	0.976	0.887
efficiency	40°	0.990	0.953	0.854

Table 6.4: Summary of pattern recognition study. Shown are the average number of points per event, the average number of points per track and the ratio of these two numbers.

6.3.3 Track Reconstruction

Lastly the effect of cross talk on the reconstructed momentum was studied. Plots of the total momentum can be seen in Figure 6.17, longitudinal momentum in Figure 6.18 and transverse momentum in Figure 6.19. Means, sigmas and RMS values are given in Table 6.5. The distributions are not strict gaussians and the difference from a gaussian is worse for measured transfer functions and cross talk. The sigmas are therefore only indicative of the width of the distribution.

A broadening of the momentum distributions with the addition of cross talk and self talk can be seen. The percentage of broadening is seen to increase with

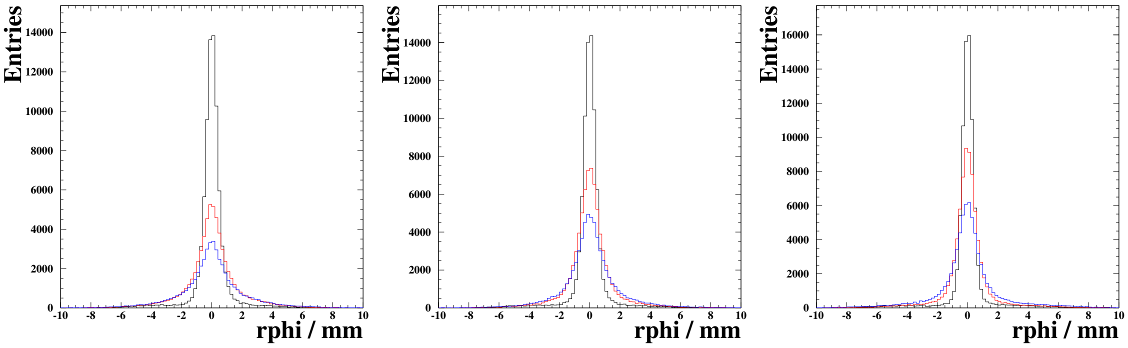

Figure 6.13: Resolution in $r\phi$ of clusters found by pattern recognition for 80° tracks (left), 60° tracks (middle), 40° tracks (right). Parameterised transfer functions are shown in black, measured transfer functions in red and with the addition of cross talk in blue.

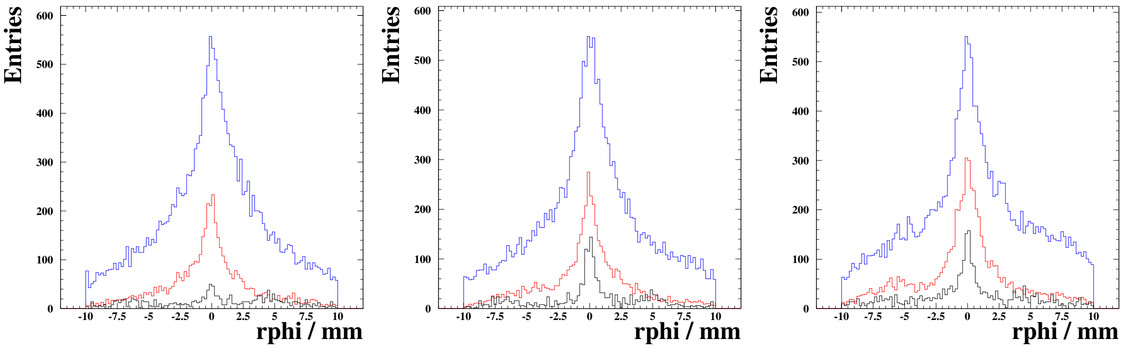

Figure 6.14: Resolution in $r\phi$ of points not found by pattern recognition for 80° tracks (left), 60° tracks (middle), 40° tracks (right). Parameterised transfer functions are shown in black, measured transfer functions in red and with the addition of cross talk in blue.

decreasing angle. For measured transfer function this amounts to an increase from 70 % to 168 % for p_t and an increase from 94 % to 169 % in p_l. For the addition of cross talk the increase goes from 119 % to 245 % in p_t and from 134 % to 227 % in p_l. A bias in the peak positions to lower values is also seen for measured transfer functions, and this becomes worse with the addition of cross talk.

6.4 Summary

The inclusion of self talk and cross talk are found to have severe consequences at all stages of the reconstruction chain. The combination increases the σ of residuals in $r\phi$ by 115 %. For z residuals an increase of 85 % is found. This has knock on effects for the pattern recognition which shows a decrease in efficiency from 99 % to just 85 % at 40°. The overall result is an increase in the width of momentum distributions

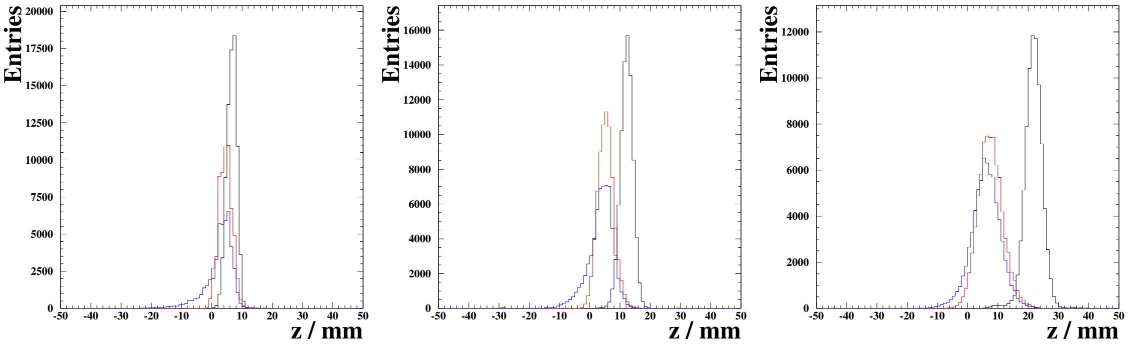

Figure 6.15: Resolution in z of points found by pattern recognition for 80° tracks (left), 60° tracks (middle), 40° tracks(right). Parameterised transfer functions are shown in black, measured transfer functions in red and with the addition of cross talk in blue.

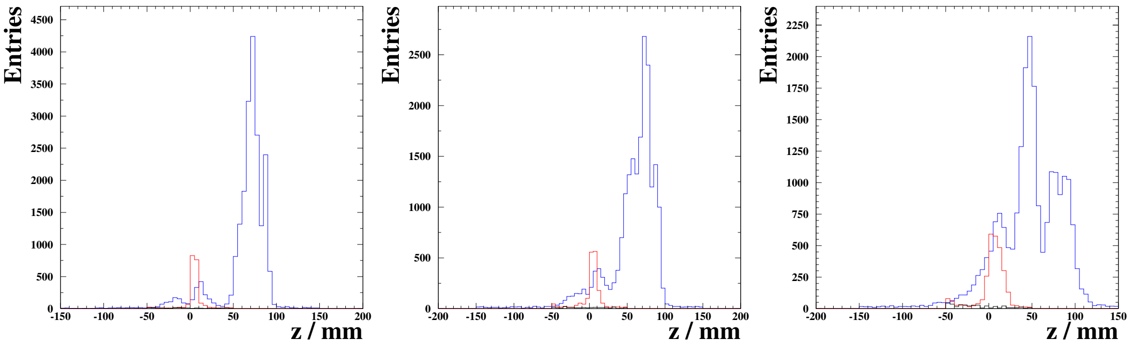

Figure 6.16: Resolution in z of points not found by pattern recognition for 80° tracks (left), 60° tracks (middle), 40° tracks (right). Parameterised transfer functions are shown in black, measured transfer functions in red and with the addition of cross talk in blue.

of the order of 220 % as well as a shift of the peak to lower values.

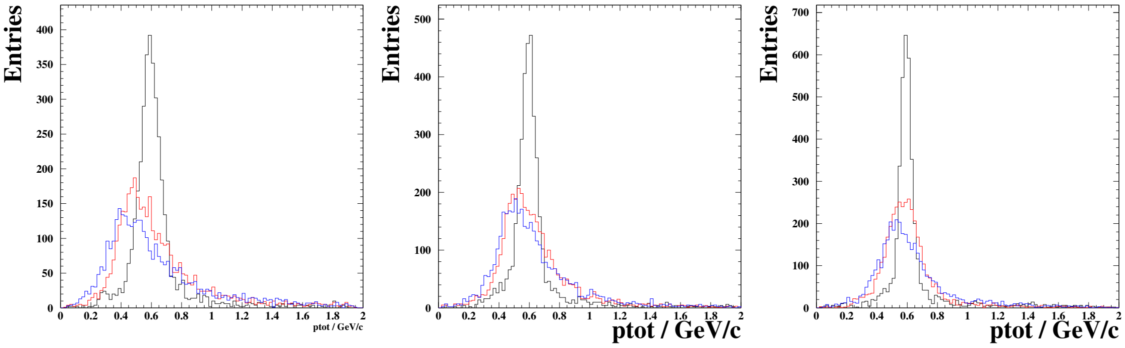

Figure 6.17: Total momentum for 80° tracks (left), 60° tracks (middle), 40° tracks(right). Parameterised transfer functions are shown in black, measured transfer functions in red and with the addition of cross talk in blue.

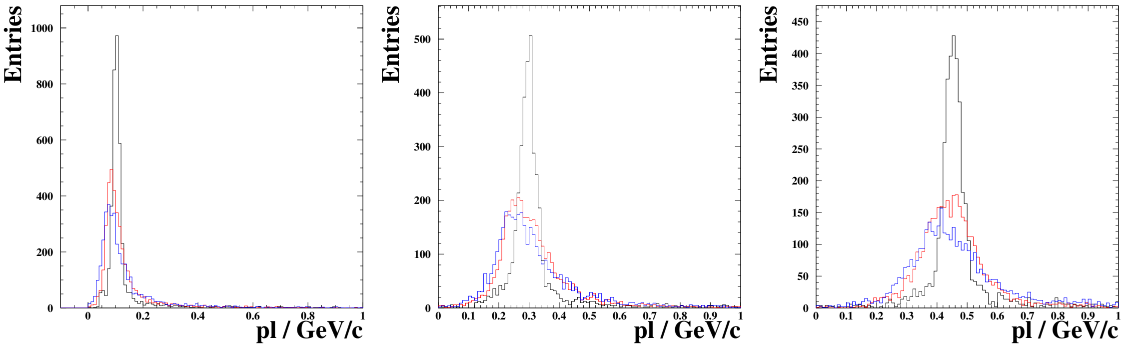

Figure 6.18: Longitudinal momentum for 80° tracks (left), 60° tracks (middle), 40° tracks (right). Parameterised transfer functions are shown in black, measured transfer functions in red and with the addition of cross talk in blue.

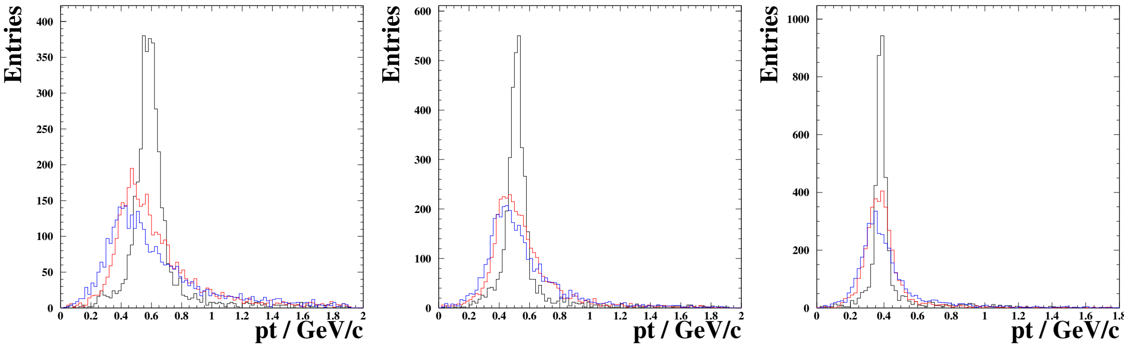

Figure 6.19: Transverse momentum for 80° tracks (left), 60° tracks (middle), 40° tracks (right). Parameterised transfer functions are shown in black, measured transfer functions in red and with the addition of cross talk in blue.

Parameter	Angle	Parametrised TF	Measured TF	Cross Talk
p_{tot} offset / GeV/c	80°	0.59	0.53	0.49
p_{tot} offset / GeV/c	60°	0.59	0.57	0.53
p_{tot} offset / GeV/c	40°	0.59	0.57	0.56
p_{tot} σ / GeV/c	80°	0.078	0.157	0.185
p_{tot} σ / GeV/c	60°	0.062	0.133	0.153
p_{tot} σ / GeV/c	40°	0.043	0.111	0.140
p_{tot} RMS / GeV/c	80°	0.212	0.302	0.341
p_{tot} RMS / GeV/c	60°	0.206	0.254	0.281
p_{tot} RMS / GeV/c	40°	0.228	0.207	0.267
p_l offset / GeV/c	80°	0.10	0.10	0.09
p_l offset / GeV/c	60°	0.30	0.28	0.27
p_l offset / GeV/c	40°	0.46	0.44	0.42
p_l σ / GeV/c	80°	0.0144	0.0280	0.0338
p_l σ / GeV/c	60°	0.0311	0.0691	0.0754
p_l σ / GeV/c	40°	0.0321	0.0865	0.1050
p_l RMS / GeV/c	80°	0.098	0.105	0.126
p_l RMS / GeV/c	60°	0.104	0.128	0.141
p_l RMS / GeV/c	40°	0.102	0.119	0.156
p_t offset / GeV/c	80°	0.58	0.51	0.49
p_t offset / GeV/c	60°	0.51	0.49	0.48
p_t offset / GeV/c	40°	0.38	0.37	0.37
p_t σ / GeV/c	80°	0.0770	0.1309	0.1691
p_t σ / GeV/c	60°	0.0542	0.1186	0.1420
p_t σ / GeV/c	40°	0.0294	0.0788	0.1016
p_t RMS / GeV/c	80°	0.209	0.298	0.336
p_t RMS / GeV/c	60°	0.200	0.230	0.255
p_t RMS / GeV/c	40°	0.171	0.171	0.222

Table 6.5: Effect of cross talk on momentum resolution.

Chapter 7

Design of a Cross Talk Correction

This chapter describes a method for cross talk correction based on the model described in chapter 5. The basic principle of the method is to predict the cross talk signal induced on each pad and subtract it from the recorded signal, inverting the process implemented in the Monte Carlo. The problems encountered by this approach and the methods used to overcome them will be detailed. A description of the software structure used to implement the method is also described.

7.1 Subtraction of Signal Shapes

The general principle of the cross talk correction described in this chapter is to predict the cross talk signal on a pad using the model described in chapter 5, which predicts the cross talk signal on a pad using the fourier transforms of the transfer functions of the mother and daughter pads along with their gains and the capacitive coupling between the two pads. This is subtracted from the signal recorded on that pad in order to obtain the pad's original signal. This general principle is illustrated in Figure 7.1. The top series of plots shows the process of calculating the cross talked signal in the Monte Carlo. The initial signal of the pad is shown on the left, the cross talked signal calculated from the signal on the mother pad is shown in the centre, and the resulting signal after addition of original signal and cross talk signal is shown on the right.

The plot in the centre indicates the signal shape which results from the TPC readout. The binning goes from the 10 ns binning used to calculate signal shapes in the Monte Carlo, to the 100 ns binning provided by the readout. Hardware threshold and pre and post samples are also applied as described in chapter 4. In order to go back to 10 ns binning allowing more detail in the signal shape to be observed, a spline interpolation of the series is used. The result of this can be seen on the bottom left. The cross talk signal can then be predicted in the same way as in the Monte Carlo; after subtraction of this signal shape the original signal on this pad is obtained.

7.2 Deconvolution to Obtain Charge Distribution

As detailed in chapter 5 the problem of cross talk falls into two separate classes; firstly self talk where the output of an amplifier is coupled to its own input, changing significantly the shape of the signal and secondly cross talk from one pad to another, when the input of one pad is coupled to the output of another, with the effect that a signal on the mother pad induces a signal on the daughter. The first problem is easy to correct as can be seen in Figure 7.2. Since the response of each pad to a delta input has been measured and the signal on a pad is the convolution of the input charge with the pad's transfer function. The original correlation between charge and energy input can be regained by deconvolving the measured signal with the pad's transfer function.

An example of the deconvolution process can be seen in Figure 7.3. The transfer function of the pad can be seen on the left, the signal on this pad for a particular event in the centre, and the deconvolution of the signal shape with the pad's transfer function on the right. The deconvolution is performed using GSL FFT functions [81].

The problem of cross talk between different pads is more complex. Since it was expected that all signals would be positive, only the positive part of the signal is recorded. The impact of this can be seen in Figure 7.4. Since the positive part of a signal resulting from cross talk is equal to the negative part, cross talk has no impact on the integral of the deconvolved distribution if the negative part of the signal is included, as can be seen in the central plot. However since in HARP's readout the negative part of the signal is removed the deconvolution is no longer effective, as can be seen in the right hand plot.

7.3 Limitations Of Signal Shape Subtraction

The reason that this loss of the negative part of the signal is important is illustrated in Figure 7.5. The plot shows the original signal, the cross talked signal and the resulting signal once cross talk is added. It can be seen that after addition of cross

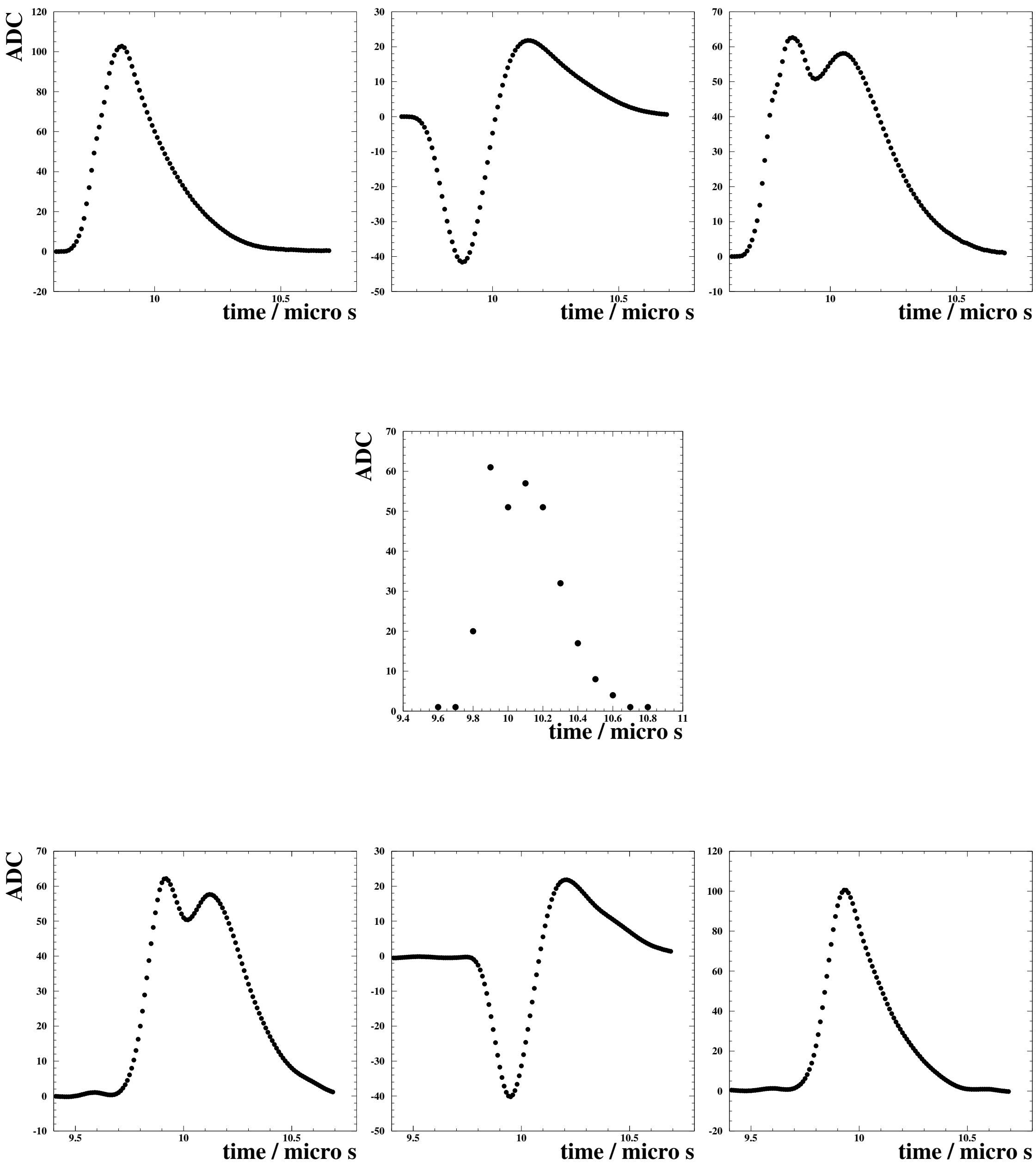

Figure 7.1: Signal shapes of original Monte Carlo signal (top left), calculated cross talk signal (top middle), resulting signal (top right), signal shape provided by TPC readout (centre), signal obtained by spline interpolation (bottom left), predicted cross talk signal (bottom middle), result of subtraction (bottom right).

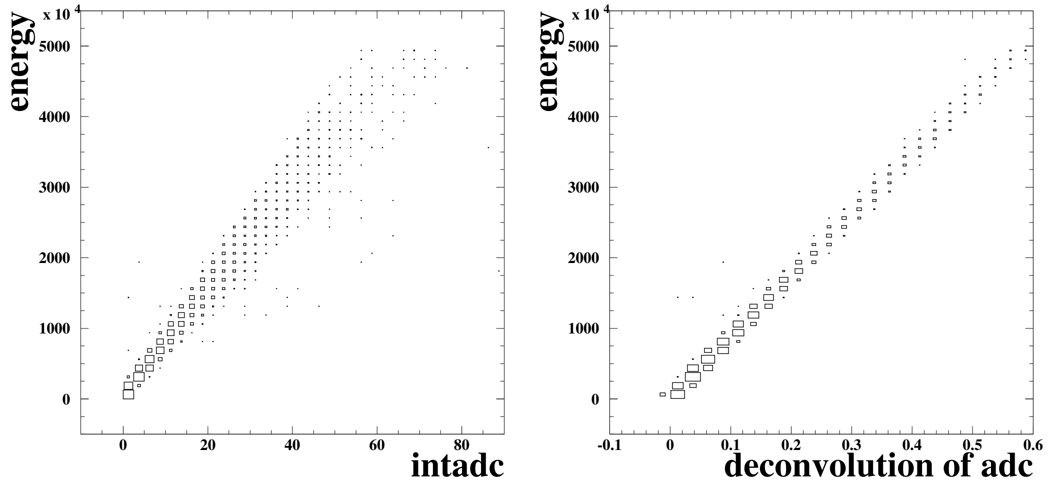

Figure 7.2: Input energy against integrated ADC (on left) and input energy against ADC series deconvolved with the measured transfer function (on right) for events with no cross talk added but using measured transfer functions

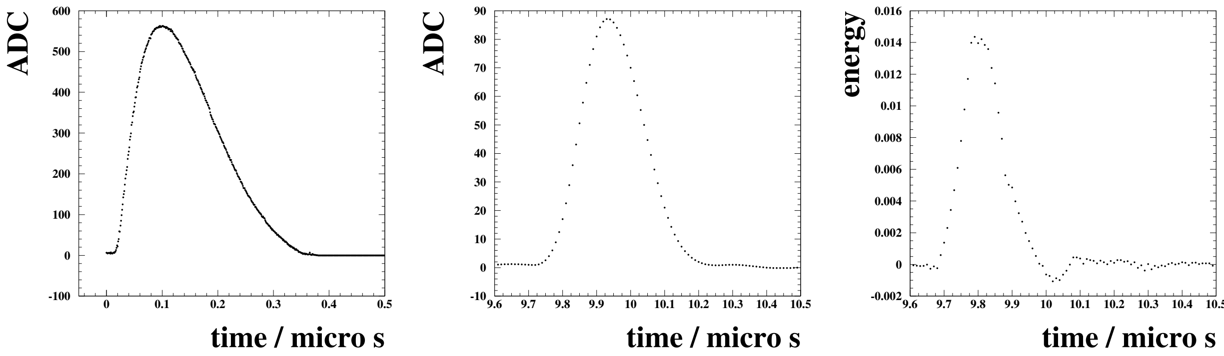

Figure 7.3: Transfer function of pad (left), example of a signal shape on that pad (centre), deconvolution of this signal with the pads transfer function (right)

talk part of the signal is negative. This occurs in the region where the negative swing of cross talk is greater in amplitude than the original signal. This region is indicated by the yellow shading. When this signal is recorded the negative part will disappear. Therefore even if the cross talk signal is correctly reproduced, subtraction of this signal will overestimate the value of the original signal in the region where the result was a negative signal, by an unknown factor.

This means that for all bins where there is a negative cross talk signal and the measured signal is zero the original signal cannot be correctly calculated. For this reason no subtraction is attempted in these bins. For any signal where subtraction was possible in every bin, it can be assumed that this signal has been completely corrected. Such an example can be seen in Figure 7.6. It is also easy to see that in

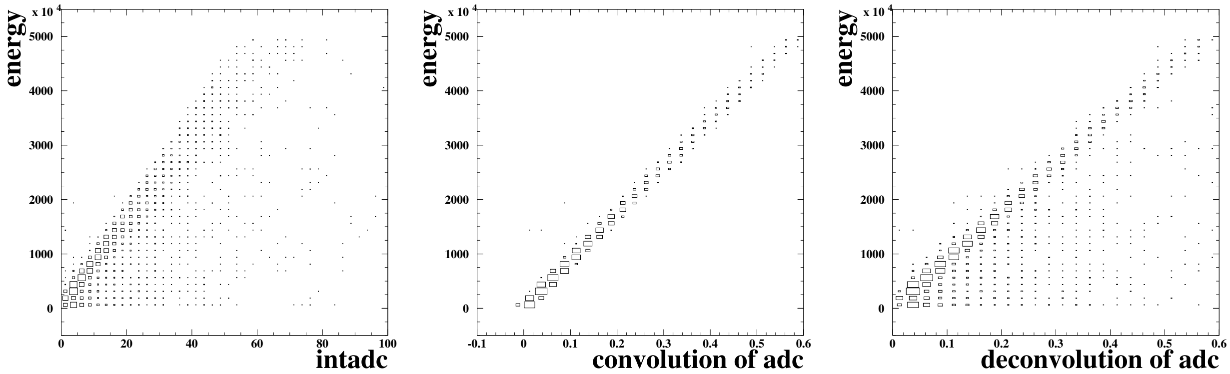

Figure 7.4: Input energy against integrated ADC (left), whole ADC series deconvolved with measured transfer (center), positive part of ADC series deconvolved with measured transfer function (right)

any case where all, or almost all of the bins are empty, then all information about the original signal has been lost and the signal therefore cannot be corrected, an example can be seen in Figure 7.6. For cases in between these two extremes two different methods are employed to recover the information that is lost.

In the case where a reasonably small number of bins are lost, particularly when these bins are not across the peak of the signal, interpolation between the points that were recovered can be done using a spline fit. An example of this can be seen in Figure 7.7

If a larger number of bins is lost, particularly if these bins are around the peak of the distribution, an alternative method is needed to correctly find the original signal shape. As mentioned above the signal on a particular pad comes from the convolution of the pad's transfer function with the charge distribution that went into the pad's amplifier. This knowledge can be used to predict the signal shape expected on a given pad. It can be assumed that the signals on pads in close proximity to the pad on which the signal is being recovered will have been caused by the same track and will therefore have a similar charge distribution. The charge distribution on any pad can be found by deconvolving the signal on this pad with the transfer function of this pad, provided the pad is unaffected by cross talk, or the cross talk has been corrected. This means that the expected signal shape on the pad of interest can be found by taking the charge distribution of a nearby pad and convolving with the transfer function of the pad for which the original signal shape is being found.

While this is expected to give the correct shape for the pad signal, the amplitude of the signal will depend on various factors such as the gains of the pads, and how close the pad is to the track. The amplitude of the signal is found using the part

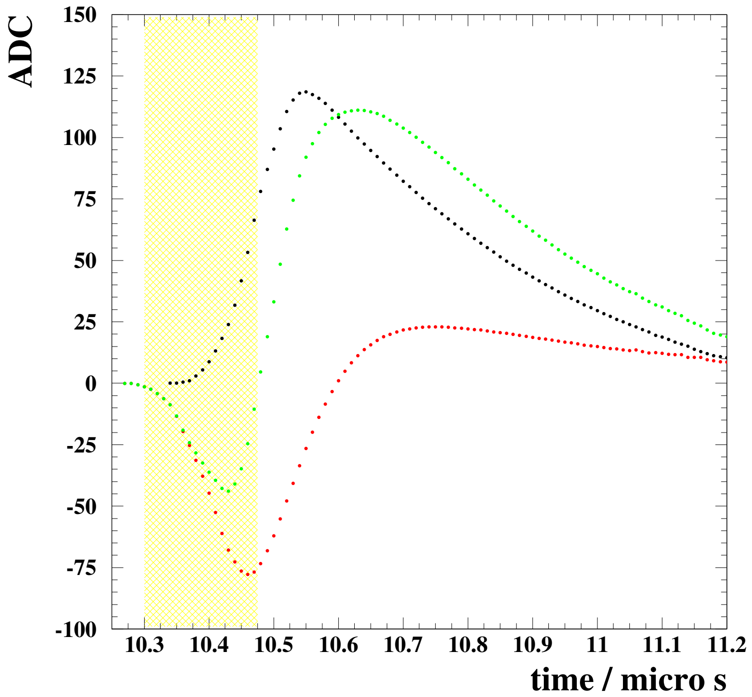

Figure 7.5: An example of the problems caused by the negative swing of cross talk. The original pad signal is shown in black, the cross talk signal in red, and the resulting signal in green. It can be seen that where the negative cross talk signal is larger in magnitude than the original signal a negative signal results which will not be read out. The problematic region is highlighted in yellow.

of the signal for which the subtraction could be successfully carried out. The least squares difference between the recovered pad signal and the predicted pad signal, multiplied by an amplitude factor A is minimised to yield the amplitude factor A, by which the predicted signal needs to be multiplied.

In order to carry out the minimisation of the difference between the two signal shapes they must have the same offset in time. The time offset is found by comparing the time of the peak of the predicted signal, with the peak of the result of subtraction, if the peak exists. If the subtracted signal does not contain the peak, then the peak of a pad within two pads in the same row is used. If this does not exist, the mean of the peaks of a pad from the row above and a pad from the row below are used. A cut is applied on the χ^2 of the minimisation.

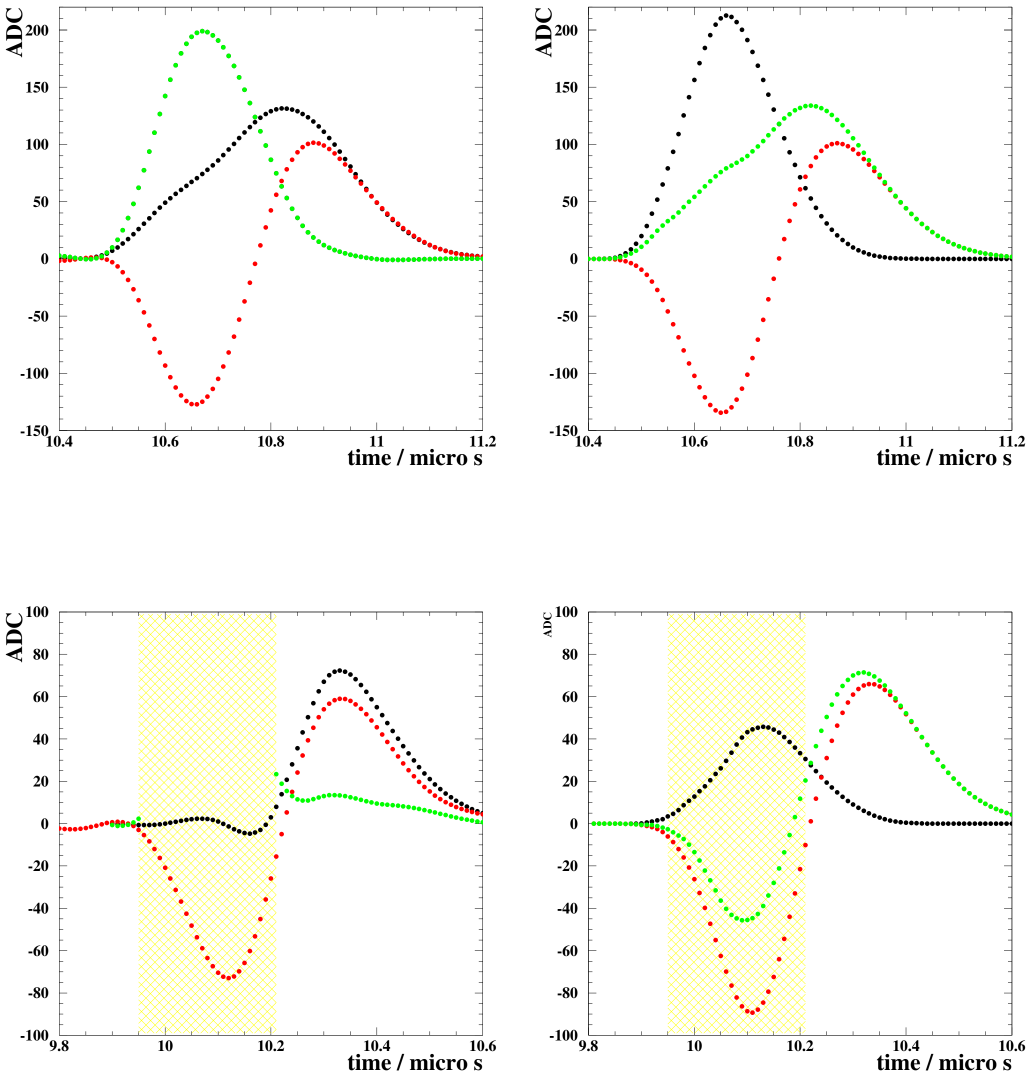

Figure 7.6: Spline fit to ADC series of pad (black left), predicted cross talk signal (red left), result of subtraction (green left). Original MC series (black right), cross talk signal (red right), resulting series (green right). Bins where subtraction of signal is not possible due to negative swing of cross talk signal being larger in magnitude than original signal are highlighted in yellow. Top shows an example where subtraction is possible for entire signal. Bottom shows an example where a large number of bins are missing and the signal cannot be corected.

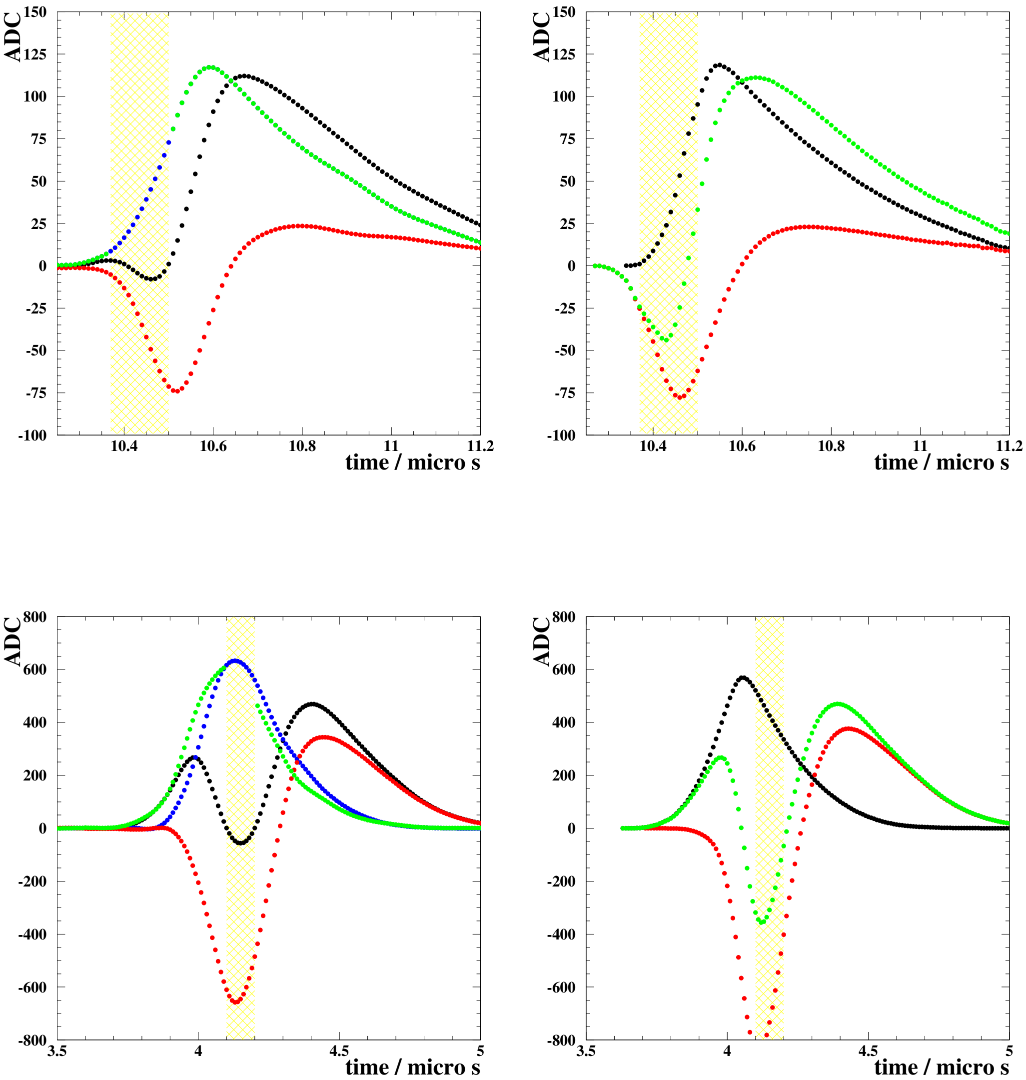

Figure 7.7: Spline fit to ADC series of pad (black left), predicted cross talk signal (red left), result of subtraction (green left), final predicted signal (blue left). Original MC series (black right), cross talk signal (red right), resulting series (green right). Bins where subtraction of signal is not possible due to negative swing of cross talk signal being larger in magnitude than original signal are highlighted in yellow. Top shows an example where a small number of bins are missing and a spline interpolation can be used. Bottom shows an example where subtraction is not possible for a significant number of bins and a minimisation is used.

7.4 Description of the ADC Series Correction Algorithm

A diagram of the algorithms and objects introduced and modified in order to correct cross talk can be seen in Figure 7.8. The procedure consists of the following steps:

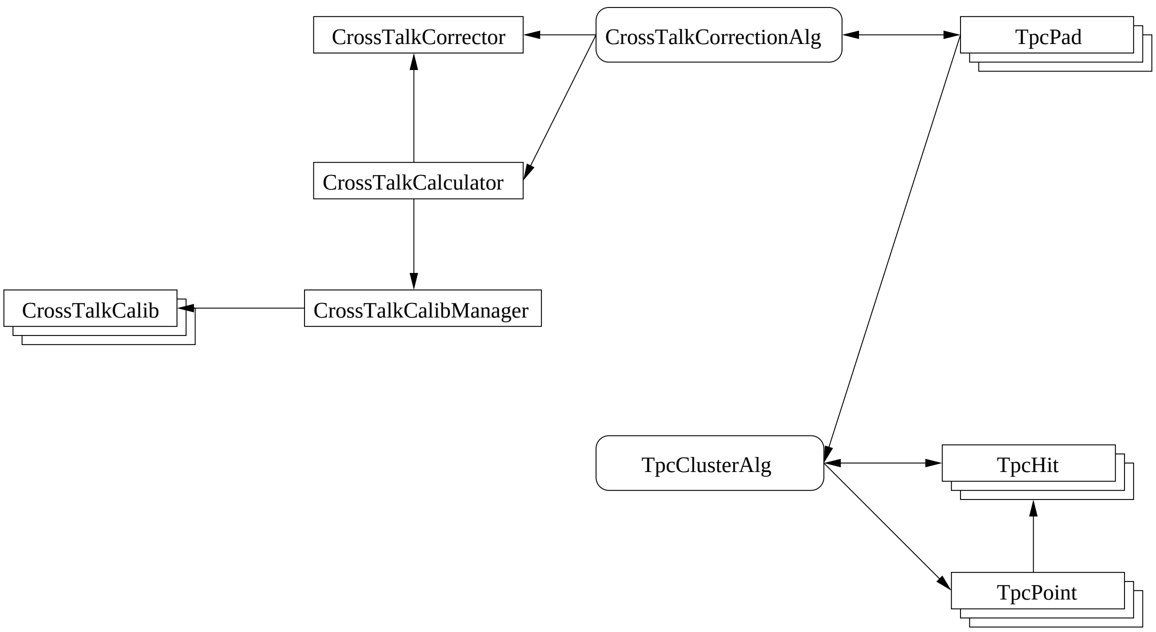

Figure 7.8: Diagram of inter-relation of objects and algorithms correcting cross talk.

- A spline fit is done to the ADC series of each TpcPad
- The number of mothers of each pad which have a signal is saved into each pad
- For each pad which has no mothers with a recorded signal the cross talk induced by those pads is calculated and saved into the daughter pad
- For each pad for which the number of cross talk signals calculated equals the number of mothers the cross talked signals are subtracted from the time series for all bins where subtraction is appropriate
- The signal is then classified into one of the four cases described above and treated appropriately
- The previous three steps are looped over starting from pads where all mothers have been found

- This procedure is repeated until the number of corrected pads is no longer increasing

The process of iterating over pads and deciding, on the basis of the number of mothers with a signal, and the number of these corrected for, in which order to correct them is carried out in the CrossTalkCorrectionAlg. Since the process of predicting the cross talk signal is identical to the requirements of the simulation, the same objects are used. These are: the CrossTalkCalib, to hold information about cross talk relations and transfer functions, the CrossTalkCalibManager, to retrieve the appropriate Calib, and the CrossTalkCalculator, to carry out the required fourier transforms and signal subtraction. The process of deciding what form of correction is appropriate from the time bins which remain after subtraction and carrying out this correction is performed by the CrossTalkCorrector.

7.5 Integration into Reconstruction Framework

Since some pads are lost during the correction procedure it was found necessary to make modifications to the reconstruction in order to get the best possible results from the correction of signal shape. These modifications and their results are described below.

7.5.1 Selection of Pads to Include in a Cluster

The decision of which hits belonged in a cluster is made in the normal way and modifications to the existing code are only made in the calculation of the point position and ADC value. If there are two or more corrected pads in a cluster then only these corrected pads are used in the calculation. Instead of using a weighted mean a gaussian fit to the points is used, meaning that information which is lost due to missing uncorrected pads in the cluster being discarded do not skew the position of the pad, or affect the ADC value of the cluster. The fit is done in ADC against $r\phi$ where the width of the gaussian comes from the pad response function and is fixed. The time is found from a weighted mean of all corrected pads in the cluster.

If not enough corrected pads exist to make a good calculation of the point position then the position of the point is calculated from all existing pads in that cluster (both corrected and uncorrected). A gaussian fit is again done to find the position in $r\phi$ and the ADC. For the calculation of the cluster's time, if there is one corrected pad in the cluster then the time of this pad is used to give the time of this cluster, otherwise a weighted mean is again used.

7.5.2 Association of Errors to Points

In order to make the most effective use of the cross talk correction procedure described, an error was associated to each point in each dimension. These errors were calculated by looking at the residuals of different classes of point which depend on:

- The total number of pads in the cluster
- The number of corrected pads in the cluster

Plots of the residuals for these classes of points can be seen in Figures 7.9 and 7.10. Errors were determined according to the RMS values of these distributions.

7.6 Summary

A correction has been written which predicts cross talk signals according to the fourier transform model, and then subtracts them from the signals recorded on the daughter pads. In some cases such subtraction is not possible due to the negative part of the signal not being recorded. In such cases, alternative methods are used to try to predict the full signal shape wherever possible. Changes are made to the clustering to use only corrected points to find cluster position whenever possible and errors are associated with each point according to the number of corrected pads which were used to calculate the position.

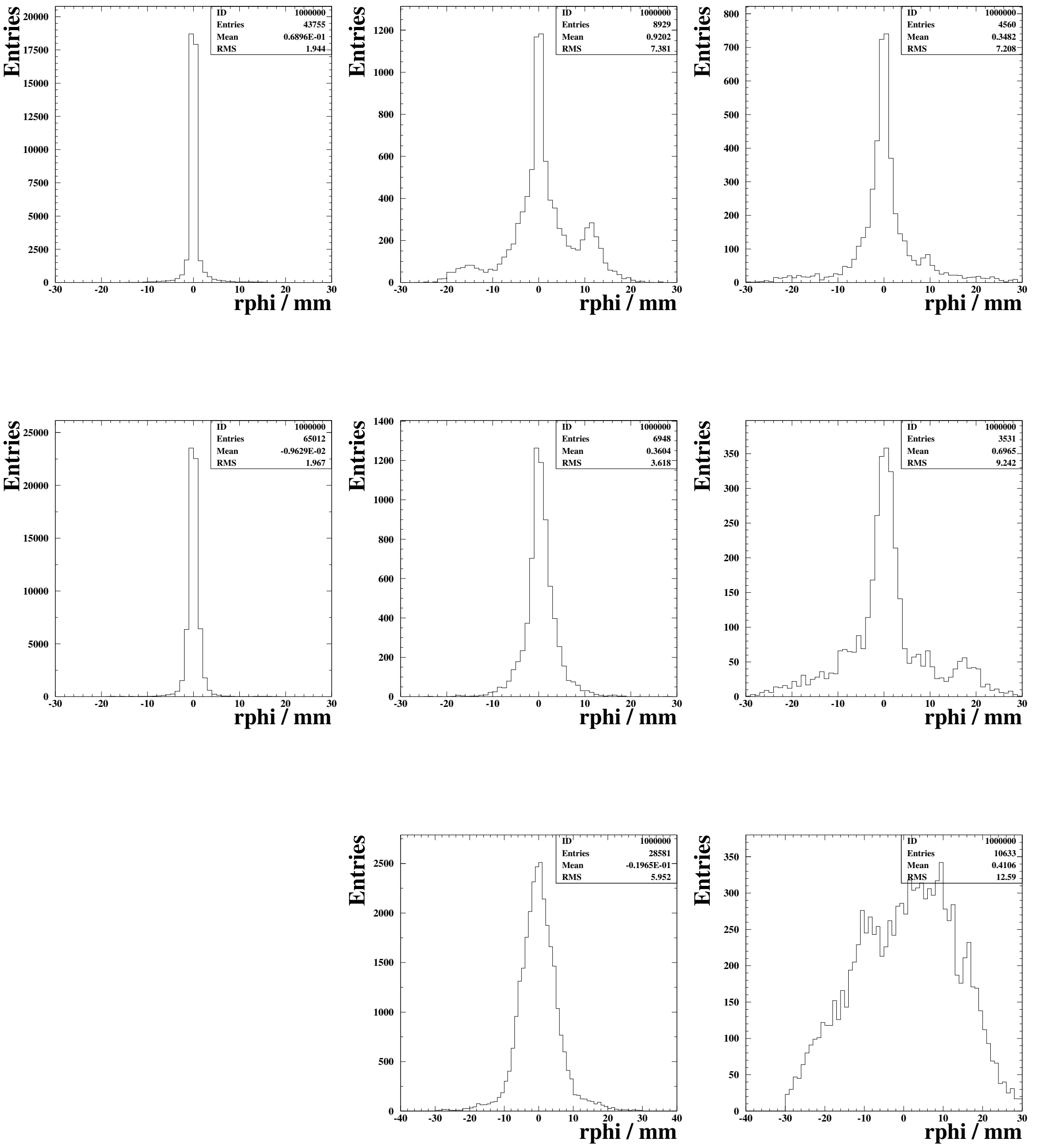

Figure 7.9: Plots of mctruth - reconstructed position in $r\phi$ for different cases. Top row, point containing three or more pads, middle row, points containing two pads, and bottom row, points containing 1 pad. Left points where 2 or more hits are corrected, middle points where 1 pad is corrected, right points where 0 pads are corrected.

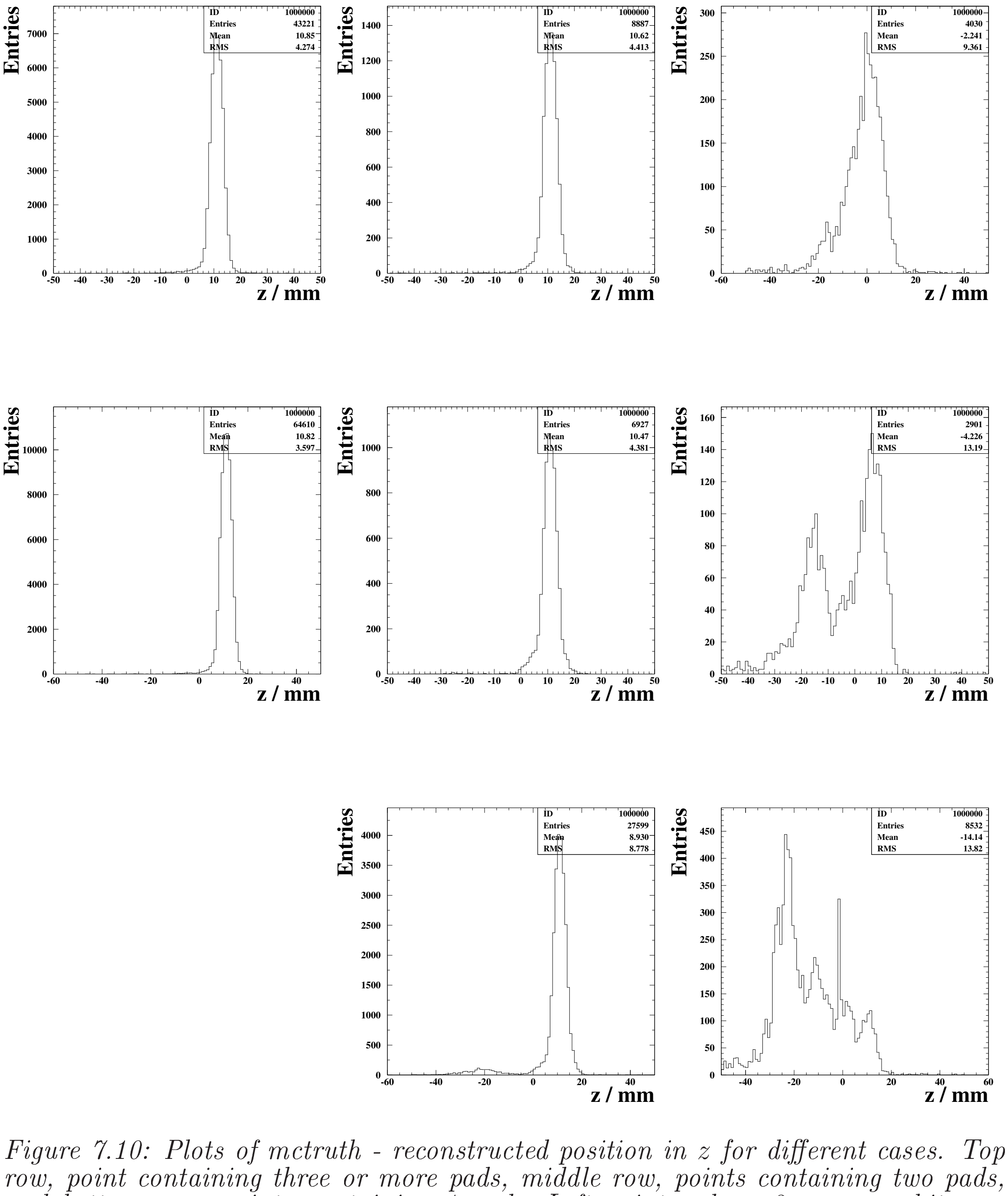

Figure 7.10: Plots of mctruth - reconstructed position in z for different cases. Top row, point containing three or more pads, middle row, points containing two pads, and bottom row, points containing 1 pad. Left points where 2 or more hits are corrected, middle points where 1 pad is corrected, right points where 0 pads are corrected.

Chapter 8

Performance of Correction

In order to study the effect of the cross talk correction process described in the previous chapter, studies using both Monte Carlo and data were performed. A study using a single track Monte Carlo comparing reconstructed positions with Monte Carlo truth positions was used to look at the effect of correction on reconstructed point positions and reconstructed momentum. A study with data compared reconstructed point positions with the reconstructed track position, to understand the effects on reconstructed point positions for data. These results were compared to a Monte Carlo sample in order to understand how well the Monte Carlo reproduced the data.

8.1 Results from Monte Carlo

In order to check the results of the correction on the Monte Carlo a procedure like that described in Chapter 6 was used. 600 MeV pions were fired from the origin at 70° and the effect on different measurable parameters was studied. The correction was studied in incremental steps to see what improvement the introduction of various steps produced:

- Correction of as many signal shapes as possible (no selection of corrected points to make a cluster) and use of deconvolved charge series instead of ADC series
- Introduction of pad selection so that, if possible, only corrected pads are used to find the point position and introduction of gaussian fit
- Introduction of errors on each point in the cluster

All comparisons are done with measured transfer functions for which deconvolution has been applied since this is the best performance that can be obtained from a cross talk correction.

8.1.1 Effect of Correction On Clustering

The effect of cross talk on the number of points found only affects the first stage of correction described above, since this is the only part of correction carried out before the grouping of pads into clusters. The effect can be seen in Figure 8.1 and Table 8.1. The number of points found clearly improves with lost points being recovered; a decrease in the RMS of the distribution is also observed.

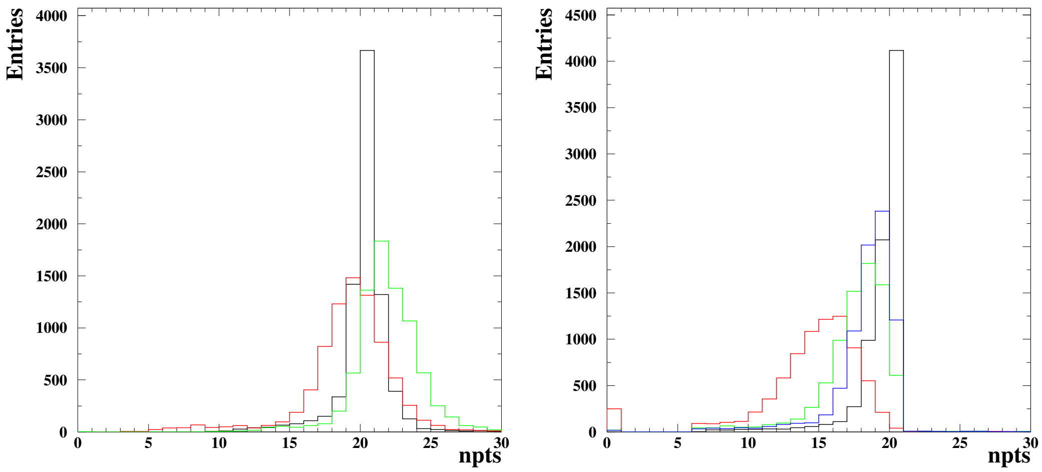

Figure 8.1: Plots of the number of reconstructed points (left) and the number of points used in the track (right). Shown are before cross talk (black), cross talk (red), corrected ADC series(green), and with gaussian fit (blue)

The effect of the correction in $r\phi$ and z is seen in Figure 8.2 and Table 8.1. Large improvements in the $r\phi$ residuals are observed with the increase in the width of the narrow gaussian reducing from 81 % to 18 %. The largest contribution comes from the correction of signal shapes. In z the width goes from an increase of 51 % to 42 %, with a reduction in the asymmetry of the distribution being observed. It should be noted that it is not expected that the distribution will go back to the ideal situation since those points for which correction was not possible are also included in the plots.

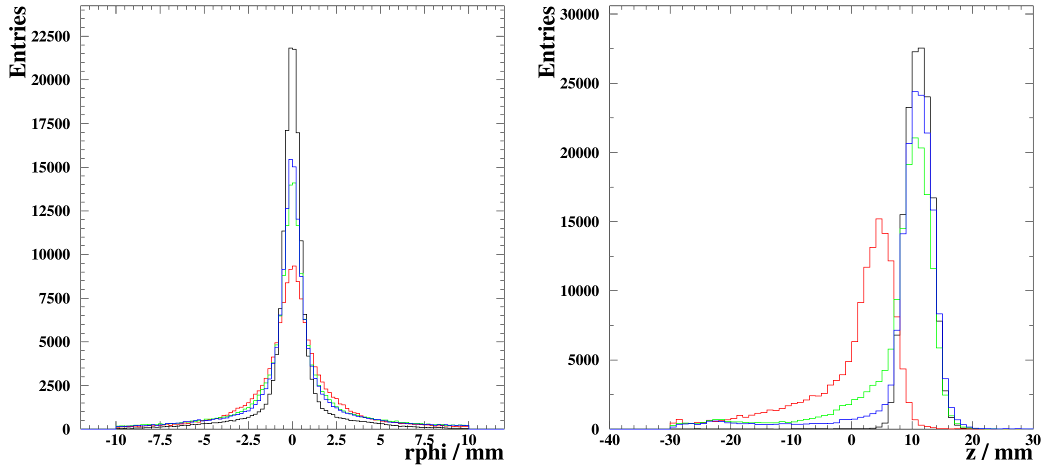

Figure 8.2: Plots of mctruth-reconstructed position for $r\phi$ (left) and z(right). Shown are before cross talk (black), cross talk (red), corrected ADC series (green), gaussian fitted points (blue)

Parameter	Meas. TF	cross talk	corrected ADC series	Gaussian Fit
$r\phi$ mm	0.47(3.48)	0.93(3.94)	0.65(4.29)	0.61(4.25)
z mm	2.05	3.15	2.65	2.35
npts	20.28	19.18	21.85	
npts rms	1.83	3.19	2.33	

Table 8.1: Summary of study of effect of correction on clustering. For $r\phi$ and z numbers indicate the σ values of the two gaussian, for npts values indicate the mean.

8.1.2 Effect of Correction on Pattern Recognition

The number of points in each event and in each track can be seen in Figure 8.1 and the results are summarised in Table 8.2. It can be seen that the number of points found by the pattern recognition increases with incremental levels of correction. It should be pointed out that the number labelled 'efficiency' is not a true measure of efficiency since we do not discriminate between points which are a result of signal and those which occur as a result of cross talk. The RMS of the distribution of points in a track also decreases after correction.

Parameter	Meas. TF	cross talk	corrected ADC series	Gaussian Fit
npts	20.28	19.18	21.85	
npts in track	19.50	14.54	17.51	18.30
npts in track RMS	1.88	3.72	2.64	2.48
efficiency	0.96	0.75	0.80	0.84

Table 8.2: Summary of study of the effect of correction on pattern recognition.

8.1.3 Effect of Correction on Reconstructed Tracks

Figures 8.3, 8.4, and 8.5 show the effect of the three steps of correction on total momentum, longitudinal momentum and transverse momentum. Mean, σ and RMS values can be seen in Table 8.3. The first two stages of the reconstruction give a small reduction in the width of the distributions, but a dramatic improvement is seen with the introduction of weightings on the different points. The bias of the position of the peak is also substantially reduced by the correction. Overall for p_l the increase in RMS is reduced from 16 % to -7 % and for p_t from 15 % to -9 %. For total momentum we go from an increase of 15 % to a decrease of 15 %.

Parameter	meas. TF	cross talk	corrected	gaussian fit	weighted points
total mom GeV/c	0.56	0.52	0.51	0.53	0.56
total σ GeV/c	0.127	0.128	0.144	0.154	0.121
total mom RMS GeV/c	0.264	0.305	0.312	0.297	0.227
pl GeV/c	0.194	0.182	0.182	0.185	0.196
pl σ GeV/c	0.0485	0.0558	0.0570	0.0587	0.0470
pl RMS GeV/c	0.0726	0.0849	0.0878	0.0842	0.0675
pt GeV/c	0.53	0.51	0.50	0.51	0.54
pt σ GeV/c	0.128	0.133	0.146	0.153	0.125
pt RMS GeV/c	0.211	0.243	0.254	0.242	0.190

Table 8.3: Summary of the effect of correction on momentum.

8.2 Effect of Correction on Data

Cosmic muon events were chosen for the study of data since they represent the simplest event topology with only one track per event which passes through the

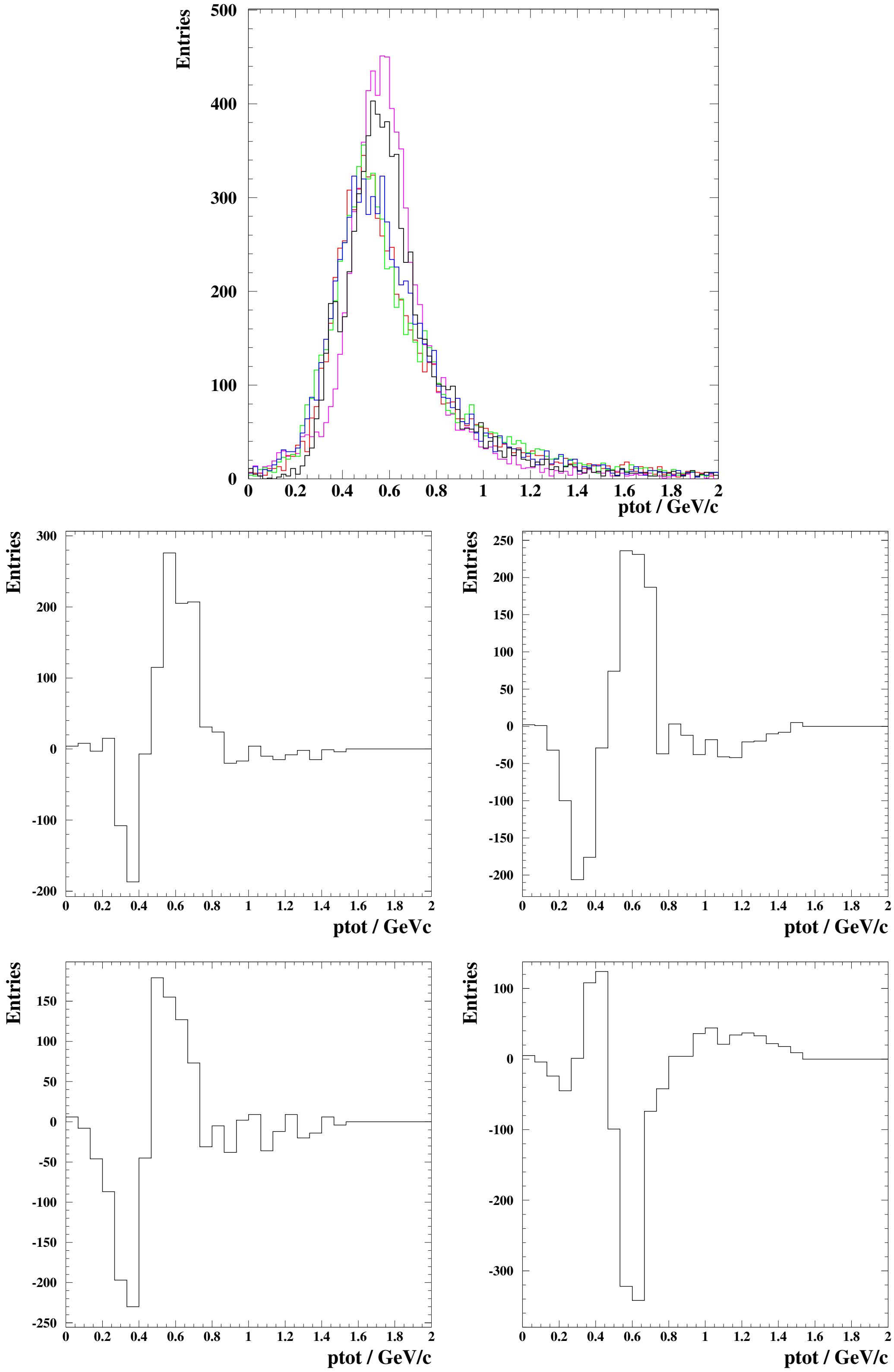

Figure 8.3: Top plot shows distributions of total momentum for different cases. before cross talk (black), cross talk (red), corrected ADC series (green), gaussian fit of points (blue) and weighted points (magenta). Bottom histograms show the differences between the different scenarios and the situation before cross talk: Before cross talk - after cross talk (middle left), before cross talk - corrected ADC series (middle right), before cross talk - gaussian fit of points (bottom left), before cross talk - weighted points (bottom right).

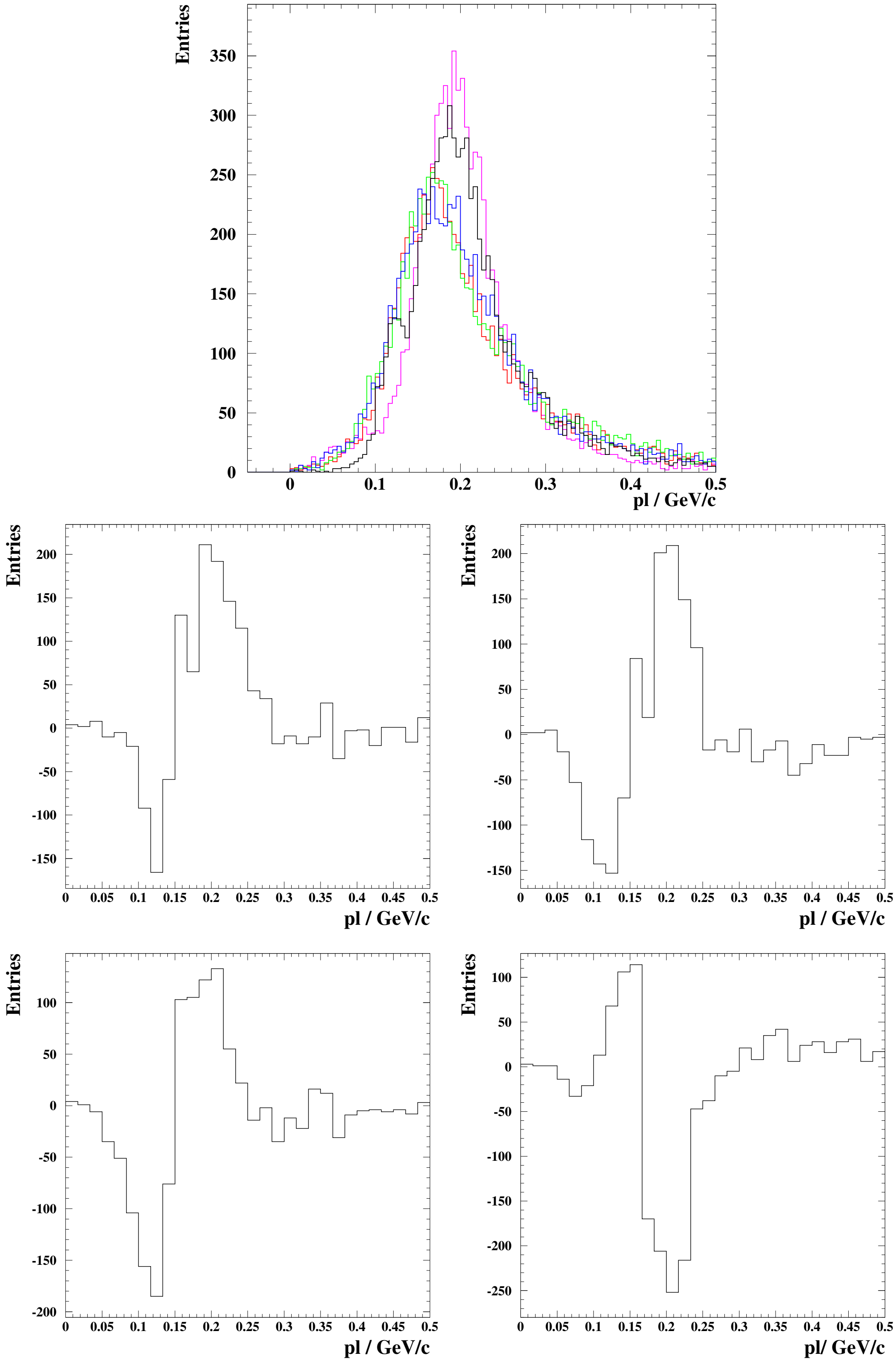

Figure 8.4: Top plot shows distributions of longitudinal momentum for different cases. before cross talk (black), cross talk (red), corrected ADC series (green), gaussian fit of points (blue) and weighted points (magenta). Bottom histograms show the differences between the different scenarios and the situation before cross talk: Before cross talk - after cross talk (middle left), before cross talk - corrected ADC series (middle right), before cross talk - gaussian fit of points (bottom left), before cross talk - weighted points (bottom right).

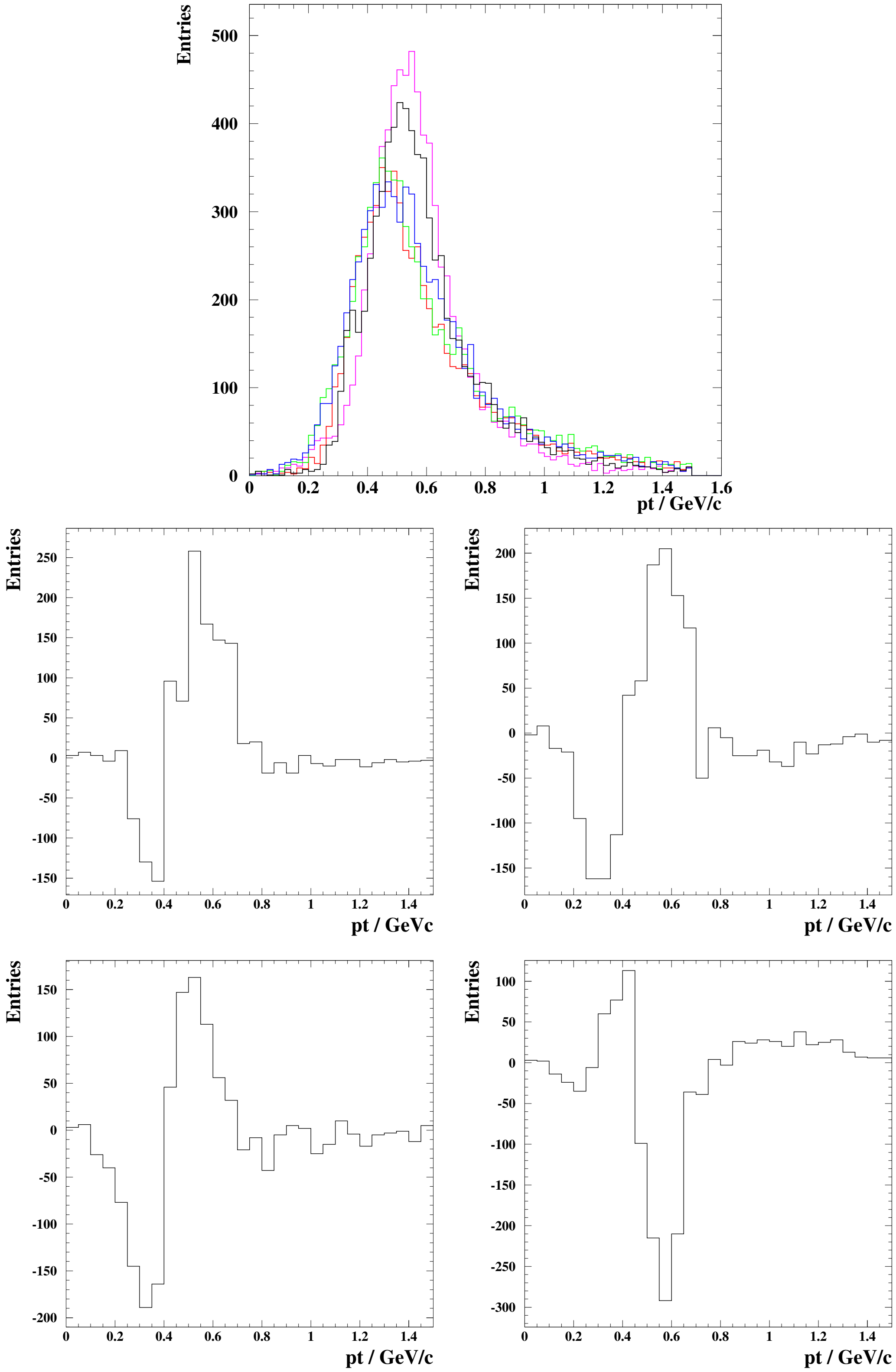

Figure 8.5: Plots of transverse momentum for different cases. before cross talk (black), cross talk (red), corrected ADC series (green) , gaussian fit of points (blue) and weighted points (magenta). Bottom histograms show the differences between the different scenarios and the situation before cross talk: Before cross talk - after cross talk (middle left), before cross talk - corrected ADC series (middle right), before cross talk - gaussian fit of points (bottom left), before cross talk - weighted points (bottom right).

centre of the TPC. Cosmic ray data from 2003 were used. These data use as trigger a central scintillator along the beam axis. The scintillator extends from -450mm to 230mm in z. This means that tracks whose electrons drift through the worst region of electric field distortions (see chapter 2) do not cause a trigger and are therefore not read out.[1]

For comparison purposes a Monte Carlo data sample was also used. This consisted of single track muon events originating from the outer edge of the TPC and passing through the centre. A cosmic generator was written for the purpose, and was passed variables to mimic the distributions in z, ϕ, θ and energy of the cosmic ray data.

Both data sets were run both with and without the cross talk correction in order to see the effect of the correction on reconstructed observables. As stated in the previous chapter the correction relies on both the knowledge of the cross talk relations between different pads, and a knowledge of the response of each pad to an input delta charge. At the time of writing this information was available only for sector six of the TPC. This means that the correction treats each sector as if it has identical cross talk relations and signals shapes to sector six All results shown and quoted are for sector six only, unless otherwise stated.

8.2.1 General Observations

In order to observe at the most basic level the effect of correction on data a large number of individual pulse shapes were initially studied. In many cases clear improvements of the signal shapes were observed, including the removal of second peaks, or improvements in distorted signal shapes. An example of such a case can be seen in Figure 8.6. It is clear that the negative swing of the predicted cross talk signal is in exactly the position of the dip in the original signal. This is removed once the cross talk signal is subtracted. Cases such as this provide a very striking example of the validity of both the cross talk model and the correction of individual signal shapes.

A scan of events was then performed to observe how the positions of points differed before and after correction. This scan showed that after correction the number of points which were found by the pattern recognition increases. A general smoothing of the points in a track is also observed after the application of the correction. A typical event can be seen in Figure 8.7. The track in the top right

[1]The edge of the inner field cage is at 286mm and this is the position of a large spike in the electric field

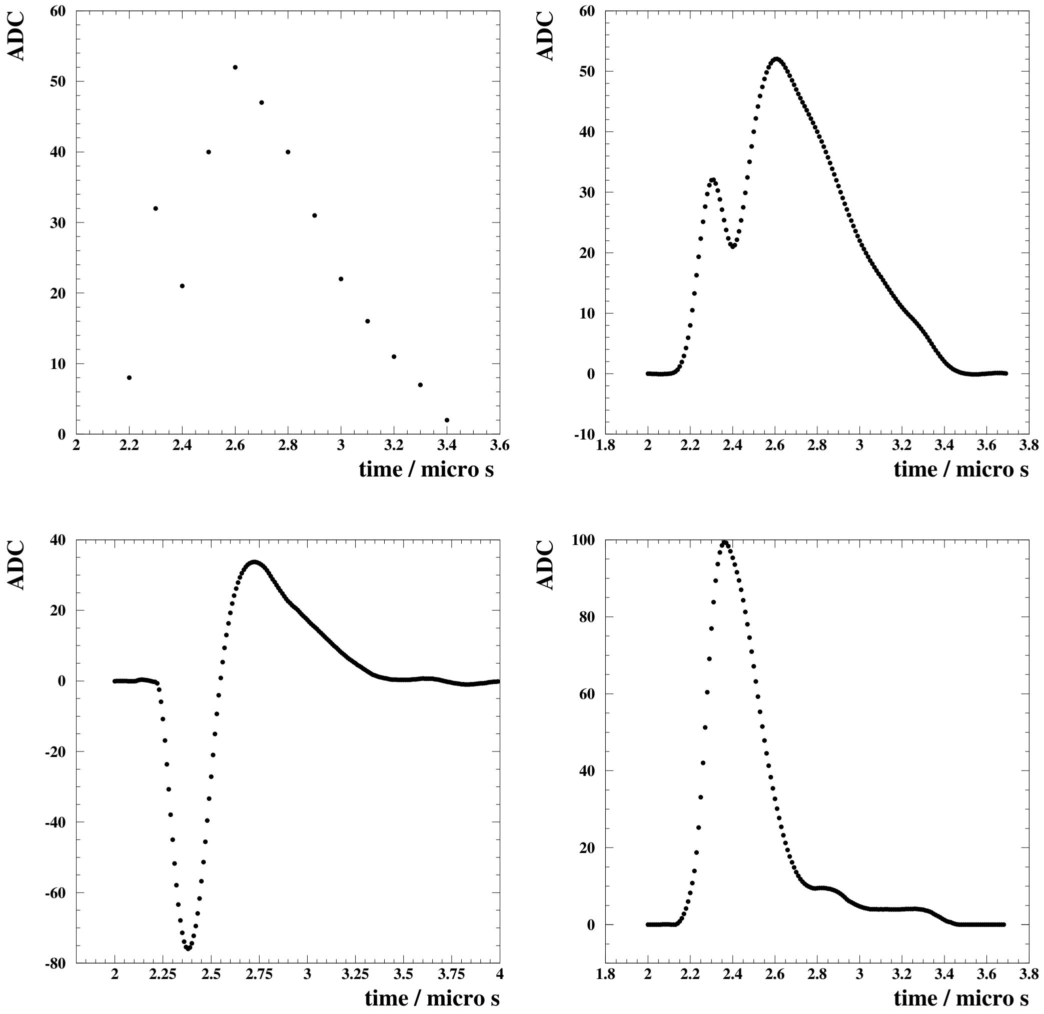

Figure 8.6: Example of a corrected signal shape from data. Shown are: original ADC series (top left), spline fit to ADC series (top right), predicted cross talk signal (bottom left), corrected signal (bottom right).

of each plot is in sector six of the TPC. It can be seen that while the correction is more effective in this sector, substantial improvement are also seen in the other arm of the cosmic in sector three. This suggest that there are considerable similarities between the cross talk relations of different sectors, as would be expected due to each sector having the same electronic layout.

Next reconstructed observables were examined. For all observables studied, in addition to examining the differences between the observables before and after correction, the differences between Monte Carlo and data were also analysed. Both differences between Monte Carlo and data before and after correction, and differences in the effect of the correction were examined. The aim was both to try to

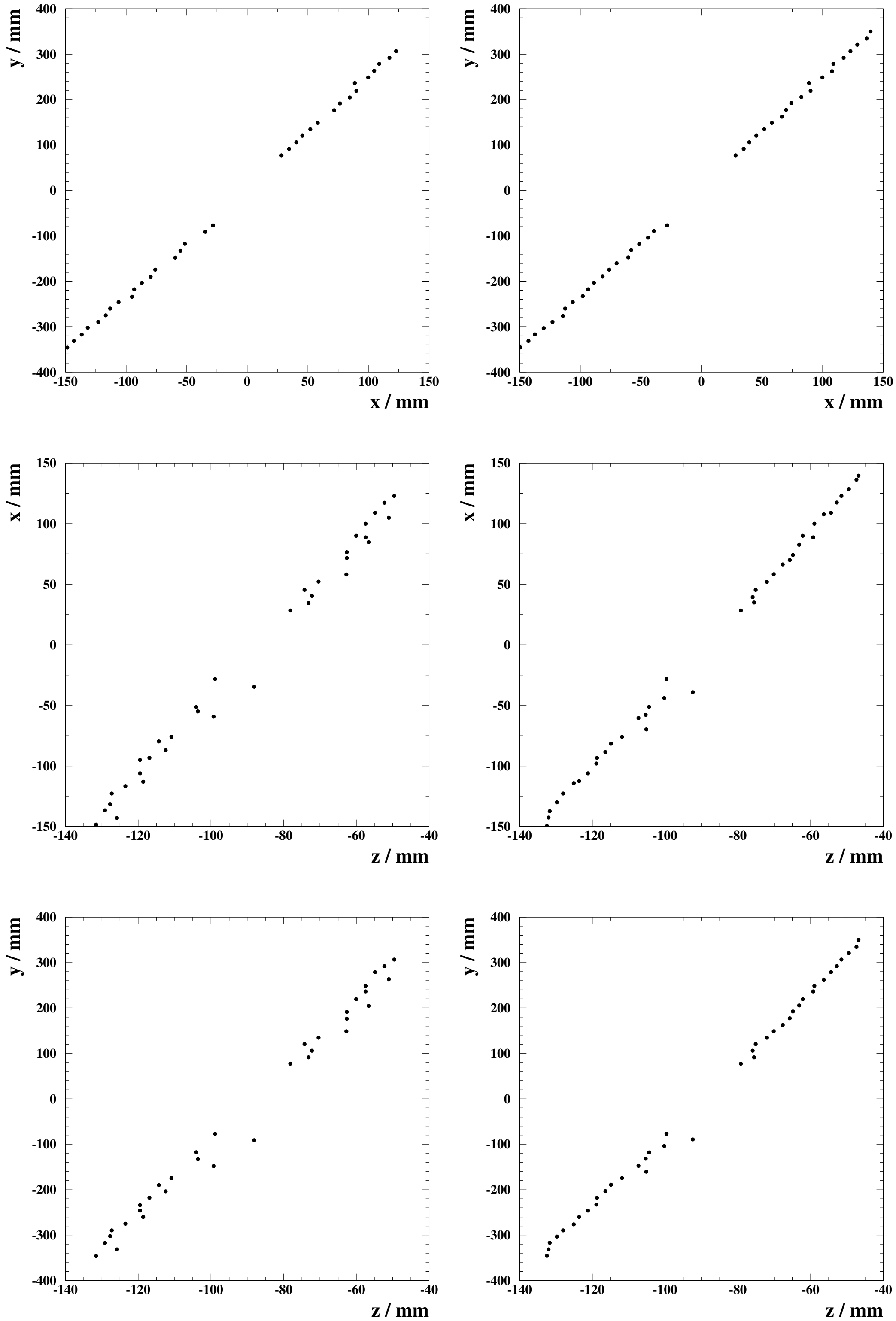

Figure 8.7: Example of a typical cosmic event before correction (left) and after correction (right). The plots show the positions of points found by pattern recognition in the xy plane (top), xz plane (middle), yz plane (bottom).

ascertain that the correction produced significant improvements in the data and also to understand how well the Monte Carlo was able to reproduce the effect of cross talk and its correction on data.

For all plots of reconstructed observables, the following cuts were made:

- The flag of the track fit must be 0 (see Chapter 6)
- The number of points in the track must be greater than 10.

these cuts remove tracks for which reconstruction was not successful.

Figure 8.8 shows the number of points per track before and after correction. An increase in the number of points is seen both in Monte Carlo and data. While the number of points increases by 2.7 in the Monte Carlo the increase is 0.7 in the data. The shapes of both plots change in a similar way becoming more asymmetric after correction, and a narrowing of the distributions is seen in both cases.

Figure 8.9 shows the number of hits per cluster for all clusters which are used in a track passing the cuts. While in Monte Carlo the number of hits per cluster increases by 0.75 after correction, in the data the increase is only 0.13. There is also disparity in the shapes of the distributions. It is believed that the differences in the distribution shapes are caused by effects in the data which are not present in the Monte Carlo, for example, dead and hot pads which will cause missing pads in the data but are not reproduced in Monte Carlo[2]. This will result in migration of points to lower bins.

8.2.2 Study of Residuals

It was decided to use $r\phi$ and z residuals as a means to study the effect of correction on data. $r\phi$ and z residuals were chosen rather than energy (dE/dx) resolution, since while energy resolution is dependent on the relative equalisation of all pads in the TPC, $r\phi$ resolution depends only on the relative resolution of pads in an individual cluster. This is expected to be dominated by the electronics gain which has been measured. The z residuals are independent of relative equalisations of pads. This means that $r\phi$ and z residuals can be studied without the effects of unequalised pads affecting the data Monte Carlo comparison.

Unbiased residuals were studied in each case. These were found by refitting the track with the point for which the residual was being found removed. The residual

[2]Some pads are dead in the Monte Carlo due to pads which were not measured or were dead during the pulser runs, however the number of pads which are dead during a typical run is much larger.

in $r\phi$ was calculated as the distance in $r\phi$ at the radius of the pad row in question between the point, and the intersection in the xy plane of the track with this circle. The residual in z is the distance in z between these two points[3] . Each residual distribution was fitted to a double gaussian.

$r\phi$ Residuals

The residual distributions in $r\phi$ can be seen in Figure 8.10 and the fit parameters are shown in Table 8.4. The fit is done to a double gaussian. Dramatic improvement is seen in the width of the narrow gaussian after application of the correction for data with a reduction of 24 %. This shows good agreement with the Monte Carlo which shows a reduction in width of 13 %. The wide gaussian shows a reduction in the data of 7 % but an increase in the Monte Carlo of 11 %. This discrepancy in the wide gaussian is not considered a cause for concern. As mentioned the composition of the wide gaussian is sensitive to hot and dead pads in the data, since in $r\phi$ the position is dependent on information from multiple pads. In addition around 50 % of points found in the data are not associated with a track. This background noise will also have an effect on the distribution of hits per point in the data. The fact that good agreement is found in the smaller gaussian indicates that cross talk and hence its correction are well modelled in the simulation. Differences in the exact sigmas of data and Monte Carlo are at least partially due to field distortions in the data, which though partially reduced by the use of the scintillator trigger are still present. A measure of the area of the gaussian is found by multiplying the value of σ by the amplitude of the gaussian. Though the ratio of these two areas is slightly different between Monte Carlo and data, the wide gaussian having a larger component in data for the reasons described above, the behaviour after the correction is the same, with the ratio between the two gaussians staying quite constant.

z Residuals

The plots of z resolution show dramatic improvement after correction. Good agreement between data and Monte Carlo is also observed (see Figure 8.11 and the results of the fit in Table 8.5). The width of the small gaussian shows a decrease of 17% in the data and 42 % in the Monte Carlo. The offset of the centre of this gaussian from 0 reduces from -1.62 to -0.16 in the data and from -1.76 to -0.28 in the Monte Carlo. The large gaussian also sees a reduction of its offset from 0.99 to 0.75 in the data and from 1.59 to 0.61 in the Monte Carlo, showing both excellent performance

[3] Code provided by S. Borghi

data set	σ_1 mm	σ_2 mm	amp_1	amp_2	ratio
uncorr data	1.50	4.10	1533	563	50:50
corr data	1.14	3.85	1999	679	47:53
uncorr mc	1.27	3.35	4647	1240	59:41
corr mc	1.11	3.74	6993	1274	62:38

Table 8.4: Fit parameters to double gaussian fits of $r\phi$ residuals, σ_1 and amp_1 indicate the σ and height of the narrower gaussian, and $sigma_2$ and amp_2 those of the broader gaussian. The ratio given is the ratio of areas of the two gaussians.

of the correction and good agreement between data and Monte Carlo. The ratios of areas of the two gaussians also show good agreement. with the ratio of 36:64 in the data increasing to 64:36 and 47:53 in the Monte Carlo increasing to 66:34. A reduction of 15 % in the width of the large gaussian is observed for the Monte Carlo which is not present in the data.

data set	σ_1 / mm	σ_2 / mm	amp_1	amp_2	ratio	$offset_1$	$offset_2$
uncorr data	1.81	4.20	2214	1664	36:64	-1.62	0.99
corr data	1.52	4.18	5115	1050	64:36	-0.16	0.75
uncorr mc	1.89	4.39	1226	575	47:53	-1.76	1.59
corr mc	1.10	3.29	3615	626.5	65:34	-0.28	0.61

Table 8.5: Fit parameters for gaussian fits to z residuals.σ_1 , $offset_1$ and amp_1 indicate the σ, distance of the peak from zero and height of the narrower gaussian, and σ_2 , $offset_2$ and amp_2 those of the broader gaussian. The ratio given is the ratio of areas of the two gaussians.

Multi Track Events

As was previously mentioned single track events have been used for the study of the performance of the correction since these represent the simplest event topology. It is expected that multi track events will not result in significant differences in performance to those presented in this chapter. Multi track events will only pose problems for the correction if the tracks are so close together as to create more cross talk relation on the pads constituting a single track. As shown in chapter 5 cross talk relations typically act on pads within only one or two pads in the $r\phi$ direction.

Therefore in order to cause problems the tracks need to be both very close in ϕ and close enough in the z direction that the pad signals will overlap in time. Due to the relatively low multiplicities at HARP energies (see Figure 1.4) it is considered that multi track events will not pose any problems for the correction.

8.3 Summary

The correction of signal shapes gives significant improvements on the $r\phi$ and z resolutions of points with respect to Monte Carlo truth. These improvements can be further enhanced by the judicious selection of hits from which to calculate the point's position, and the use of a gaussian fit rather than a weighted mean. This results in a reduction of the width of $r\phi$ residuals from an 81 % increase after the addition of cross talk to just 18 %. In z there is a reduction from 51 % to 42 %. Due to large differences in residuals of corrected and uncorrected points it is necessary to weight the points in the fit in order to see significant improvements in the momentum resolution. With all the steps in place the RMS of the momentum distributions can be reduced by a significant factor. An increase of $\sim$ 16 % in RMS values of both p_l and p_t can be reduced to a decrease of 7 % in p_l and 9 % in p_t.

The correction is shown to be very effective on the data. A reduction in the $r\phi$ residuals of 24 % is observed and a reduction in the z residual of 17 %. This shows that the correction results in a large improvement in the data. Further to this, very good agreement with the Monte Carlo is seen where the $r\phi$ residuals show a decrease of 13 %. This, along with striking similarities in the z residual distributions and their changes after correction, lead to the conclusion that the cross talk is well modelled in the data. Discrepancies exist between the Monte Carlo and data however, and these are believed to be due to effects which are not yet modelled in the data. Specifically hot and dead pads, background noise and field distortions which are present in data but not in the Monte Carlo.

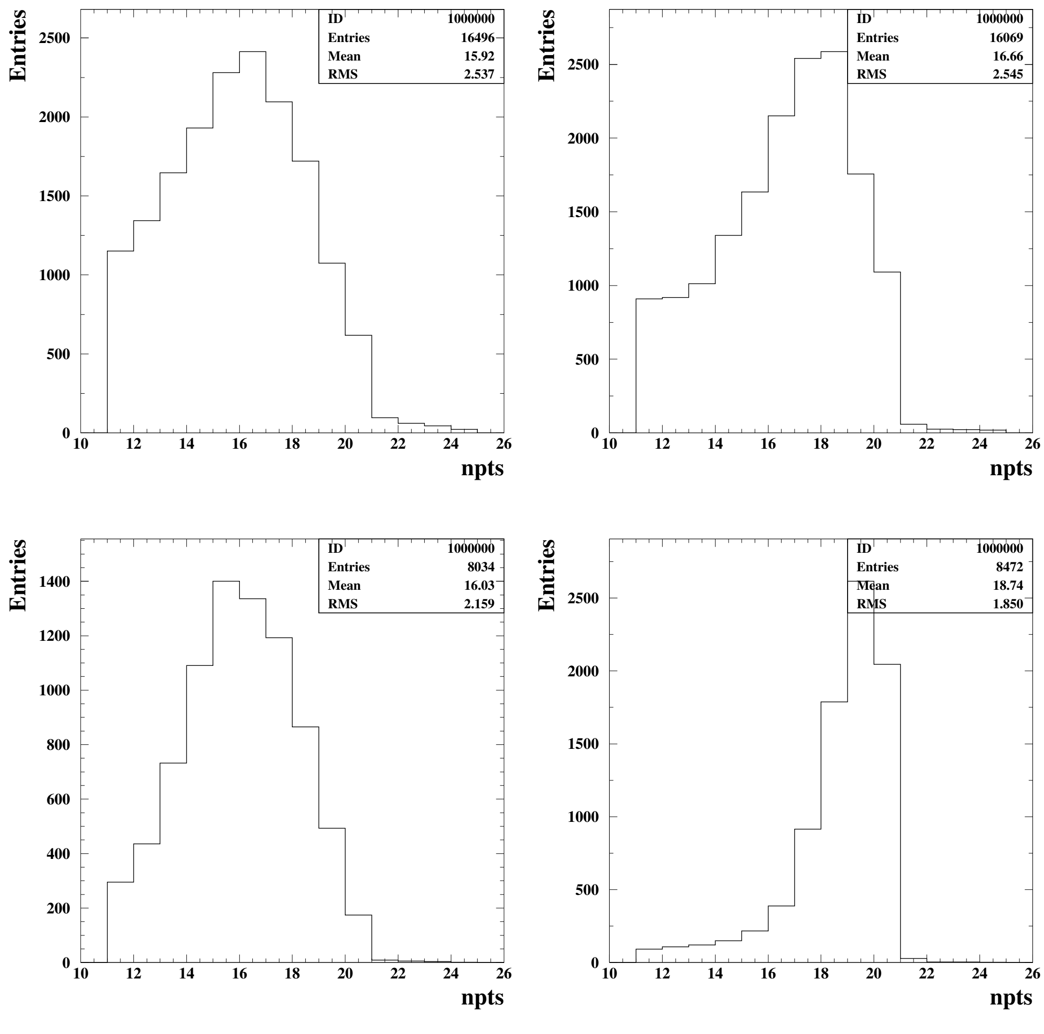

Figure 8.8: Number of points per track in cosmic data events (top) and Monte Carlo cosmics (bottom). Plots on the left are before cross talk correction and those on the right after.

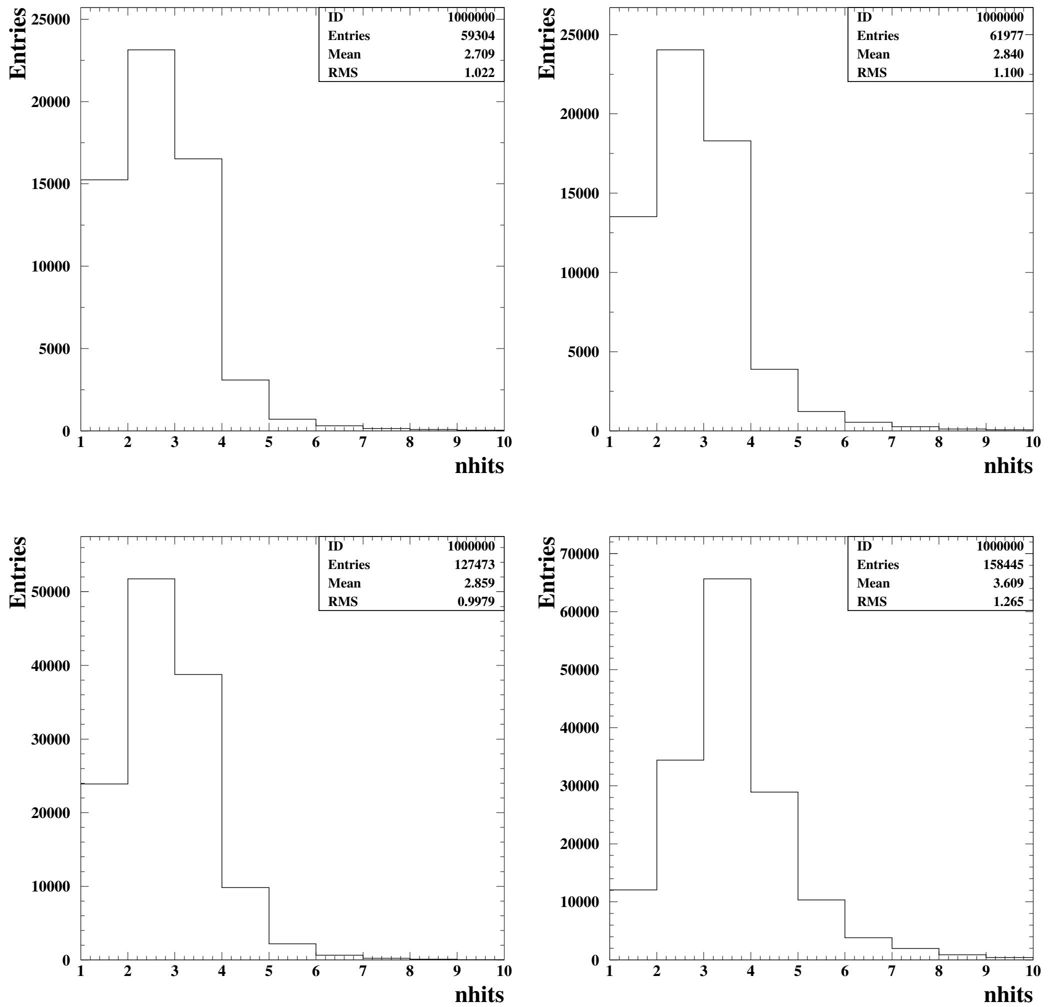

Figure 8.9: Number of hit per cluster for data (top) and Monte Carlo (bottom). Both before correction (left) and after correction (right).

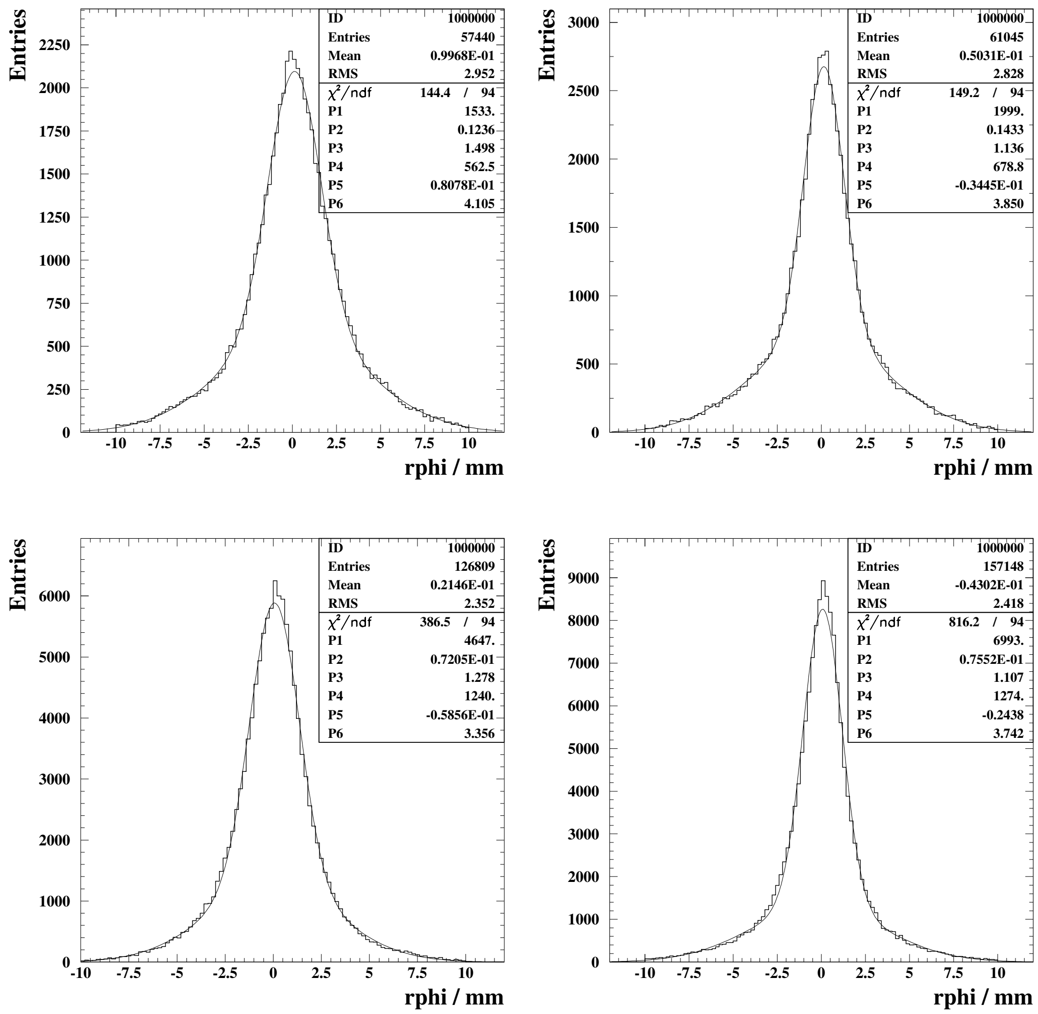

Figure 8.10: $r\phi$ residuals. For data (top) and Monte Carlo (bottom). Uncorrected is shown on the left, and corrected on the right.

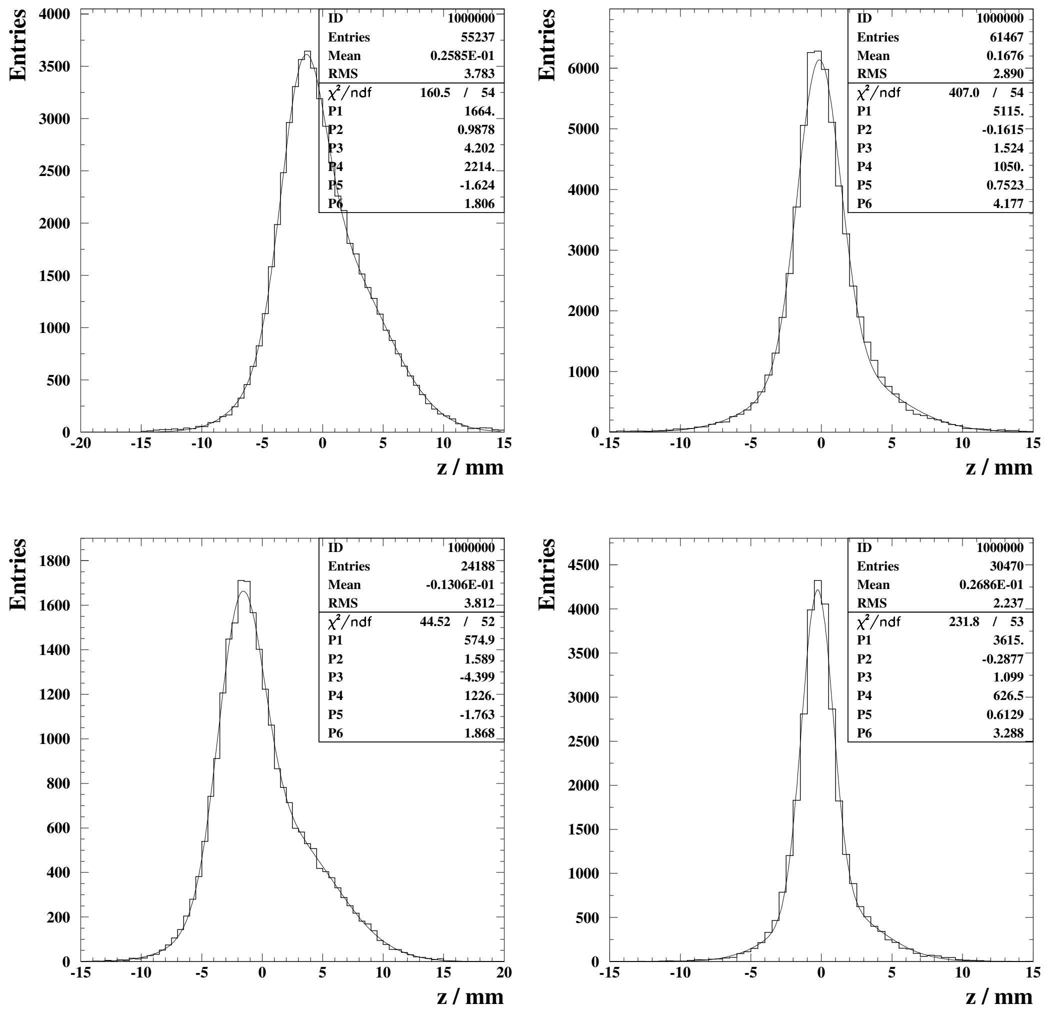

Figure 8.11: z residuals. For data (top) and mc (bottom). Uncorrected is shown on the left, and corrected on the right.

Chapter 9

Summary

The recent discovery of neutrino mass means measurements of the parameters of the neutrino sector are of increasing interest and importance. Currently the design of future neutrino experiments and understanding of the systematic uncertainties in existing experiments are hampered by uncertainties in the calculation of neutrino fluxes stemming from a lack of high precision hadron production data in the region of interest. The HARP hadron production experiment was proposed to address this problem.

The HARP experiment aimed to measure hadron production cross sections with beam momenta from 2 to 15 GeV/c. The experiment was designed to give as close to 4π acceptance as possible. Forward going particles were tracked by a series of drift chambers with particle identification in this angular region provided by a TOF system, a threshold Cherenkov counter and an electron and muon identifier. For particles leaving the target at large angles with respect to the beam axis, tracking and particle identification were provided by a TPC with the particle identification in this angular region complemented by a layer of RPCs. In order to have the experiment taking data on a short timescale, many detectors were recovered from other experiments, and the remaining detectors were designed and commissioned on very short timescales. Inevitably a few problems resulted, most notably a cross talk problem in the TPC.

In addition to the tracking of secondary particles, tracking of beam particles is also necessary in order to give the impact point of beam particles on the target. A series of algorithms has been written to reconstruct the trajectories of incoming beam particles using the multi-wire proportional chambers. The software has been tested with a Monte Carlo simulation, and using efficiencies for each plane taken from the data, the reconstruction efficiency is found to be 99.9 % and the error on position at the target 0.45 mm.

A good understanding of detectors is clearly crucial to the ability to produce accurate physics results. To this end the prototype TPC Monte Carlo has been rewritten to reproduce the design performance of the TPC. For each physics process validation plots have been produced demonstrating that the TPC simulation reproduces design specifications. This provided a solid and flexible framework into which additional effects could be introduced.

An unwanted cross talk effect was found in the TPC during 2002 data taking, which occurred as a result of capacitive couplings between the inputs and outputs of preamplifiers on the TPC motherboard. In cases where these couplings are between the inputs and outputs of the preamplifier of the same pad this results in alterations of the signal shape. Where the couplings are between the input of one pad's preamplifier and the output of another pad's preamplifier this results in signals on the daughter pad whether on not there was an input signal. Once the simulation of the design TPC was completed it was possible to simulate on top of this the effects of cross talk. This was done in two stages firstly by introducing the measured signal shapes that occur as a result of cross talk and then modelling the effect of cross talk between pads.

A study was performed to ascertain the effect of cross talk on reconstruction. It is found that cross talk causes an increase in the width of $r\phi$ residuals of up to 115 % and up to 85 % for the width of z residuals. This results in an increase in the width of momentum distributions of the order of 200 % with respect to the ideal situation[1].

An algorithm was designed to correct for the effects of cross talk. This correction worked by predicting the cross talk signals which are expected with the fourier transform model using the signals on mother pads, and then subtracting them from the signals on the daughter pads. Since cross talk can result in negative signals which are not read out out by the DAQ this was not always possible. In such cases alternative methods to recover the original signals had to be found. Changes were also made to the reconstruction to maximise the use that could be made from these corrected signal shapes.

The correction was found to reduce the effects of cross talk on the width of $r\phi$ residuals from an increase of 81 % with respect to the situation without cross talk to an increase of just 18 % at 70°. For z residuals an increase in width of 51 % with respect to the situation without cross talk was reduced to 42 %. This resulted in dramatic improvements in the RMS of momentum distributions with an increase in p_t of 15 % with respect to the situation without cross talk changing to a reduction

[1]Numbers quoted are for 600 MeV pions

of 9 % and an increase in p_l of 16 % changing to a reduction of 7 %.

The correction was then applied to cosmic ray data and the effect of the correction on $r\phi$ and z residuals with respect to reconstructed position was studied. A reduction of the sigma of $r\phi$ residual of 24 % is observed showing good agreement with a similar study using the Monte Carlo where a reduction of 13 % is observed. The z residuals show a reduction in width of 17 %. In both Monte Carlo and data a large asymmetric shoulder in the z distribution is observed before correction, which is almost eliminated by the correction. These results demonstrate that the correction is working on the data and that the Monte Carlo and data show good agreement. At the time of writing the cross talk map and measured transfer functions are only available for sector six. Work is currently underway to provide this data for the other five sectors. So far it appears that the cross talk relations of different sectors are almost identical, as would be expected from the fact that they are constructed in the same way. For this reason no significant differences are expected in the performance of the correction on the other five sectors.

In conclusion it is seen that the correction produces large reduction of the effect of cross talk on momentum resolution in the Monte Carlo. The correction is also seen to show substantial improvement in the $r\phi$ and z residuals in data. Agreement between Monte Carlo and data is good, and further improvements are expected after the introduction into the Monte Carlo of additional effects such as hot and dead pads and field distortions. The good agreement between data and Monte Carlo means that we can conclude that most effects of cross talk on momentum resolution can also be corrected in the data. This can be tested once the necessary parameters are available for the other five sectors of the TPC, using comparisons of the momenta of the two arms of a cosmic ray track.

Appendix A

Software Framework

A.1 GAUDI

HARP software is written within the GAUDI framework, developed for the LHCb experiment at CERN [86]. The Gaudi Framework makes a clear distinction between "data" and "code", where data consist of variables and would include things such as tracks, points and hits, and code is that which performs operations on data like objects. All software written by the author therefore falls into 2 categories:

- DataObjects
- Algorithms

DataObjects and Algorithms are the "data" and "code" base classes, and all software written inherits from one of these two classes. Each algorithm has three member functions: initialize, execute and finalize. For each algorithm which is run the initialize phases of all algorithms are called once in the order specified. Next for each event which is processed the execute phases of the algorithms are called in order and finally the finalize phase of each algorithm is called once in order.

Each Algorithm is able to utilise the various services provided by GAUDI. These include: the event data store where Objects can be stored between algorithms, the ntuple and histogram services which take care of the production of these files and the message service which controls the verbosity of the various algorithms.

Algorithms also make use of the jobOptions service which reads information in from a steering file called a jobOptions file. This allows parameters to be passed to the Algorithms at run time. It is here that the Algorithms and their order are specified along with which libraries are needed and which services are required.

A.2 Harp Software Framework

The HARP software is written in Object Oriented C++ in the GAUDI framework. Within this framework software is organised into packages each with a specific task defined in the user and software requirements. Only certain dependencies between the packages are allowed as can be seen in Figure A.1, so for example the DetResponse Software is not allowed to know anything about Reconstruction. These dependencies are defined to stop incorrect dependencies within the software.

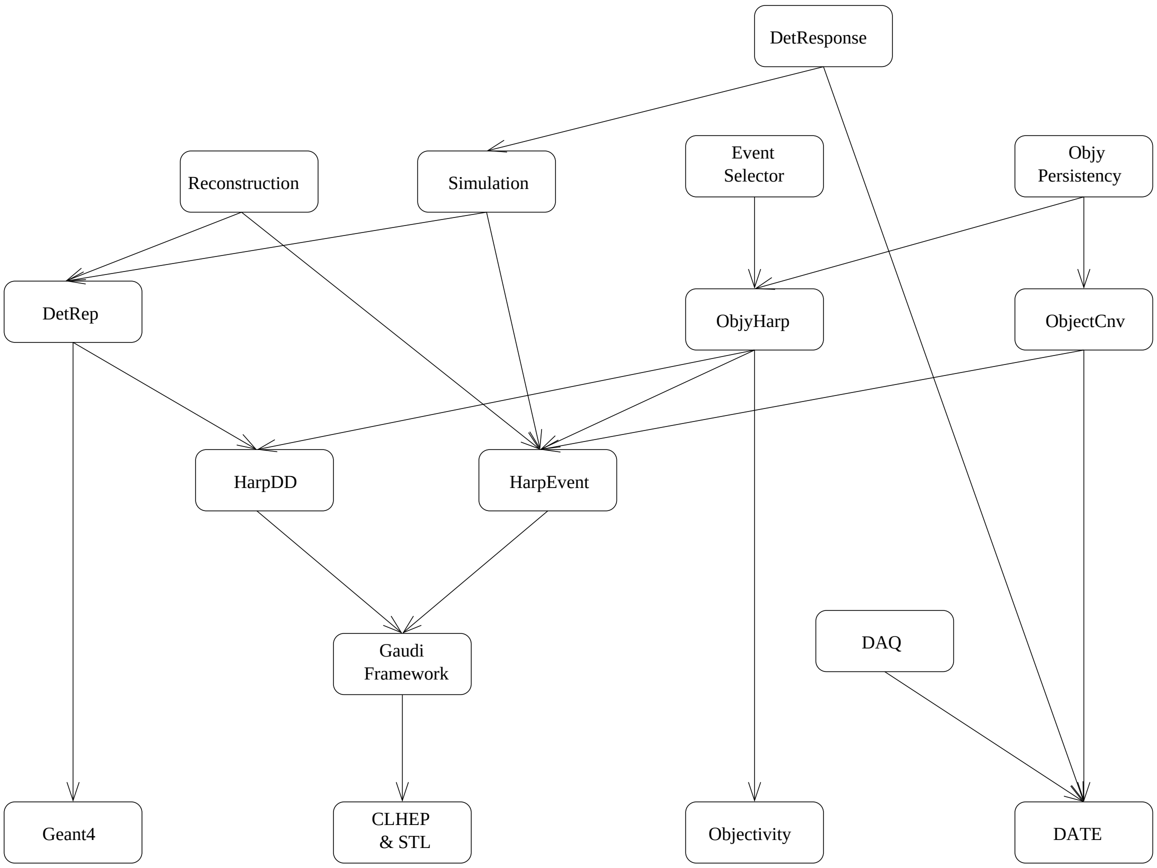

Figure A.1: Diagram showing the dependencies of the packages in the HARP software framework. Arrows indicate permitted dependencies.

The packages contributed to by the author or heavily used are:

- ObjectCnv : Decodes information from the Database and creates objects containing basic hit information
- Reconstruction : Reconstructs basic hit information eventually resulting in tracks and particles

- Simulation : Simulates interactions of particles within the detector using GEANT4.
- DetResponse : Simulates the response of the detector to particles produced
- HarpEvent : Contains DataObjects which hold the raw, reconstructed and Monte Carlo information

In addition to these HARP specific packages the framework also contains several other libraries such as GAUDI, GEANT4, DATE, CLHEP, and Objectivity.

Bibliography

[1] F. Reines and C.L. Cowan. Detection of the Free Neutrino. *Phys. Rev.*, 92:830, 1956.

[2] L. Grodzins M. Goldhaber and A.W. Sunyar. Helicity of Neutrinos. *Phys. Rev.*, 109:1015, 1958.

[3] G. Danby et al. Observation of High-Energy Neutrino Reactions and the Existence of Two Kinds of Neutrino. *Phys. Rev. Lett.*, 9:36, 1962.

[4] Halzen and Martin. *Quarks and Leptons*. Wiley, 2002.

[5] M. Naakagawa Z. Maki and S. Sakata. Remarks on the Unified Model of Elementary Particles. *Progr. Theor. Phys.*, 28:870, 1962.

[6] D.E. Groom et al. Particle Data Group. *Eur. Phys. J.*, page 280, 2001.

[7] B. Kayser. Neutrino Physics as Explored by Flavour Change. *Phys. Rev. D*, 66, 2002.

[8] L. Wolfenstein. Neutrino Oscillations in Matter. *Phys. Rev.*, page 2369, 1978.

[9] A. de Santo. An Experimentalists View of Neutrino Oscillations. hep-ex/0106089.

[10] Y. Fukada. Evidence for Oscillation of Atmospheric Neutrinos. *Phys. Rev. Lett.*, 81:1562, 1998.

[11] Q.R. Ahmad et al. Measurement of the rate of $\nu_e + d \rightarrow p + P + e^-$ interactions produces by ^{8}B solar neutrinos at the Sudbury Neutrino Observatory. *Phys. Rev.Lett.*, 87:71301, 2001.

[12] K. Eguchi et al. First Results from KamLAND: Evidence for Reactor Anti-Neutrino Disappearance. hep-ex/0212021.

[13] C. Athanassopoulos. Evidence for $\nu_\mu \to \nu_e$ Neutrino Oscillations from LSND. nucl-ex/9709006, 1997.

[14] B. Armbruster et al. Upper limits for neutrino oscillations $\overline{\mu}_\mu \to \overline{\nu}_e$ from muon decay at rest. hep-ex/0203021, 2002.

[15] E. Church et al. A proposal for an experiment to measure $\nu_\mu \to \nu_e$ disappearance at the Fermilab Booster BooNE. http://www.neutrino.lanl.gov/BooNE/boone_proposal.ps, 1997.

[16] Yuichi Oyama. K2K (KEK to Kamioka) neutrino-oscillation experiment at KEK-PS. hep-ex/9803014v2, 1998.

[17] S. Geer. Neutrino Factories : Physics. hep-ph/0008155, 2000.

[18] G. Gregoire et al. Proposal to Rutherford Appleton Laboratory: An International Muon Ionisation Cooling Experiment (MICE). http://hep04.phys.iit.edu/cooldemo/micenotes/public/pdf/MICE0021/MICE0021.pdf, 2003.

[19] R. Edgecock. Neutrinos from Muon Storage Rings. 2001. UKNF Note 20 : http://hepunx.rl.ac.uk/neutrino-factory/muons/documents.html.

[20] The Neutrino Factory and Muon Collider Collaboration. Expression of Interest for R and D towards a Neutrino Factory Based on a Storage Ring and a Muon Collider. physics/9911009, 1999.

[21] http://hepunx.rl.ac.uk/neutrino-factory/muons/uknf.html.

[22] R. Bennett C. Densham, P. Drumm. Considerations of Temperature Distribution in Heavy Metal Targets for the Neutrino Factory. UKNF Note 1 : http://hepunx.rl.ac.uk/neutrino-factory/muons/documents.html, 1999.

[23] R. Bennett. Some Thoughts on a High Power Radiation Cooled Rotating Toriodal Target for Neutrino Production. UKNF Note 2 : http://hepunx.rl.ac.uk/neutrino-factory/muons/documents.html, 1999.

[24] T.K. Gaisser and M. Honda. Flux of Atmospheric Neutrinos. hep-ph/0203272, 2002.

[25] The AMS collaboration. The Alpha Magnetic Spectrometer (AMS) on the International Space Station Part I : Results from the Test Flight on the Space Shuttle. http://ams.cern,ch/AMS/Publications/AMS-06.ps, 2002.

[26] K. Abe et al. Measurements of Proton, Helium and Muon Spectra at Small Atmospheric Depths with the BESS Spectrometer. astro-ph/0304102, 2003.

[27] E802 Collaboration. A single arm spectrometer detector system for high-energy heavy-ion experiments, 1990.

[28] I. Chemakin et al. A facility to study proton-nucleus and heavy ion collisions using a large acceptance detector with particle identification capabilities. http://www.phys.bnl.gov/ e910/html/phys/proposal/proposal.ps.

[29] S. Afansiev:1999. The NA49 large acceptance hadron detector.

[30] M.G. Catanesi et al. Proposal to study hadron production for the neutrino factory and for the atmospheric neutrino flux. 1999. CERN-SPSC/99-35 (SPSC/P315).

[31] P.D. Barnes et al. Proposal to measure particle production in the meson area usin main injector primary and secondary beams. http://www.phys.fnal.gov/ experiments/e907/Proposal/P97-EOI.pdf.

[32] Yu. P. Nikiton A.N. Kalinovskii, N.V. Mokhov. *Passage of High Energy Particles through Matter.* American Institute of Physics, 1985.

[33] D. Horn and F. Zachatiasen. *Hadron Physics at Very High Energies.* W.A. Benjamin Inc., 1973.

[34] P. Capiluppi et al. Charged particle production in proton-proton inclusive reactions at very high-energies. *Nucl. Phys.*, B79:189, 1974.

[35] P. Capiluppi, G. Giacomelli, A. M. Rossi, G. Vannini, and A. Bussiere. Transverse momentum dependence in proton-proton inclusive reactions at very high-energies. *Nucl. Phys.*, B70:1, 1974.

[36] B. Alper et al. Production spectra of $\pi^{\pm}$, $k^{\pm}$, $\rho^{\pm}$ at large angles in proton-proton collisions in the CERN intersecting storage rings. *Nucl. Phys.*, B100:237, 1975.

[37] T. Abbott et al. Measurement of particle production in proton induced reactions at 14.6-GeV/c. *Phys. Rev.*, D45:3906–3920, 1992.

[38] I. Chemakin et al. Inclusive soft pion production from 12.3 and 17.5 GeV/c protons on Be, Cu and Au. nucl-ex/0108007, 2001.

[39] C. Caso et al. Proton-proton interactions at 6GeV/c. *Nuovo Cim.*, 45:66, 1966.

[40] S.P. Almeida. pp interactions at 10 GeV/c. *Phys. Rev.*, 174:1638, 1968.

[41] N.Ono et al. Nuclear mass number dependence of inclusive pion production by pions and protons at 4.3 GeV/c. *Phys. Lett.*, 84B:515, 1979.

[42] I. Chemakin et al. Measuring centrality with slow protons in proton nucleus collisions at 18-GeV/c. *Phys. Rev.*, C60:024902, 1999.

[43] A. Ferrari A. Fasso and P.R. Sala. Fluka: Status and prospective for hadronic applications. invited talk in the Proceedings of the MonteCarlo 2000 Conference, Lisbon., 2000.

[44] The Geant4 Collaboration. Physics reference manual. http://wwwasd.web.cern.ch/wwwasd/geant4/G4UsersDocuments/PhysicsReferenceManual/PhysicsReferenceManual.html, 2003.

[45] N.V. Mokhov. The mars code system user's guide. FermiLab-FN-629, 1995.

[46] J. Collot, H. G. Kirk, and N. V. Mokhov. Pion production models and neutrino factories. *Nucl. Instrum. Meth.*, A451:327–330, 2000.

[47] D.J. Simon. The CERN PS : A versatile particle factory. CERN-PS-96-019-DI, 1996.

[48] http://psdoc.web.cern.ch/PSdoc/acc/pscomplex.html.

[49] http://harp.web.cern.ch/harp/Classified/PICTURES/Drawings/Harp/HARPdetector.ps.

[50] P. Gorbounov and L. Scotchmer. MWPC : Layout and Geometry. http://harp.web.cern.ch/harp/Classified/Sub_detectors/MWPC/index.html, 2001.

[51] O. Gutsche. Report on the Improvements of the Calibration of the Time of Flight Hodoscopes of the HARP Experiment. http://harp.web.cern.ch/harp/Students/index.html, 2001.

[52] http://harp.web.cern.ch/harp/Classified/Sub_detectors/Beam/plots/beam_part_sep_3GeV.eps.

[53] C. N. Booth. Simulation of Interactions in the HARP Target Support, 2000. HARP NOTE 00-005.

[54] http://harp.web.cern.ch/harp/Classified/Sub_detectors/Beaminst/drawings/beamline6.eps.

[55] F. Braid. Efficiency of Target Defining Scintillator for HARP. http://harp.web.cern.ch/harp/Classified/Sub_detectors/Trigger/TDS/Seamus_rpt.ps, 2000.

[56] A. Lundborg. Electrostatic Simulations of parts of the HARP TPC. HARP-NOTE 00-009, 2000.

[57] G. Vidal Sitjes. *The HARP Time Projection Chamber*. PhD thesis, Universidad de Valencia, CERN, 2003.

[58] F. Dydak. On distortions of TPC coordinates : inhomogeneities of electric and magnetic field. HARP-NOTE 03-001, 2003.

[59] J. Wotschak. Proposal for an RPC system for TOF measurement in HARP. HARP-NOTE 00-007, 2000.

[60] M. Anfreville et al. The drift chambers of the NOMAD experiment. *Nucl. Instr. and Meth.*, A481:339, 2002.

[61] G. Barichello et al. The HARP TOF Wall counter construction and test. HARP-NOTE 02-001, 2002.

[62] http://harp.web.cern.ch/harp/Classified/Sub_detectors/TOF/drawings/slab.eps.

[63] U. Dore et al. EMC Calibration and MUID. HARP NOTE 03-007, 2003.

[64] R. E. Kalman. A New Approach to Linear Filtering and Prediction Problems. *J. Basic. Eng.*, 82:35, 1960.

[65] R. E. Kalman. Application of Kalman Filtering to Track and Vertex Fitting. *Nucl. Instr. and Meth. A*, 262:444, 1987.

[66] A. Cervera-Villanueva. Kalman filter tracking and vertexing in a silicon detector for neutrino physics. CERN-EP/2001-092.

[67] R. J. Barlow. *Statistics - A Guide to the Use of Statistical Methods in the Physical Sciences*. John Wiley and Sons, 1989.

[68] A. Grossheim. private communication, 2003.

[69] R.K. Bock and A. Vasilescu. *The Particle detector Briefbook*. Springer-Verlag, 1998.

[70] D.H. Perkins. *Introduction to High Energy Physics*. Addison-Wesley, 1982.

[71] F. Sauli. Principles of operation of multiwire proportional and drift chambers. CERN 77-09, 1977.

[72] I. Smirnov. Interactions of particles with gas. http://consult.cern.ch/writeup/heed, 1997.

[73] R. Veenhof. Calculations for the Harp TPC read-out. http://r.home.cern.ch/r/rjd/www/Harp/, 2001.

[74] A. Peisert and F. Sauli. Drift and diffudion of electrons in gases: A compilation. CERN 84-08, 1984.

[75] R. Veenhof. Simulation of gaseous detectors. http://garfield.web.cern.ch/garfield/, 2001.

[76] W. Blum and L. Rolandi. *Particle Detection with Drift Chambers*. Springer-Verlag, 1983.

[77] Knoll. *Radiation Detection and Measurement*. Wiley, 1989.

[78] G. Vidal-Sitjes. Cross talk measurement on spare sector. Talk at HARP Collaboration Meeting 10 June 2002, 2002.

[79] G. Giannini et al. On the TPC Analog Signals. HARP-NOTE 03-005, 2003.

[80] G. Vidal Sitjes. Status of the TPC analog electronics measurement. HARP-NOTE 03-006, 2003.

[81] M. Galasso et al. *GNU Scientific Library Reference Manual, 2nd Edition*. Network Theory Ltd., 2003.

[82] G. Vidal-Sitjes. Private Communication.

[83] R. Veenhof S.Borghi, M.G. Catanesi. Clustering algorithm. http://ps-proj-hadroprod-analysis.web.cern.ch/ps-proj-hadroprod-analysis/AnalysisNotes/NoteCluster.ps, 2003.

[84] S.Robbins. Cosmic rays with the rpc trigger. Talk at Harp Collaboration Meeting 10th December, 2001.

[85] M.C. Morone. *Evaluation of Silicon sensors for the ATLAS Silicon Tracker and TPC Reconstruction in the HARP Experiment*. PhD thesis, Geneva, 2003.

[86] M. Cattaneo and P. Maley. Gaudi users guide. http://lhcb-comp.web.cern.ch/lhcb-comp/Frameworks/Gaudi/Gaudi_v9/GUG/GUG.pdf, 2001.